B_1 INHOMOGENEITY COMPENSATION IN MAGNETIC RESONANCE IMAGING (MRI)

by

Suwit Saekho

BS, Chiangmai University, 1985

MS, East Carolina University , 2000

Submitted to the Graduate Faculty of

School of Engineering in partial fulfillment

of the requirements for the degree of

Doctor of Philosophy

University of Pittsburgh

2004

UNIVERSITY OF PITTSBURGH

SCHOOL OF ENGINEERING

This dissertation was presented

by

Suwit Saekho

It was defended on

December 1, 2004

and approved by

George D. Stetten, M.D., Ph.D., Department of Bioengineering

Fernando E. Boada, Ph.D., Departments of Radiology and Bioengineering

Qing X. Yang, Ph.D., Pennsylvania State University College of Medicine Department of Radiology

V Andrew. Stenger, Ph.D., Departments of Radiology and Bioengineering

Dissertation Director

B_1 INHOMOGENEITY COMPENSATION IN MAGNETIC RESONANCE IMAGING (MRI)

Suwit Saekho, PhD

University of Pittsburgh, 2004

This thesis concentrates on the reduction of RF field (or B_1) inhomogeneity in high magnetic field MRI. B_1 inhomogeneity is one of the major drawbacks in high field MRI. The non-uniformity causes regions of increased and decreased signal intensity in the images. None of existing methods can perfectly correct the non uniformity. This thesis aims to develop new methods that are practical, safe, and required no additional devices.

Specifically, three-dimensional (3D) tailored RF (TRF) pulse were designed and validated in human MRI experiments at 3 Tesla. Two novel designs of 3D TRF pulses for B_1 inhomogeneity reduction are presented in this thesis. Both designs are based on the small flip angle approximation. The first design is for a thick slab 3D acquisition. These pulses employ a 3D stack of spirals k-space trajectory simultaneously with B_1 inhomogeneity compensated RF pulse waveforms during excitation. Another pulse design uses analytical functions as a compensated B_1 inhomogeneity pulse weighting function. The k-space is modeled in the manner such that k_x-k_y provides compensated spatial weighting function for quadratically varying B_1 inhomogeneity patterns. The k_z-direction is controlled by fast switching gradients in the fashion similar to Echo planar imaging (EPI). This design is more appropriate for 2D high resolution acquisition images.

The two pulse designs show equal improvement of signal loss of approximately 30%. Long pulse length, 22 ms, and limited peak B_1 are the major concern of the first design. The second design,

the compensated fast k_z pulses provide relatively shot pulse length only 3-5 ms. The primary limitation of this design is that it can be used for only a quadratic pattern of B_1 inhomogeneity and may cause resonance shift.

TABLE OF CONTENTS

LIST OF FIGURES

PREFACE

Many people around me have contributions to this thesis in both direct and indirect ways. I would like to deeply thank Dr. V Andrew Stenger, my advisor, for his teaching, guidance and support. Without him, I would never have made it. I do apologize for being stubborn to him sometimes. I would also like to thank my thesis committee for useful comments and corrections. I also owe many thanks to many people including Dr. Peter Bornert (Phillips Research Laboratories, Hamburg, Germany) for kindly providing me a reference, all friends in my lab and Heidi Green for texts editing. I am really grateful to my family back home for providing me moral support throughout my journey.

1.0 INTRODUCTION

1.1 THE USES OF HIGH FIELD MAGNETIC RESONANCE IMAGING

In recent years, the use of high field magnetic resonance imaging (MRI) technologies has rapidly increased. The great advantages of a high field MR system include increased signal-to-noise ratio (SNR) [1-3], increased contrast-to-noise ratio (CNR) [4] and improved chemical selectivity [5, 6]. Several applications have exploited the benefits of the higher field strength MRIs [7, 8], including functional MRI (fMRI), magnetic resonance angiography (MRA), magnetic resonance spectroscopy (MRS). Functional MRI is the area that high magnetic fields have had the most impact by virtue of the increased magnetic susceptibility, which enhances the blood oxygenation level dependent (BOLD) contrast [8-11]. This effect is of advantage to the increase of spatial resolution after neural activity. Magnetic Resonance Angiography (MRA) demonstrates improved visualization of small vessels in high field MRI [7, 12]. The improved resolution results from the increased SNR of high field. Christoforidis *et al* [13, 14] have identified venous structures below 100 microns in brains, using 8T MRI. In MR spectroscopy, the higher magnetic field provides better peak separation [6, 8]. Additional advantage of high field MRI is

to facilitate tissue segmentation which many studies such as those exploring Alzheimer's disease[1] and schizophrenia[2] have relied on.

1.2 PROBLEMS OF HIGH FIELD MRI

A number of benefits exist as advance to higher field strength; however, the increased field strength is also associated with many technical challenges leading to problems that need to be solved. Higher field strength causes increasing of B_1 inhomogeneity, increasing the amount of RF energy deposited in tissue, and increasing of susceptibility artifacts. Details will be discussed in the chapter 3.

1.3 SIGNIFICANCE OF THIS THESIS

B_1 inhomogeneity is a significant issue for high field MRI and will be addressed throughout this thesis. Inhomogeneity causes an imbalance of signal intensity across an image. This effect can result in the loss of details in one or more particular areas of the image. This problem is of greater concern when high field imaging is employed. In high field MRI, the lack of uniformity is more severe than in low field MRI since the B1 propagating through the object has shorter wavelengths and greater attenuation. The interference of the waves from all directions in the object can cause signal cancellation and addition, producing areas of decreased and increased intensities inside the image. This thesis aims to develop a new method for reducing the B_1

[1] Progressive brain disorder that causes a gradual and irreversible decline in memory
[2] Severe mental illness characterized by a variety of symptoms, including loss of contact with reality, disorganized thinking and speech

inhomogeneity using 3D TRF pulses. This approach does not require any additional hardware, it is easy to implement, and it is practical.

1.4 THE AIMS OF THIS THESIS

(a) To develop B_1 inhomogeneity compensated 3D TRF pulses for routine use in a commercial 3T scanner. The desired pulse needs to provide an acceptable pulse width of approximately 3-5 ms, and it must be safe for use with humans. The pulse sequence will be modified to allow for single-shot or multi-shot excitation to be used with a multi-shot spiral acquisition so that high-resolution images (1mm) can be acquired.

(b) To validate the effectiveness of artifact reduction of the pulses.
The images acquired from a standard sinc pulse will be compared with the images acquired from the compensated 3D TRF pulse. Image magnitude profiles, percentage of non-uniform reduction, SNR, and SAR will be considered.

(c) To explore the feasibility of using 3D TRF pulses to reduce the B_1 inhomogeneity at the field beyond 3T. The pulses will be tested using Bloch equation simulations and a doped phantom of large diameter constructed to simulate wave effects in higher field MRI. The experiments will be performed in the approach similar to that used for 3T.

2.0 BACKGROUND

2.1 INTRODUCTION

This chapter will provide general background information about MRI. This information will serve as the building blocks for chapters 3 through 6. Major topics of this chapter include physics of MRI, MR excitation, imaging principles, fast imaging techniques, and multi-dimensional selective excitation. The section on the physics of MRI will detail the nuclear spin systems, the interaction of spins with magnetic fields, the behavior of spins after they are excited, and the Bloch equation which describes time dependence of magnetization in a magnetic field. MR excitation section will confer the basic excitation, the rotating frame of reference which eases the concept of excitation effect on a Radio frequency (RF) pulse, the selective excitation as well as the small tip angle approximation which facilitates the RF pulse design. Imaging principles will be discussed with regard to the derivation of signal equation, as well as the relationship between magnetization, Fourier interpretation and sampling requirements. The section on fast imaging techniques will discuss about two best known imaging techniques including spiral imaging and Echo-planar imaging. The chapter will conclude with information about multi-dimensional selective excitation, which is the main focus of the thesis. Examples of applications related to the designs in the later chapters will also be discussed

2.2 PHYSICS OF MRI

2.2.1 Nuclear Spin Systems

The phenomenon of nuclear magnetic resonance arises in nuclei of atoms with an odd number of protons and/or an odd number of neutrons. These nuclei have a property known as spin angular momentum, **S**. Spin angular momentum is a vector quantity expressed as

$$\mathbf{S} = \hbar\mathbf{I} \tag{2.1}$$

where $\hbar$ is Plank's constant (divided by 2π) and **I** is the spin operator in quantum mechanics. Associated with **S** is a magnetic dipole moment μ, where

$$\mu = -\gamma\mathbf{S} = \gamma\hbar\mathbf{I} \tag{2.2}$$

and γ is the gyromagnetic ratio, a known constant unique for different nuclear species. From a classical point of view, one can imagine a charged sphere spinning about its axis, thereby giving rise to a current loop that creates the magnetic dipole moment. Generally, to obtain the MR signal, the nuclei need to interact with three types of magnetic fields: 1) static main magnetic fields (B_0), 2) RF fields (B_1) and 3) linear gradient fields (G).

2.2.2 Interaction with external magnetic fields

Three major types of magnetic fields including main magnetic field B_0 field, Radio frequency field or B_1 field and gradient fields, **G** interact with the nuclei to generate the MR signal.

From a classical viewpoint, at the presence of Main Field, B_0, μ aligns in the direction of the applied field; therefore, per unit volume, magnetization $M = \sum \mu$, and the torque that M experiences from the external B_0 results in nuclear precession with an angular frequency of

$$\omega_0 = \gamma B_0 \tag{2.3}$$

This is known as the Larmor frequency. For $^1\mathbf{H}$, $\frac{\gamma}{2\pi}$ =42.58 MHz/Tesla; therefore, for the magnetic field strength of 3.0T, the Larmor frequency is 127.74 MHz. Macroscopically, the B_0 field polarizes the sample, including a net magnetization vector pointed in the z-direction with a strength of M_0 [15].

Magnetization is excited as the B_1 field or the RF field is applied at the Larmor frequency (resonance frequency) in the transverse direction. Classically, excitation implies a rotation of *M* by some degree angle. The rotating magnetic field B_1 induces a torque on the magnetization, causing *M* to rotate away from its position of equilibrium along z, while proceeding about the z axis. However, *M* eventually returns to its state of equilibrium along z as a result of the regrowth of the longitudinal component, M_z. The time constant characterizing the return of the magnetization vector along the z direction is called T1. Another phenomenon occurs simultaneously with the regrowth of M_z is the decaying of the transverse component, M_{xy}. The time constant characterizing the decay of the vector component in the transverse (x-y plane) is called T2.

If all spins experience only B_0 and are excited by B_1 fields, the signals generated after excitation at different locations are typically indistinguishable. In MRI, spatial localization is achieved by applying linear gradient magnetic fields in addition to B_1 and B_0. Therefore, the frequency of the spins becomes a function of spatial location. In general, the gradients are time-varying gradients.

For the following equation, let **G**(t) be a gradient oriented in 3D. This gradient consists of three vector components: $G_x\boldsymbol{i}$, $G_y\boldsymbol{j}$ and $G_z\boldsymbol{k}$. When all three gradients are turned on, the total magnetic field can be calculated as

$$\mathbf{B}(\mathbf{r},t) = (B_0 + \mathbf{G}(t)\cdot\mathbf{r})\mathbf{k} \tag{2.4}$$

Thus, the general solution for the transverse component derived from the Bloch equation becomes

$$M(\mathbf{r},t) = M_0(\mathbf{r})e^{-t/T_2(\mathbf{r})}e^{-i\omega_0 t}e^{-i\int_0^t \Delta\omega(\mathbf{r},t)d\tau} \tag{2.5}$$

where $\Delta\omega(\mathbf{r},t) = \gamma\Delta B(\mathbf{r},t)$.

Further details of the Bloch equation are described in section 2.2.4.

2.2.3 Relaxation

Following an excitation, M_z returns to its equilibrium state, called longitudinal relaxation. At the same time, the transverse component, M_{xy}, decays away, and this state is called transverse relaxation.

The longitudinal magnetization behaves according to

$$\frac{dM_z}{dt} = -\frac{M_z - M_0}{T1} \tag{2.6}$$

The solution of this equation is

$$M_z = M_0 + (M_z(0) - M_0)e^{-t/T1} \tag{2.7}$$

Following a 90 ^{o} RF pulse, $M_z(0) = 0$; hence,

$$M_z = M_0(1 - e^{-t/T1}) \tag{2.8}$$

,where $T1$ is the spin–lattice time constant, characterizing the recovery to equilibrium along the B_0 direction, and M_0 is magnetization along z at thermal equilibrium. Note that $T1$ is dependent upon the field strength because a greater energy exchange is required at higher frequencies than

at lower frequencies and the relaxation effect takes longer at higher fields than lower ones. The behavior of longitudinal relaxation shows in Figure 2.1.

The behavior of the destructive transverse magnetization can be described by

$$\frac{dM_{xy}}{dt} = -\frac{M_{xy}}{T2} \tag{2.9}$$

The solution after 90^o pulse is

$$M_{xy} = M_0 e^{-t/T2} \tag{2.10}$$

where $T2$ is the spin-spin time constant, characterizing the decay of the transverse magnetization. The decay is caused by loss of phase coherence; thus, $T2$ is independent of field strength. The behavior of the transverse component decay shows in Figure 2.2.

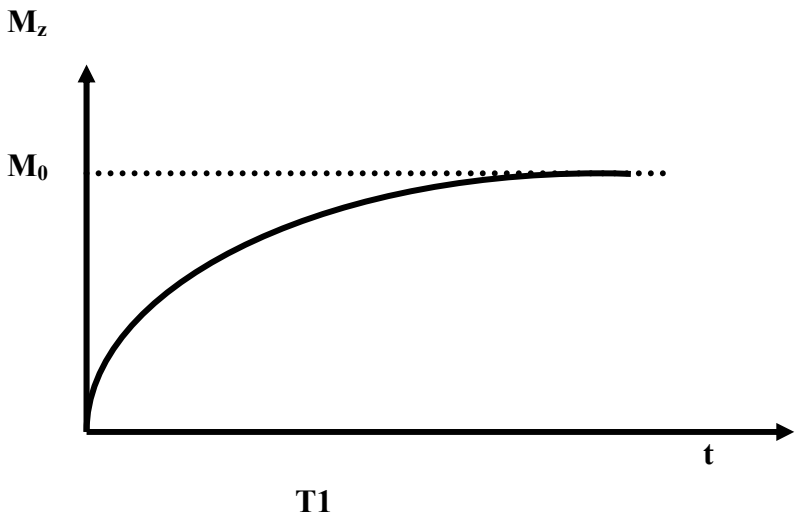

Figure 2.1 Longitudinal relaxation characterized by time constant T1

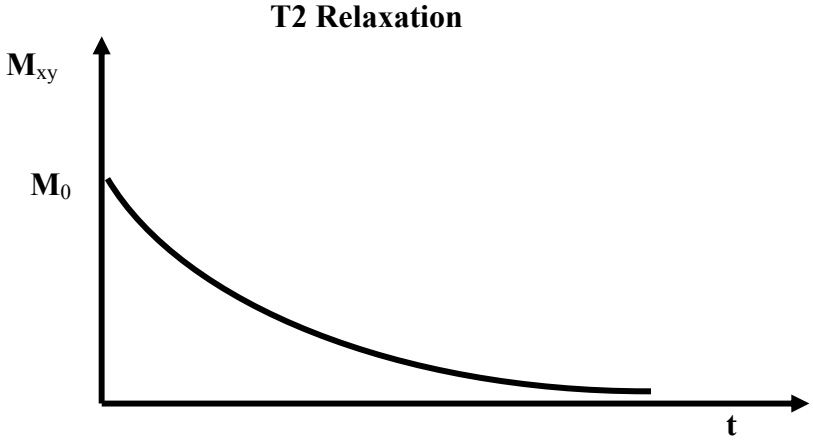

Figure 2.2 Transverse relaxation characterized by time constant T2

2.2.4 The Bloch Equation

The time-dependent phenomenon of magnetization in the presence of an applied magnetic field $\boldsymbol{B}_1(t)$ is described quantitatively by the Bloch equation:

$$\frac{d\mathbf{M}}{dt} = \gamma \mathbf{M} \times \mathbf{B} - \frac{M_x \mathbf{i} + M_y \mathbf{j}}{T2} - \frac{(M_{z'} - M_0)\mathbf{k}}{T1} \tag{2.11}$$

i, **j** , **k** are unit vectors in x, y, z directions, respectively.

B consists of three types of magnetic field: a. $\mathbf{B}_0$, the main magnetic field; b. $\mathbf{B}_1(t)$, RF fields; and c. **G**(t), gradient fields.

The Bloch equation describes the precessional behavior of magnetization with regard to the cross product term and the exponential manners of both the longitudinal and transverse components with the relaxation terms.

2.3 EXCITATION

The external force of magnetization in the presence of the B_0 field comes from an oscillating magnetic field denoted as $\boldsymbol{B}_1(t)$. A classical model suggests that $\boldsymbol{B}_1(t)$ rotates with the Larmor frequency. However, based on a quantum mechanic model, the electromagnetic radiation of frequency ω_{rf} carries energy (Planck's law):

$$E_{rf} = \hbar\omega_{rf} \tag{2.12}$$

To induce a coherent transition of spins from one energy state to another, the radiation energy must be equal to the energy difference, ΔE, between the adjacent spin states. That is,

$$\hbar\omega_{rf} = \Delta E = \gamma\hbar B_0 \tag{2.13}$$

or

$$\omega_{rf} = \omega_0 \tag{2.14}$$

Equation (2.14) defines what is known as the resonance condition. In the most basic case, the RF field is turned on with only the B_0 present, exciting all spins in the volume in the same way. This type of excitation is referred to as non-selective excitation. Generally, the RF pulse is turned on with a gradient, exciting spins in only an specific region of the volume, typically a plane. Such an excitation is called selective excitation.

2.3.1 Basic excitation principles

The simplest form of excitation is to excite the magnetization with B_1 field tuned to Larmor frequency at the presence of only B_0 field as a whole volume excitation. This type of excitation has no restricted region of excitation.

The general formulation of excitation to be considered here is an amplitude-modulated RF pulse, $\boldsymbol{B}_1(t)$, applied in the transverse direction. A typical $\mathbf{B}_1(t)$ is in a linear polarized magnetic field [16]:

$$\mathbf{B}_1(t) = 2B_1(t)\cos\omega_{rf}t\mathbf{i} \tag{2.15}$$

$B_1(t)$ is an amplitude modulation function, also known as a pulse envelop function, and ω_{rf} is the carrier frequency of the excitation. This linearly polarized field decomposes into two circularly polarized fields. One is a clockwise rotating field, and the other is a counterclockwise rotating field. Mathematically, the $\mathbf{B}_1(t)$ field can be rewritten as:

$$\mathbf{B}_1(t) = B_1(t)[\cos\omega_{rf}t\mathbf{i} - \sin\omega_{rf}t\mathbf{j}] + B_1(t)[\cos\omega_{rf}t\mathbf{i} + \sin\omega_{rf}t\mathbf{j}] \tag{2.16}$$

where the first bracketed term represents the clockwise rotating field and the second bracketed term represents the counterclockwise rotating field. Hoult and Yang have named each of the two fields after their rotating directions, $B_1^+(t)$ and $B_1^-(t)$, for the counterclockwise and clockwise rotating fields, respectively. Since the counterclockwise component has a negligible effect on the spins [15, 16] , the effective $\mathbf{B}_1$(t) field becomes

$$\mathbf{B}_1(t) = B_1(t)[\cos\omega_{rf}t\mathbf{i} - \sin\omega_{rf}t\mathbf{j}] \tag{2.17}$$

The x-component is

$$B_{1,x}(t) = B_1(t)\cos(\omega_{rf}t) \tag{2.18}$$

and the y-component is

$$B_{1,y}(t) = -B_1(t)\sin(\omega_{rf}t) \tag{2.19}$$

Thus, in a complex notation, the $\mathbf{B}_1$(t) is:

$$\mathbf{B}_1(t) = B_1(t)e^{-i\omega_{rf}t} \tag{2.20}$$

In summary, an RF pulse generates an oscillating $\mathbf{B}_1(t)$ field perpendicular to the $\mathbf{B}_0$ field. Assuming the initial phase is zero, the RF pulse is characterized by two parameters: the envelope function, $B_1(t)$, and the carrier frequency, ω_{rf}. The excitation frequency, ω_{rf}, is generally constant and is determined by the resonance condition. The most important part of an RF pulse is the resulting envelope function. It uniquely specifies the shape and duration of an RF pulse, thus determining its excitation property.

2.3.2 Rotating frame of reference

The rotating frame of reference is used for conceptual simplicity in describing the excitation effect on an RF pulse. A rotating frame is a coordinate system in which the transverse plane typically rotates clockwise about the z axis at an angular frequency, ω. Let x', y', z' represent a rotating coordinate system and $\mathbf{i}', \mathbf{j}', \mathbf{k}'$ be the corresponding unit vectors along the three axes. A rotating frame is related to a lab frame or stationary frame by the following transformation:

$$\begin{aligned} \mathbf{i}' &= \cos(\omega t)\mathbf{i} - \sin(\omega t)\mathbf{j} \\ \mathbf{j}' &= \sin(\omega t)\mathbf{i} + \cos(\omega t)\mathbf{j} \\ \mathbf{k}' &= \mathbf{k} \end{aligned} \tag{2.21}$$

Let $\mathbf{M}$ be a magnetization in the lab frame denoted by:

$$\mathbf{M} = M_x\mathbf{i} + M_y\mathbf{j} + M_z\mathbf{k} \tag{2.22}$$

and $\mathbf{M}_{rot}$ be a magnetization in the rotating frame described by:

$$\mathbf{M}_{rot} = M_{x'}\mathbf{i}' + M_{y'}\mathbf{j}' + M_{y'}\mathbf{k}' \tag{2.23}$$

Setting $\mathbf{M}=\mathbf{M}_{rot}$ yields

$$\begin{bmatrix} M_{x'} \\ M_{y'} \\ M_{z'} \end{bmatrix} = \begin{bmatrix} \cos(\omega t) & -\sin(\omega t) & 0 \\ \sin(\omega t) & \cos(\omega t) & 0 \\ 0 & 0 & 1 \end{bmatrix} \begin{bmatrix} M_x \\ M_y \\ M_z \end{bmatrix} \tag{2.24}$$

Likewise, for $\mathbf{B}_1$ and $\mathbf{B}_{1,\,\mathrm{rot}}$

$$\mathbf{B}_1 = B_{1,x}\mathbf{i}, B_{1,y}\mathbf{j} \tag{2.25}$$

and

$$\mathbf{B}_{1,rot} = B_{1,x'}\mathbf{i}', B_{1,y'}\mathbf{j}' \tag{2.26}$$

Then

$$\begin{bmatrix} B_{1,x'} \\ B_{1,y'} \end{bmatrix} = \begin{bmatrix} \cos\omega t & -\sin\omega t \\ \sin\omega t & coa\omega t \end{bmatrix} \begin{bmatrix} B_{1,x} \\ B_{1,y} \end{bmatrix} \tag{2.27}$$

Equations (2.24) and (2.27) are used to convert a magnetization vector and B_1 between the lab frame and the rotating frame. The transformation can also be expressed in a complex notation as:

$$M_{x'y'} = M_{xy}e^{i\omega t} \tag{2.28}$$

where $M_{xy} = M_x + iM_y$ and $M_{x'y'} = M_{x'} + iM_{y'}$ and

$$B_{1,rot} = B_1(t)e^{i\omega t} \tag{2.29}$$

where $B_1 = B_{1,x} + iB_{1,y}$ and $B_{1,rot} = B_{1,\,x'} + iB_{1,\,y'}$.

Ignoring the relaxation terms, the Bloch equation in the rotating frame can be rewritten as:

$$\frac{\partial \mathbf{M}_{rot}}{dt} = \gamma \mathbf{M}_{rot} \times \mathbf{B}_{eff} \tag{2.30}$$

where

$$\mathbf{B}_{eff} = \mathbf{B}_{rot} + \frac{\boldsymbol{\omega}}{\gamma} \tag{2.31}$$

This derivation is in Appendix A.

$\mathbf{B}_{eff}$ is the effective magnetic field that the bulk magnetization experiences in the rotating frame. Following the same analysis, the general Bloch equation can be expressed in the rotating frame as:

$$\frac{\partial \mathbf{M}_{rot}}{dt} = \gamma \mathbf{M}_{rot} \times \mathbf{B}_{eff} - \frac{M_x \mathbf{i} + M_y \mathbf{j}}{T2} - \frac{(M_{z'} - M_0)\mathbf{k}'}{T1} \tag{2.32}$$

2.3.3 On resonance excitation

The condition that $\mathbf{B}_1(t)$ is tuned to the Larmor frequency is known as an on resonance excitation. Given that the far smaller magnetic field of RF pulse is able to tip the magnetization in the much higher magnetic field, B_0. This can be explained by the following mathematic equations.

Equation (2.17) can be expressed as:

$$\begin{bmatrix} B_{1,x} \\ B_{1,y} \end{bmatrix} = \begin{bmatrix} B_1 \cos \omega_{rf} t \\ -B_1 \sin \omega_{rf} t \end{bmatrix} \tag{2.33}$$

Substituting Equation (2.33) into Equation (2.27) when B_1 is in the rotating frame yields

$$B_{1,rot} = \begin{bmatrix} B_{1,x'} \\ B_{1,y'} \end{bmatrix} = \begin{bmatrix} \cos \omega_{rf} t & -\sin \omega_{rf} t \\ \sin \omega_{rf} t & coa\omega_{rf} t \end{bmatrix} \begin{bmatrix} B_1 \cos \omega_{rf} t \\ -B_1 \sin \omega_{rf} t \end{bmatrix} = \begin{bmatrix} B_1 \\ 0 \end{bmatrix} = \begin{bmatrix} B_1 \mathbf{i}' \end{bmatrix} \quad (2.34)$$

Therefore, the effective field (Equation(2.31)) in the rotating frame becomes

$$\mathbf{B}_{eff} = (B_0 - \frac{\omega_{rf}}{\gamma})\mathbf{k}' + B_1 \mathbf{i}' \tag{2.35}$$

If $\omega_{rf} = \omega_0$ is an on resonance excitation condition, then $\mathbf{B}_{eff} = B_1 \mathbf{i}'$.

For a general $B_1(t)$, the angular rotation becomes $\omega_1(t) = \gamma B_1(t)$. If the $B_1(t)$ is on for time τ, then the tip angle derived from the solution of the Bloch equation is

$$\alpha = \int_0^{\tau} \omega_1(s)ds \tag{2.36}$$

and, for a constant B_1,

$$\alpha = \omega_1 \tau$$

2.3.4 Selective excitation

In the stated above of excitation, the RF pulse tuned to the Larmor frequency excites all spins at the presence of B_0 for the entire volume. However, in the selective excitation approach, only the selected region is excited. This can be accomplished by applying the RF pulse with the modulation function $B_1(t)$ in the presence of a gradient magnetic field [17], typically G_z, Therefore, only those spins lying in the z location with resonance frequencies that match the temporal frequencies of the $B_1(t)$ will be excited. Spins which have resonance frequencies outside the excitation bandwidth will be unaffected.

The general formulation of the selective excitation is similar to those of the basic excitation as described in the previous section. The additional feature of the magnetic gradient field typically G_z, a term added to the z component. As a result, $\mathbf{B}_{eff}$ from Equation (2.35) becomes

$$\mathbf{B}_{eff} = (B_0 - \frac{\omega_{rf}}{\gamma} + \gamma G_z z)\mathbf{k}' + B_1\mathbf{i}' \tag{2.37}$$

Now, the Bloch equations in the rotating frame, ignoring relaxation terms, in a matrix form are

$$\frac{\partial M_{rot}}{dt} = \begin{bmatrix} 0 & \omega_0 - \omega_{rf} + \omega(z) & 0 \\ -(\omega_0 - \omega_{rf} + \omega(z)) & 0 & \omega_1(t) \\ 0 & -\omega_1(t) & 0 \end{bmatrix} \begin{bmatrix} M_{x'} \\ M_{y'} \\ M_{z'} \end{bmatrix} \tag{2.38}$$

where $\omega(z)=\gamma G_z z$. If the excitation frequency is tuned to the central Larmor frequency, such that $\omega_{rf} = \omega_0$, then the Bloch equation becomes

$$\frac{\partial M_{rot}}{dt} = \begin{bmatrix} 0 & \omega(z) & 0 \\ -\omega(z)) & 0 & \omega_1(t) \\ 0 & -\omega_1(t) & 0 \end{bmatrix} \begin{bmatrix} M_{x'} \\ M_{y'} \\ M_{z'} \end{bmatrix} \tag{2.39}$$

Here, the Bloch equation is a function of *ω(z)* and the magnitude of each *ω(z)* is determined by its corresponding location along z. In principle, the selective excitation case can be solved for different z positions, each corresponding to a different offset frequency.

2.3.5 Small tip angle approximation

Small tip angle approximation has been employed in many applications in order to separate the B_1 field calculation from the magnetization. Since Equation (2.39) has no closed-form solution, a numerical calculation is required to solve this equation. A few assumptions, such as initial condition and flip angle, need to be made in order to solve for the equation [18, 19].

Assumptions:

1. The initial condition is $\mathbf{M}_{rot} = \begin{bmatrix} 0 \\ 0 \\ M_0 \end{bmatrix}$ at equilibrium.

2. The RF flip angle is small, generally less than 30 degree.

With these assumptions, the magnetization along z, M_z, can be approximated as equal to the magnetizations at thermal equilibrium M_0, ($M_z \cong M_0$),and $\frac{dM_{zrot}}{dt} \cong 0$. Therefore, the Bloch equation from Equation (2.39) has only transverse components remaining and can be rewritten as [15]

$$\frac{dM_r}{dt} = -i\omega(z)M_r + i\omega_1(t)M_0 \tag{2.40}$$

where M_r=M_{rot}.

The solution of Equation (2.40) is detailed in Appendix B.

$$M_r(t,z) = iM_0 e^{-i\omega(z)t} \int_0^t e^{i\omega(z)\tau} \omega_1(\tau) d\tau \tag{2.41}$$

If $B_1(t)$ is on from $t=0$ *to* τ, then at $t = \tau$, (derivation from Equation (2.41) to Equation (2.42) can be found from reference [15])

$$M_r(\tau,z) = iM_0 e^{-i\omega(z)\frac{\tau}{2}} \mathrm{FT}_{1D}\{\omega_1(t+\frac{\tau}{2})\}_{f=-f(z)=-\frac{\gamma}{2\pi}G_z z} \tag{2.42}$$

It is clear that with the small tip angle, the slice profile at a particular z location has a Fourier Transform relationship with $B_1(t)$. This relationship is very useful in that it facilitates the design of $B_1(t)$.

If the signal immediately after the selective excitation pulse were to be sampled, it would be relatively weak due to the signal loss caused by phase dispersion across the finite slice width represented by the phase factor $exp(-i\omega(z)\tau/2)$, as shown in Equation (2.42). To obtain a higher signal, the magnetization needs to be refocused. To refocus, the phase factor term needs to be in the opposite sign as $exp(+i\omega(z)\tau/2)$, and the area under the refocusing lobe should be one-half of the area under the selective excitation lobe [20].

2.4 IMAGING PRINCIPLES

This section will discuss the derivation of the signal equation. The solution of the Bloch equation in the presence of the gradient field will be exploited for the derivation. This section also will

describe the basic principles of MR imaging. The elegant Fourier interpretation of the signal will provide the structure of MR imaging. The ramifications of this signal on parameters such as spatial resolution and image field of view will also be discussed.

2.4.1 Signal detection and reciprocity law

According to Faraday's Law, if a source is producing a magnetic field, then we can measure how much flux it will generate through a coil by measuring the voltage across the coil. In magnetic resonance imaging, we measure the voltage or signal from the coil and determine the magnetic fields (in our case, spin distribution) producing such a signal. According to the principle of reciprocity, if there are two identical coils, A and B, if coil A can produce flux through coil B, then coil B can also produce an identical amount of flux through coil A [21] and the flux,Φ is defined as

$$\Phi = \int \mathbf{B} \cdot d\mathbf{a} ,$$

where **B** is the magnetic field perpendicular to the coil, and **a** is the surface area of the coil. In MRI, generally the same RF coil is used for excitation and detection; therefore, the flux detected by the receiving coil can be determined through the principle of reciprocity [21] as:

$$\Phi(t) = \int \mathbf{B}_r(\mathbf{r}) \cdot \mathbf{M}(\mathbf{r},t) d\mathbf{r} \tag{2.43}$$

where $\mathbf{B}_r(r)$ is the laboratory frame magnetic field at location **r** per unit of direct current flowing in the coil and $\mathbf{M}(\mathbf{r},t)$ is the magnetization that produces the magnetic flux through the coil. Since the M_z component of $M_z(\mathbf{r},t)$ is a slowly varying function compared to the free precession of the M_x and M_y components, the M_z component can be ignored. Therefore, after the

demodulation of the high frequency term, the signal equation in rotating frame with Gradient Echo sequence becomes [16]

$$s(t) = i\omega_0\gamma \int C(\mathbf{r}) \cdot \mathbf{M}(\mathbf{r},t) \cdot \sin(\alpha(\mathbf{r})) \cdot e^{-i\gamma \int_0^t \mathbf{G}(\tau)\cdot\mathbf{r}d\tau} d\mathbf{r} \tag{2.44}$$

where $C(\mathbf{r})$is spatial coil sensitivity, and $\alpha(\mathbf{r}) = \gamma \int_0^{\tau} B(\mathbf{r},t)dt$ is the flip angle.

Mansfield [22] introduces the concept of a reciprocal space vector, **k**, given that

$$\mathbf{k}(t) = \frac{\gamma}{2\pi} \int_0^t \mathbf{G}(\tau)d\tau \tag{2.45}$$

Thus Equation (2.44)becomes

$$s(t) = i\omega_0\gamma \int C(\mathbf{r}) \cdot \mathbf{M}(\mathbf{r},t) \cdot \sin(\alpha(\mathbf{r})) \cdot e^{-i\cdot 2\cdot\pi\cdot\mathbf{k}(t)\cdot\mathbf{r}} d\mathbf{r} \tag{2.46}$$

The k-vector has a unit of the reciprocal space or spatial frequency. Therefore the signal equation in Equation (2.46) can be written in the k-space or Fourier domain as

$$S(\mathbf{k}) = i\omega_0\gamma \int C(\mathbf{r}) \cdot \mathbf{M}(\mathbf{r},t) \cdot \sin(\alpha(\mathbf{r})) \cdot e^{-i\cdot 2\cdot\pi\cdot\mathbf{k}\cdot\mathbf{r}} d\mathbf{r} \tag{2.47}$$

and

$$M(\mathbf{r}) = C'(\mathbf{r}) \int S(\mathbf{k}) \cdot e^{i\cdot 2\cdot\pi\cdot\mathbf{k}\cdot\mathbf{r}} d\mathbf{r} \tag{2.48}$$

where

$$C'(\mathbf{r}) = 1 / i\omega_0\gamma C(\mathbf{r}) \sin(\alpha(\mathbf{r}))$$

and

$$s(t) = S(k(t)) = S(\frac{\gamma}{2\pi} \int_0^t G(\tau)d\tau) \tag{2.49}$$

Note that the magnetization, $M(\mathbf{r})$ and the signal, S(t) are mutually conjugate. This relationship is of critical importance to MR imaging.

2.4.2 Fourier interpretation of the signal equation

Equation(2.46) shows that at any given time t, $s(t)$ equals the Fourier transformation of the magnetization at a particular spatial frequency. Equation(2.49) demonstrates that the total recorded signal $s(t)$ maps directly to a trajectory through spatial frequency space, as determined by the time integrals of the applied gradient waveform $\mathbf{G}(t)$. To form an image, the trajectories corresponding to a set of $s(t)$ are required to cover a sufficient part of k-space to allow reconstruction of $M(\mathbf{r})$. Figures 2.3 and 2.4 illustrate examples of 2D Fourier Transform sequences. Figure 2.3(a) displays the timing diagram of the basic 2D Fourier Transform (2DFT) sequence. Figure 2.3(b) shows the corresponding k-space trajectory from a $\longrightarrow$ b $\longrightarrow$ c. Figure 2.4 illustrates the timing diagram and the k-space trajectory which cover full 2D k-space. The most common image reconstruction in MRI is 2DIFT which performs 2DFT of the 2D k-space to obtain an image.

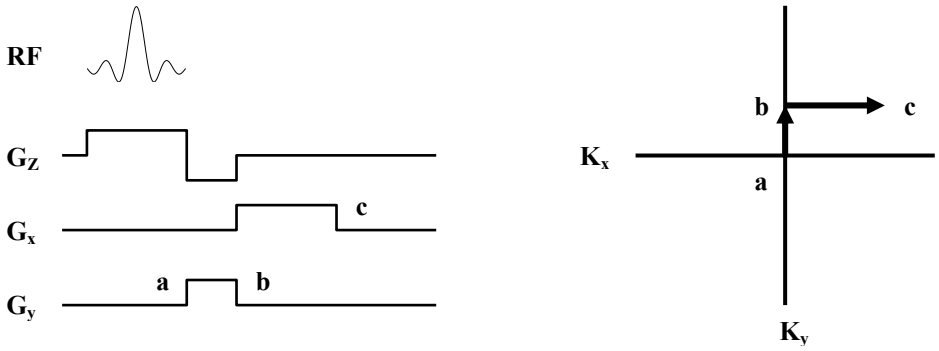

(a) *from Nishimura's Principles of Magnetic Resonance Imaging [48]* **(b)**

Figure 2.3(a) Timing diagram, (b) k-space

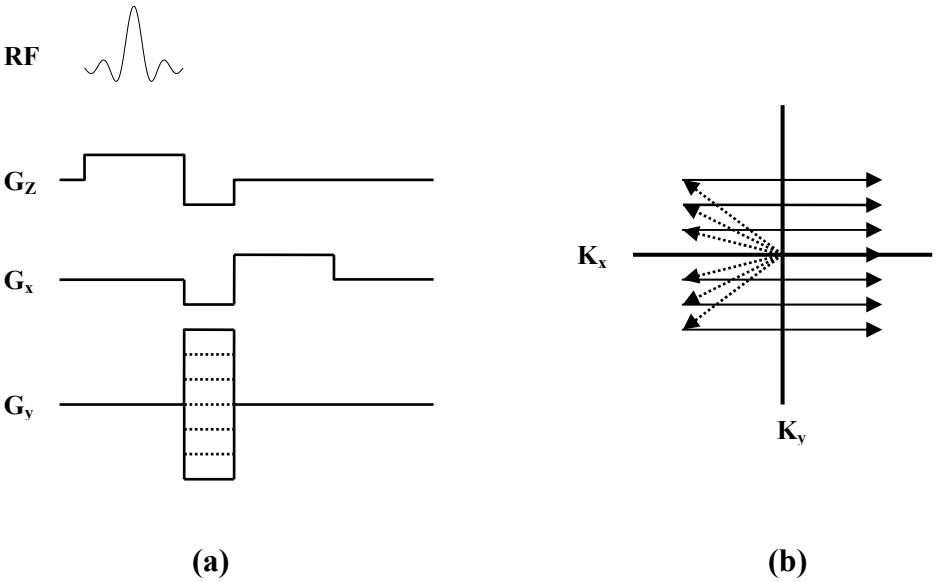

(a) **(b)**

Figure 2.4(a) Timing diagram, (b) k-space

2.4.3 Sampling requirements in 2DFT imaging

The sampling requirements here address only the case of uniform sampling in 2D imaging with a Cartesian grid. The sampling in each dimension can be treated separately. This concept can be easily extended to higher dimensional cases. This assumes that the object being imaged has fields of view (FOV) along the x and y directions denoted by *FOVx* and *FOVy,* respectively, and the x direction is used for frequency encoding while y direction is used for phase encoding. To meet the Nyquist criteria,

$$\Delta k_x \le \frac{1}{FOVx} \quad \text{and } \Delta k_y \le \frac{1}{FOVy} \tag{2.50}$$

and

$$\begin{aligned} \Delta k_x &= \gamma \left| G_x \right| \Delta t \\ \Delta ky &= \gamma \Delta G_y \tau_p \end{aligned} \tag{2.51}$$

where

Δk_x and Δk_y are step sizes of the k-space along x and y directions, respectively

G_x is frequency-encoding gradient

ΔG_y is phase-encoding gradient step size

Δt is readout sampling time interval

τ_p is phase-encoding interval

Substituting Equation (2.51)into Equation (2.50) sets the following requirements for the data acquisition parameters:

$$\begin{aligned} \Delta t &\le \frac{2\pi}{\gamma \left| G_x \right| FOVx} \\ \Delta G_y &\le \frac{2\pi}{\gamma \tau_p FOVy} \end{aligned} \tag{2.52}$$

2.5 FAST IMAGING

The basic imaging sequence discussed in section 2.3 requires relatively long scan time to cover the full k-space because the readout performs on one single line in k-space at a time and the interval (TR) between readouts is long. However, many applications require fast scanning to overcome motion effects such as cardiac MRI or to capture dynamic events. To achieve this goal, a greater portion of k-space per readout is required and /or to shorten the interval between signal generation [15]. This can be done by having an appropriate modulation of the gradient waveforms to control the k-space trajectory. The most common trajectories used in fast imaging are spiral trajectory [23, 24] and Echo-Planar proposed by Mansfield [25].

2.5.1 Spiral trajectory

Figure 2.5 shows a type of radial scan known as a spiral trajectory. The trajectory starts at the origin of the k-space and spirals outward (Figure2.5(a)). The corresponding gradients (Figure2.5(b)) are a pair of increasing sinusoidal gradients. This trajectory provides the entire k-space in a single readout.

2.5.2 Echo-planar trajectory

Figure 2.6 shows a Cartesian scan called the Echo-planar with its gradient waveforms. This trajectory is characterized by the acquisition of multiple raster lines per excitation. Initial movement is to the bottom of the k-space, then the scan traverses each line along k_x before blipping upwards in the k_y direction.

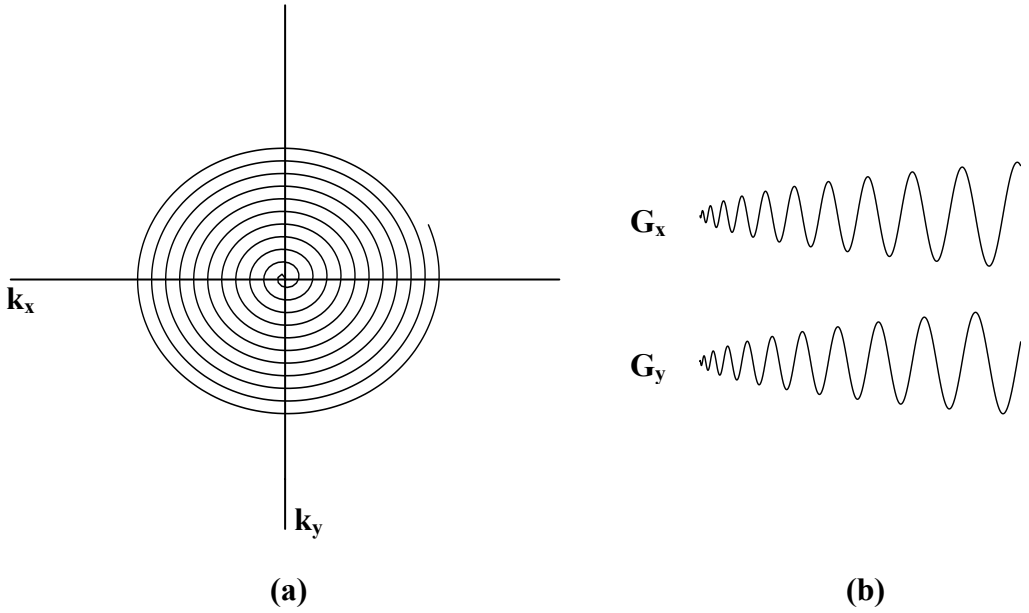

Figure 2.5 (a) Spiral k-space trajectory, (b) Gradient waveforms corresponding to the spiral k-space

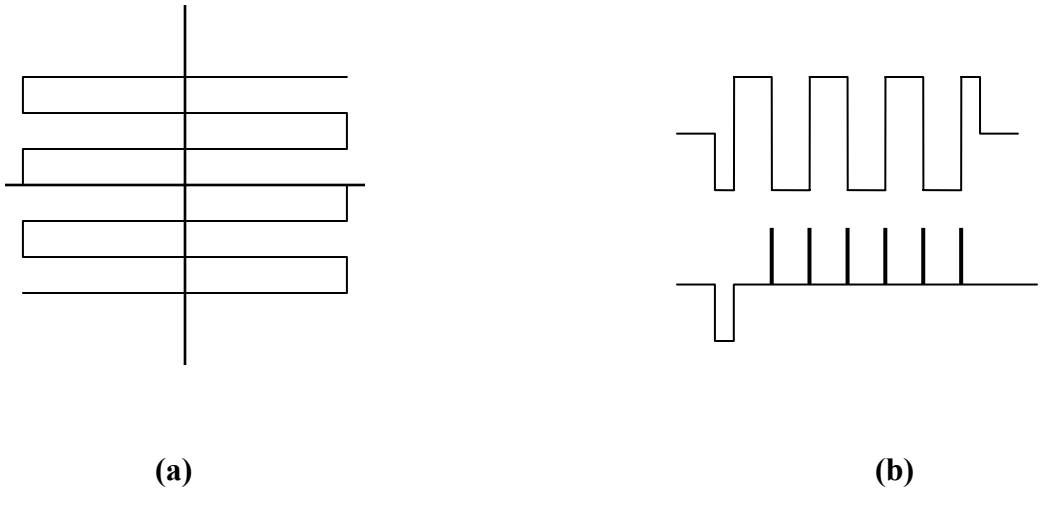

Figure 2.6 (a) Echo-planar trajectory, (b) Gradients waveforms of the Echo-planar trajectory

2.6 MULTI-DIMENSIONAL SELECTIVE EXCITATION

The concept of this excitation involves the limited area to be excited or refocused not only in the z direction but also in the transverse direction [20, 26-29]. The spatial selectivity of the multi-dimensional RF pulse is achieved by the application of appropriate gradients simultaneously with the RF waveform. An example of the gradient waveform which is generally employed in most applications is the spiral gradient [28]. A couple of examples of multi-dimensional selective excitation and their applications will be presented in the following sections.

2.6.1 2D Curved-slice excitation

Bornert [27, 28, 30] applies the 2D RF pulse to excite curvature objects in 3D space. The pulses have two major components, 2D gradients such as spiral or Echo-planar trajectories and RF pulse waveforms. The two components must be applied simultaneously in order for 2D selective excitation to occur. The 2D RF pulse aims to excite the anatomical structures often embedded in curved surfaces. By using this pulse, the curved structure can be excited and measured as a projection on a selected imaging plane. In 3D space, the curved structure excited by the 2D RF pulse is considered to be a chain of N voxels, restricted by conventional frequency encoding in the third spatial direction.

2.6.2 3D Slice-select Tailored RF (TRF) pulses

Stenger, *et al*. [31, 32] present another application of multidimensional excitation. The design of the 3D slice-select tailored RF (TRF) pulses is based on small tip angle approximation [20]. In 3D space, the pulse selectively excites when the 3D stacked spiral k-space is applied at the same

time as the 3D TRF pulse waveform. The long pulse length problem due to sampling resolution constraint is overcome by breaking up the pulse into orthogonal components, called multi-shot 3D TRF pulse that excites the slice in separate acquisitions. The final image is obtained by the summation of the complex image data. This pulse can be used for T2*-weighted functional MRI in brain regions corrupted by intravoxel dephasing artifacts due to susceptibility variations.

2.6.3 Stacked spiral k-space

The stacked spiral k-space is one of the fastest known trajectories through 3D k-space [33]. The trajectory is created from 2D spiral trajectories in k_x-k_y and gradient "blips" along k_z such that a cylindrical k-space volume is covered. The 2D spiral trajectories design uses the analytical algorithm developed by Glover [34]. In creating his algorithm, Glover modified the slew rate-limited algorithm of Duyn and Yang [35], which has a singularity problem at origin, with a smoother transition function near the origin. However, at a particular time when it is determined that the gradient magnitude will exceed the maximum allowed, the algorithm switches to an amplitude-limited function. In brief, this algorithm includes a modified slew rate-limited case for the trajectories near origin and switches to an amplitude-limited case when the maximum allowed gradient is being reached. The 2D spiral k-space can also be split into several interleaves for multi-shot excitation and/or interleaves acquisition. Figure 2.7 shows examples of stacked spiral k-space. Figures 2.7(a) and (b) show single shot and a two shot spiral k-spaces respectively. Figures 2.7(c) and (d) show top views of the corresponding spiral k-spaces.

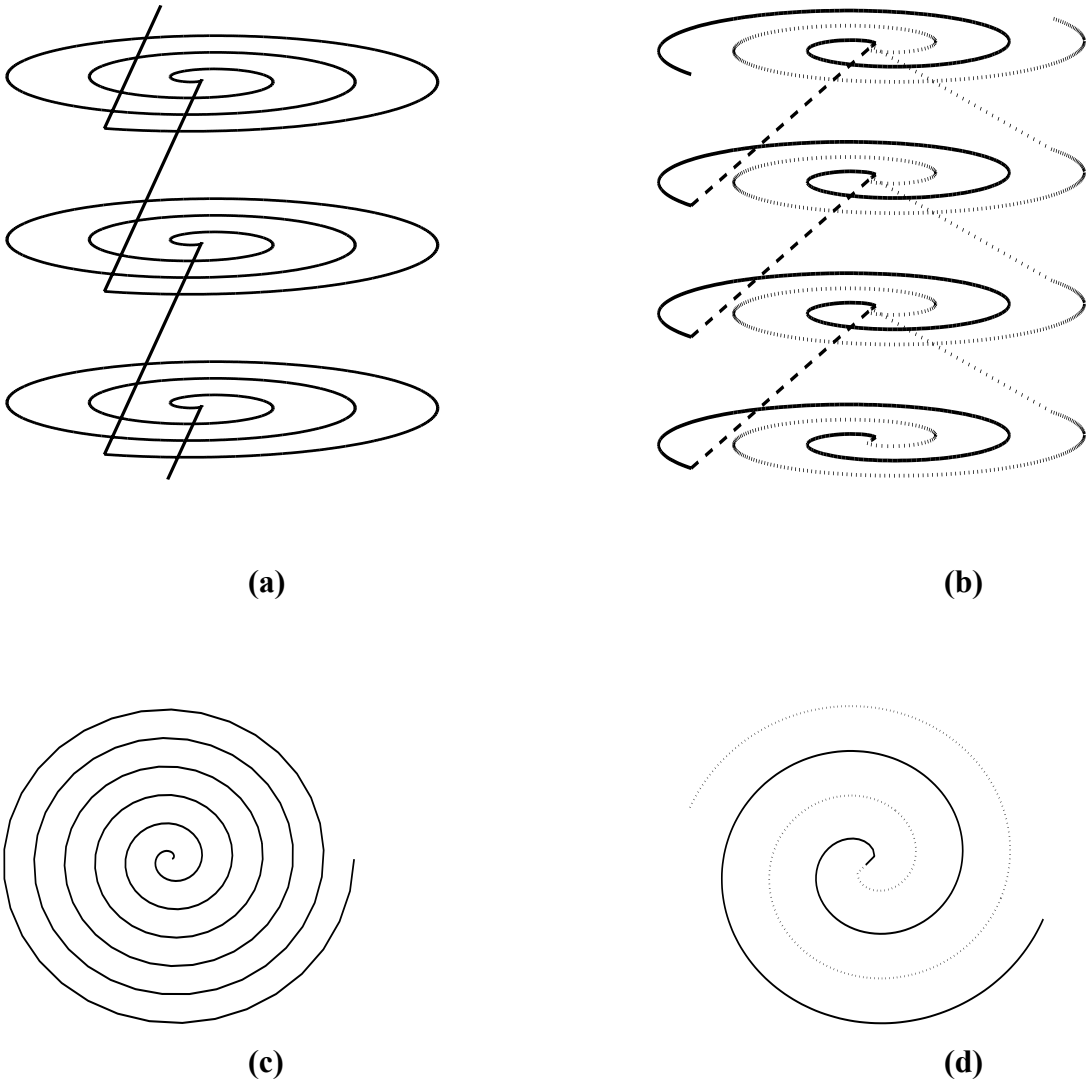

Figure 2.7 (a) Single shot stacked spiral k-space, (b) Two shot stacked spiral k-space, (c) Top view of a single shot 2D spiral k-space, (d) Top view of a two shot stacked spiral k-space

Stenger *et al* applies the 3D slice-selective TRF pulse waveform for B_0 field inhomogeneity reduction [31, 32]. An example of the desired 3D magnetization profile that matches the stacked spiral k-space is a Circ function in the x-y direction and a Gaussian function in the z direction. Mathematically, this description can be expressed as:

$$B_1(t) \propto \Delta(\mathbf{k}(t))\left|\mathbf{G}(t)\{\int M_{xy}(\mathbf{r})e^{i.\mathbf{k}(t).\mathbf{r}}d\mathbf{r}\}\right| \tag{2.53}$$

where $$\mathbf{k}(t) = -\gamma \int_{t}^{T} \mathbf{G}(s) ds$$

Above, $\Delta\mathbf{k}(t)$ is a sample density correction term, and **G**(t) represents the gradients that are applied simultaneously to $B_1(t)$. $M_{xy}(r)$ is the desired complex transverse magnetization. The k-space vector **k**(t) is determined by the area remaining of the of the gradients at time t. Any arbitrary analytical or numerical form for M_{xy}(r) can be used as long as the sampling requirements are satisfied for the resolution of M_{xy}(r) and for the 3D FOV of the area being imaged. An example of the Circ function for M_{xy}(r) at a particular z location in the cylindrical coordinate can be written as:

$$M_{xy}(\rho, z) = \exp\left[-\pi(z / z_0)^2\right] circ(\rho / \rho_0) \tag{2.54}$$

where z_0 and ρ_0 are the slice thickness and the in-plane radius of the disk respectively. The Circ function is defined as being 0 when $\rho > \rho_0$ and 1 when $\rho \le \rho_0$.

3.0 MAGNETIC RESONANCE IMAGING CONSIDERATION IN HIGH FIELD MRI

3.1 INTRODUCTON

This chapter will be discussed about the technical impacts on high field MR imaging and focused more on B_1 inhomogeneity problem. The currently available methods for B_1 inhomogeneity reduction will also be discussed as a comparison for the proposed methods in the next following chapters.

3.2 TECHNICAL IMPACTS ON HIGH FIELD MRI

The technical impacts on high field MRI lead to both benefits and problems in MRI. The technical benefits gained from high field MRI involve increase of SNR, improving of spatial resolution, and reduction of total acquisition time. However, there are a few technical challenges associated with the increased magnetic field strength that need to be resolved such as B_1 inhomogeneity, susceptibility artifacts and high specific absorption rate (SAR). This thesis will be focused on technical development of RF pulse designs which aim to reduce B_1 inhomogeneity

in 3T MRI. The RF pulse design encompasses safety issue which is characterized by SAR as a constraint of the design.

3.2.1 Signal-to-Noise Ratio

One of the major advantages of high field over low field MRIs is the improvement of SNR [1, 2, 36, 37]. This is explained by the relationship of signal equation [7] below:

$$S \propto \rho \frac{\gamma^3 \hbar B_0^2}{4kT} V \tag{3.1}$$

As equation (3.1) shows, the MR signal (S) is quadratically dependent on the static magnetic field (B_0) and is directly proportional to the spin density (ρ) and voxel size (V), where $\gamma, \hbar, k, and\, T$ are gyromagnetic ratio, Planck's constant, Boltzmann's constant, and absolute temperature, respectively. Therefore, if the field strength increases by a factor of two, the signal can be expected to be four times higher. Unfortunately, noise, which is frequency dependent, also increases by a factor of approximately two [38]; therefore, the signal's increase is just twofold.

3.2.2 Improving spatial resolution

The increased SNR associated with increased field strength can improve spatial resolution while maintaining constant SNR and acquisition time. Consequently, the partial volume effect may be reduced [39]. The relationship between SNR and spatial resolution [7, 40] can be written as:

$$SNR_{3D} = \sqrt{\Delta x \Delta y \Delta z}$$
$$SNR_{2D} = s\sqrt{\Delta x \Delta y} \tag{3.2}$$

where SNR_{3D} and SNR_{2D} correspond to SNR of 2D and 3D acquisitions, Δx, Δy, and Δz are voxel-dimensions along x, y and z plane, respectively, and s is slice thickness. Note that SNR depends on slice thickness differently for 2D and 3D approaches. If the field strength increases by a factor of two, the in-plane resolution promisingly reduces by half with no loss of SNR. Along the z-direction, when SNR is constant, the slice thickness can be reduced by a factor of two in 2D and four in 3D cases as the field strength increases by a factor of two. Thus, thin slice and high-resolution images can be achieved with reasonable SNR in high field and ultra-high field MRI.

3.2.3 Shortening data acquisition times

SNR is roughly proportional to the square root of the total data acquisition time [7, 41]. Therefore, reducing the total data acquisition time by a factor of four while maintaining the SNR requires twice as much field strength. Therefore at higher field the reduction in total acquisition time could reduce significant amount of time in the applications which requires numerous signal averages.

3.2.4 B_1 inhomogeneity

As the B_0 field increases, the frequency of B_1 (Radiofrequency) required to excite the magnetization increases linearly. Consequently, the effective wavelength of the B_1 field becomes comparable to or less than the dimensions of the human body being studied, due to the body's dielectric and conductive properties [42-44]. Standing waves can be created inside the sample,

along with wave propagation. The resulting images would have regions of increased and decreased magnitudes.

Dielectric resonance and B_1 inhomogeneity

For 3T and 7T MRI scanners, the RF frequencies required to oscillate at resonance are approximately 128 MHz and 300 MHz, respectively. At these frequencies, when the B_1 propagates through mediums, the wavelengths are shorter than their free space wavelengths and their amplitudes are attenuated. This result can be understood by the complex wave number and the plane-wave equations shown below. The complex wave number [45] is calculated using the following equation:

$$\kappa = \kappa_+ + i\kappa_- \quad \kappa_\pm = \omega\sqrt{\frac{\varepsilon\mu}{2}}\left[\sqrt{1+\left(\frac{\sigma}{\varepsilon\omega}\right)^2} \pm 1\right]^{1/2} \tag{3.3}$$

The plane-wave solutions derived from Maxwell's equation (3.3) are

$$E(x,t) = E_0 e^{i(kx-\omega t)}, \qquad B = B_0 e^{i(kx-\omega t)} \tag{3.4}$$

As shown in these equations, if the complex wave number k is substituted in the plane-wave solutions, the imaginary part of k becomes a negative real number and the wave-amplitude decays exponentially as the wave travels into a medium. On the other hand, the real part of k is found to be an imaginary number, and this part determines the wavelength, the propagation speed, and the index of refraction [45]. The wavelength is defined as

$$\lambda = \frac{2\pi}{\kappa_+}, \tag{3.5}$$

For a "poor" conductor

$\sigma << \omega\varepsilon$

$$\kappa_+ \cong \omega\sqrt{\varepsilon\mu}, \quad \kappa_- \cong \frac{\sigma}{2}\sqrt{\frac{\mu}{\varepsilon}} \tag{3.6}$$

where σ = Conductivity

ω = RF frequency

ε = Permittivity

μ = Permeability

As shown in the equation above, wave penetration through this medium is independent of frequency, and the B_1 inhomogeneity typically depends on the standing waves created inside the medium.

For a "good" conductor$\boldsymbol{\sigma >> \omega\varepsilon}$

$$\kappa_+ \cong \kappa_- \cong \sqrt{\frac{\omega\sigma\mu}{2}} \tag{3.7}$$

For a substance which has the conductivity in between good and poor, the calculation of the complex wave number refers to the original equation(3.3). For distilled water, which has a high dielectric constant and zero conductivity, the wavelength of the B_1 field is reduced to 27 cm at 128 MHz [44] and becomes comparable to the dimension of a human head. If the experiment were conducted in a distilled-water phantom of this size, a standing wave would be produced inside the phantom, and it would cause an inhomogeneous RF distribution. However, for human brain tissue, in which the dielectric properties are somewhere between good and poor conductivity [42], the standing wave is not sustained due to strong decay of the RF caused by sample conductivity (the κ_- term). The amplitude distribution of the fields in the head results from both the interference of decayed traveling waves in a given coil configuration and contributions from dielectrically induced standing waves. This effect causes increased signal

intensity in the middle of the image and decreased signal intensity near its edge. This effect is even more severe during ultra-high field imaging [37, 43].

3.2.5 Specific Absorption Rate (SAR)

Transmitted RF energy can be deposited in the body as heat. When the field strength is up to 1.5T, the wavelength of the RF is considerably long, resulting in only a small amount of energy absorption by the body. However, as the field strength moves towards higher fields, the RF frequency increases, as does the amount of RF power deposited in the body, and safety becomes a concern. Human body tissue can tolerate only a few watts per kilogram before its temperature begins to rise. According to Food and Drug Administration (FDA) safety guidelines, the specific absorption rates (SARs) for heads and bodies should be limited to 2W/kg and 8W/kg, respectively. Numerous factors affect the SAR value of a scan. The number and type of RF pulses in the pulse sequence, the type of coil, the position of the patient, and the static magnetic field strength are among the most pertinent factors affecting the calculated SAR. The more slices per TR, the higher the SAR. The more RF pulses per slice, the higher the SAR. A higher flip angle requires more energy and, thus, a higher SAR. The larger the volume of the transmitted coil, the higher the SAR. Therefore, body coils generally have higher SARs than do smaller volume, transmit/receive head coils. Patients positioned nearer the iso-centers and centered within the coils have lower SAR values than those positioned off-center, since the latter coil has a higher loading factor (i.e., less RF energy is reflected by the coil during transmission and energy is transferred into the patient more efficiently). Lower magnetic field strengths have lower SAR values than do higher field strengths [46, 47] because less energy is required by each RF pulse to accomplish the desired flip angle.

3.2.6 Susceptibility artifacts

Susceptibility artifacts result from variations in the local field gradients that occur near the interfaces of substances with differing magnetic susceptibilities. In other words, objects with magnetic susceptibility cause distortion and signal loss. An example of a large susceptibility artifact in the human brain is the region closed sinuses in T2* contrast images. At higher field strengths, the effects of susceptibility-induced geometric distortion and signal loss are even more aggravated, [5, 48, 49] since the strength and size of the local gradients are proportional to the field strength, B_0.

3.3 EXISTING METHODS OF REDUCING THE B_1 INHOMOGENEITY

As mentioned in the above section, this thesis will be addressed the B_1 inhomogeneity problem. To date, three major approaches have been developed to address this problem. They are improved RF coil designs [38, 50, 51], compensated RF pulse designs [52-55] , and post-processing image correction [56-64].

3.3.1 Improved RF coil designs

In high field or ultra-high field MRI, designing RF coils is particularly challenging since coils must be sufficiently large for practical use, but there is the constraint of high resonance frequency. At high frequencies, the wavelengths of high-frequency electromagnetic waves in the human body approach the RF coil's dimensions, and non-uniformity becomes an issue, as does

radiation loss [65]. These problems could result in the severe degradation of the coil quality factor (Q) and, ultimately, coil sensitivity. They could also limit the design of large-size RF volume coils with high-operating frequencies [65]. Several coil designs [38, 50, 65] have been proposed to solve these problems. Three examples are selected to discuss in this thesis.

The first example is Spiral volume coil. The spiral coil [50] uses angled conductors instead of straight axial conductors. The coil produces sinusoidal current distribution similar to a birdcage coil by preserving the discrete rotational symmetry around the axis. The difference between the traditional birdcage coil and the spiral coil is the variation of the current phase with distance along the axis. The rotation of the spiral coil conductors as a function of axial distance leads to a phase rotation of the RF field. The amount of phase rotation is determined by the tightness of the spiral. Experiments show that the spiral volume coil can improve spatial uniformity in images with a linear variation of phase along the axis.

The second example is the Detunable Transverse Electromagnetic (TEM) coil. Vaughan, et al. [38] introduces TEM coil for 4T MRI which exploits the uniformity of the body coil as a transmitter and utilizes the high SNR of the surface coil as a receiver. Both coils are detunable when operated. For a static magnetic field strength lower than 3T, this technique is generally used to acquire high resolution images [38]. However, at higher field strength, the design is much more challenging than it is at lower field strength due to signal loss. Studies of this coil design are promising for both functional MRI and spectroscopy images.

Microstrip transmission line (MTL) volume coil

The last example is Microstrip transmission line (MTL) volume coil [65]. The design is based on the concepts of using the miscrostrip transmission line (MTL), which consists of a thin strip conductor and a ground plane separated by a low-loss dielectric material, as a resonator.

With its semi-open transmission line structure, substantial electromagnetic energy can be stored in the area near the strip conductor. This reduces both the amount of radiation that is lost and the perturbation of sample loading to the RF coil at high fields. Compensation for B_1 inhomogeneity is made through adjustment of the depth of RF penetration which corresponds to the thickness to the dielectric material layer. Results of experiments conducted with human brains show improved SNR and slightly flatter images in MTL than in lower field images.

Although improving the RF coil performance is clearly a necessary step for homogeneous transmission and reception, it may be unlikely that coils alone will be able to remove all inhomogeneity because the effect also depends on the sample's geometry and its physical properties.

3.3.2 Compensated RF pulse design

This technique relies on shaping profiles, varying flip angles or adjusting the transmitting power of the RF pulse to compensate for the B_1 inhomogeneity inside the objects.

One of the best known compensated pulses used for B_1 inhomogeneity is adiabatic pulse. The adiabatic pulse [66] and slice-selective adiabatic pulse [67-69] are special RF pulses that can be used when the RF field is inhomogeneous. In general, the flip angles produced by conventional RF pulses use a constant, Larmor frequency and are sensitive to B_1 or RF field homogeneity. In contrast, those produced by adiabatic pulses are relatively insensitive to B_1 or RF field homogeneity. These special pulses are produced by sweeping the frequency of an irradiating RF pulse through the Larmor frequency. The disadvantages of adiabatic pulses are that they are difficult to produce and more time is required in order for the desired flip angle which causes

high SAR to be produced. Consequently, rapid multi-slice imaging of humans is not currently practical with adiabatic pulses [38].

Deichmann, et al. [53, 54] propose that impulse 1D and 2D pulses compensate for the B_1 inhomogeneity correction of T1-weighted images. In their study, compensated RF pulses were used with the magnetization-prepared rapid gradient-echo (MP-RAGE) sequence [70] and the centric phase encoding (PE) technique [71]. When the gradients are applied during the excitation, the compensated pulse profiles have a parabolic shape which corresponds to the maximum flip angles near the edge and the minimum flip angle at the center. In the centric PE, the central k-space lines, which determine the image intensity, are acquired first. Therefore, their contribution to the image is proportional to the flip angle, since only the transverse magnetization component contributes to the signal at t=0. The loss of signal in the periphery was compensated by using these pulses. For the 1D pulse method, the correction is only in the z direction, and the B_1 map can be calculated using the equation below

$$B_1 \approx 1 - 5.2.10^{-5}(z)^2 \tag{3.8}$$

where B_1 has arbitrary units in z direction. For 2D pulses, additional y direction was compensated beside the z direction. Thus, the pulses consist of 2 RF pulses simultaneously excited with the gradients Gz and Gy to provide an inhomogeneity correction in both directions. Impulse1D and 2D pulses have very short pulse widths (1.3 ms). However, they are not a slice-slab selective, and thus, they require a high sampling rate in the readout direction to avoid aliasing.

Clare, *et al.* [55] present a method of compensating for B_1 inhomogeneity that combines both correction during excitation and reception. The method is based on calibration of the B_1 distribution in a particular coil, calculation and application of appropriate transmitter power

levels for each slice and compensation for receiver gain in post-processing. This method works well if the effect of coil geometry is the primary source of B_1 inhomogeneity, but it is less successful if the problem is caused by the sample's dielectric or conductive properties. For fields higher than 3T or sequences that have a high number of spin echo pulses such as Fast Spin Echo, increasing the transmitted power may cause the SAR to exceed its limits.

3.3.3 Post-processing image correction

These techniques are based on the practice of correcting the intensity of problematic image pixels. Artifact pixels are replaced by reference pixels derived using a particular algorithm. In addition, filters are typically applied to smooth the images. A variety of methods have been used with some success. Guillemand and Brady [59] used an expectation-maximization algorithm to iteratively classify and correct the images based upon a set of initial probability estimates. Decarli, et al. [60] compared local and composite medians of specific tissue classes. Lee and Vannier [61] applied the fuzzy "c-means-clustering" algorithm to estimate bias in MR images. Koivula, et al. [62] employed the compensating function to small variations within homogenous areas through extensive averaging. Wang, et al. [63] matched histograms in order to correct variations in scanner sensitivity. Sled, et al. [64] developed an iterative deconvolution approach, which they combined with polynomial filtering to estimate the distribution of true tissue intensities. Zhou, et al. [72] used both low and high frequency components of an image's intensity variation to correct for RF inhomogeneity. The results of these methods are sensitive to original signals and could lead to the reduction of image contrast between two tissues after correction.

4.0 3D TAILORED RF FOR B1 INHOMOGENEITY COMPENSATION AT 3T

4.1 INTRODUCTION

4.1.1 Overview

The design of 3D TRF pulses for B_1 inhomogeneity compensation discussed in this chapter is based on the design of 3D slice-select TRF pulses for B_0 field inhomogeneity proposed by Stenger, *et al.* [31, 32]. With the small tip angle approximation [20], an RF pulse and the desired magnetization profile have a mutually Fourier relationship as in Equation (2.42) and Equation.(2.53). Thus, if the magnetization is known, an RF pulse can be estimated using the inverse Fourier transform of a magnetization profile described by Equation(2.53). This concept can be modified for building 3D TRF pulses which incorporate B_1 inhomogeneity compensation. The proposed method aims to reduce the B_1 inhomogeneity at 3T as well as, possibly, higher magnetic field strengths. The pulses use a 3D map of the B_1 inhomogeneity acquired *in-vivo* as pre-scan images and are implemented as slab-select pulses for 3D imaging. Compared to the 3D TRF slice-select pulses for susceptibility artifact reduction [31, 32], the slab-select 3D TRF implementation is more practical because it allows for relatively short pulse lengths. Furthermore, the spatial variation of the B_1 inhomogeneity is slow enough that only a low-resolution map is required, further reducing the length of the pulse. Imaging experiments using a

$NiCl_2$ doped phantom and a normal human brain in vivo at 3T are discussed in the following sections.

4.1.2 Theory

Ignoring relaxation and off-resonance, the MR signal derived from reciprocity law at time t for one pulse with small tip angles approximation, $\alpha(\mathbf{r})$ can be written as

$$s(t) \propto \int_V W(\mathbf{r})\rho(\mathbf{r})C(\mathbf{r})\alpha(\mathbf{r})e^{-i\gamma\int_0^t G_{acq}(s)ds\mathbf{r}}d\mathbf{r} \tag{4.1}$$

In the above equation, V is the volume of the coil, $\mathbf{G}_{acq}(s)$ represents the acquisition gradients, $W(\mathbf{r})$ is spatial weighting due to selective excitation, and $C(\mathbf{r})$ is the receive sensitivity. The spatial dependencies of $\alpha(\mathbf{r})$ and $C(\mathbf{r})$ reflect the effects of an inhomogeneous B_1 field. These dependencies are present in the reconstructed image $I(\mathbf{r})$ of the spin density $\rho(\mathbf{r})$:

$$I(\mathbf{r}) = \alpha(\mathbf{r})C(\mathbf{r})\rho(\mathbf{r}) \tag{4.2}$$

Although the exact form of each of the above equations is dependent upon the specific details of acquisition, hardware, and reconstruction, the equations are generally applicable to methods described here. The B_1 inhomogeneity artifacts in $I(\mathbf{r})$ can be reduced by designing 3D TRF pulses using the small tip angle approximation [20]. The small tip angle approximation equates the pulse waveform $P(t)$ to the Fourier transform of the desired slice profile $W(\mathbf{k}(t))$, weighted by the k-space velocity produced by the gradients $\mathbf{G}(t)$ that are applied during excitation:

$$P(t) \propto \Delta(\mathbf{k}(t))\left|\mathbf{G}(t)\right|W(\mathbf{k}(t)) \tag{4.3}$$

This equation is technically valid for tip angles less than 30^0, and it has been found to hold well for angles on the order of 90^0 [26]. In the above equation, $W(\mathbf{k}(t))$ is defined as

$$W(\mathbf{k}(t)) = \int W(\mathbf{r}) e^{i\mathbf{k}(t)\mathbf{r}} d\mathbf{r}, \text{ where } \mathbf{k}(t) = -\gamma \int_t^T \mathbf{G}(s) ds \tag{4.4}$$

The excitation *k*-space trajectory $\mathbf{k}(t)$ is equal to the area remaining under the gradients at time t and at the end of pulse T. Any arbitrary $W(\mathbf{r})$ can be tailored provided that sampling requirements are met by $\mathbf{k}(t)$. However, one practical concern is that a pulse of unreasonable length often is needed to excite a profile $W(\mathbf{r})$ with the desired resolution and no aliasing. As a result, the implementation of the 3D TRF pulses often requires a multi-shot modality [32]. It can be seen from Equation (4.2) that B_1 inhomogeneity can be removed if the excitation profile is tailored to have the following spatial distribution:

$$W(\mathbf{r}) = \frac{W_0(\mathbf{r})}{C(\mathbf{r})\alpha(\mathbf{r})} \tag{4.5}$$

In this equation, $W_0(\mathbf{r})$ is the desired uniform 3D slice profile. Either *in vivo* measurements or theoretical calculations of $\alpha(\mathbf{r})$ and $C(\mathbf{r})$ can be used.

4.2 METHODS

The algorithm for building the 3D compensated TRF pulse encompasses three major steps: 1) building the uniform excitation 3D TRF pulses to excite the desired slice volume and acquiring a set of pre-scan images for generating 3D maps 2) generating 3D maps from the pre-scan images, and 3) building the 3D compensated TRF pulses from the 3D maps and acquiring images for the same slice location, FOV and slice thickness as the first step.

4.2.1 The uniform 3D TRF pulses construction

The 3D TRF pulses were designed for a General Electric (GE Medical Systems, Waukesha, WI) 3T imaging system with a standard head coil and a body gradient with a 150 T/m/sec slew rate and a 40 mT/m peak. A two-shot interleaved stacked-spiral *k*-space trajectory was used for the excitation. Each 2D trajectory spirally traverses from outside into the center, then blips along z at the center. Figure 4.1 shows a two-shot stacked-spiral trajectory in which the solid and dashed lines represent each shot. Exploiting the Fourier transform relationship which exists between the magnetization and the B_1, a uniform pulse profile or pulse envelope was built in the spatial domain. Construction of the pulse profile relied on several analytical functions, including a Fermi function along the in plane coordinate and the Fourier transform of the product of a sinc function with a Hamming filter along the through plane direction. Mathematical clarification is provided below.

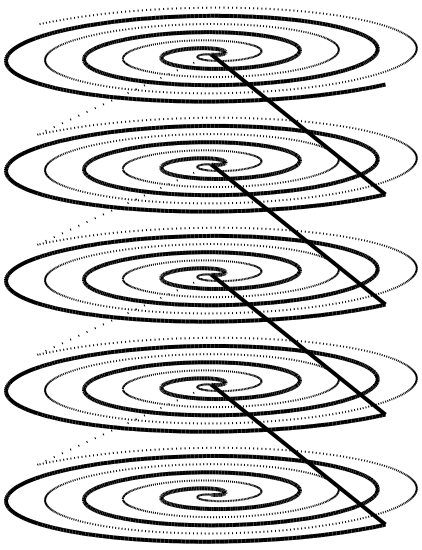

Figure 4.1 Diagram of the two-shot 3D stacked spiral k-space trajectory used for the 3D TRF pulses. The solid and dashed lines represent each shot.

The uniform slice profile $W_0(\mathbf{r})$ was the Fourier transform of a Hamming-filtered sinc function along z and a Fermi function along the in-plane coordinate ρ:

$$W_0(\mathbf{r}) = \frac{FT\left\{z_0 \mathrm{sinc}(k_z z_0) H(k_z)\right\}}{1 + \exp[(\rho - \rho_0)/w]}. \tag{4.6}$$

In this equation, z_0 and $2\rho_0$ are the effective slice thicknesses along z and ρ, respectively, while w is a parameter that controls the steepness of the edges of the Fermi function and $H(k_z)$ is a Hamming filter. The sample density $1/\Delta(\mathbf{k}(t))$ was determined in a manner consistent with that proposed by Hardy et al. [73]. Equation (4.6) shows a profile that is essentially a cylinder. The sinc function was smoothed with a Hamming filter to reduce the presence of a ripple along the z-direction. The slab thickness z_0 was 10 cm, and the in-plane radius ρ_0 was 12 cm. It is convenient to describe 3D TRF pulses in terms of "excitation resolution" and "excitation FOV" in the xyz-directions. These were 2.0x2.0x1.25 (xyz) cm^3 and 24x24x20 cm^3, respectively. The excitation resolution determines the degree to which small changes in the slice profile can be tailored, and the excitation FOV determines the separation between the slice aliases. The resultant pulse length was approximately 11 ms for each shot. Figure 4.2 shows Bloch equation simulations of the profile $W_0(\mathbf{r})$ plotted versus x-y and x-z using the 3D TRF pulse at a 20^0 flip angle. The 3D TRF pulses were inserted into a standard 3D stacked-spiral [33] pulse sequence for use on the scanner.

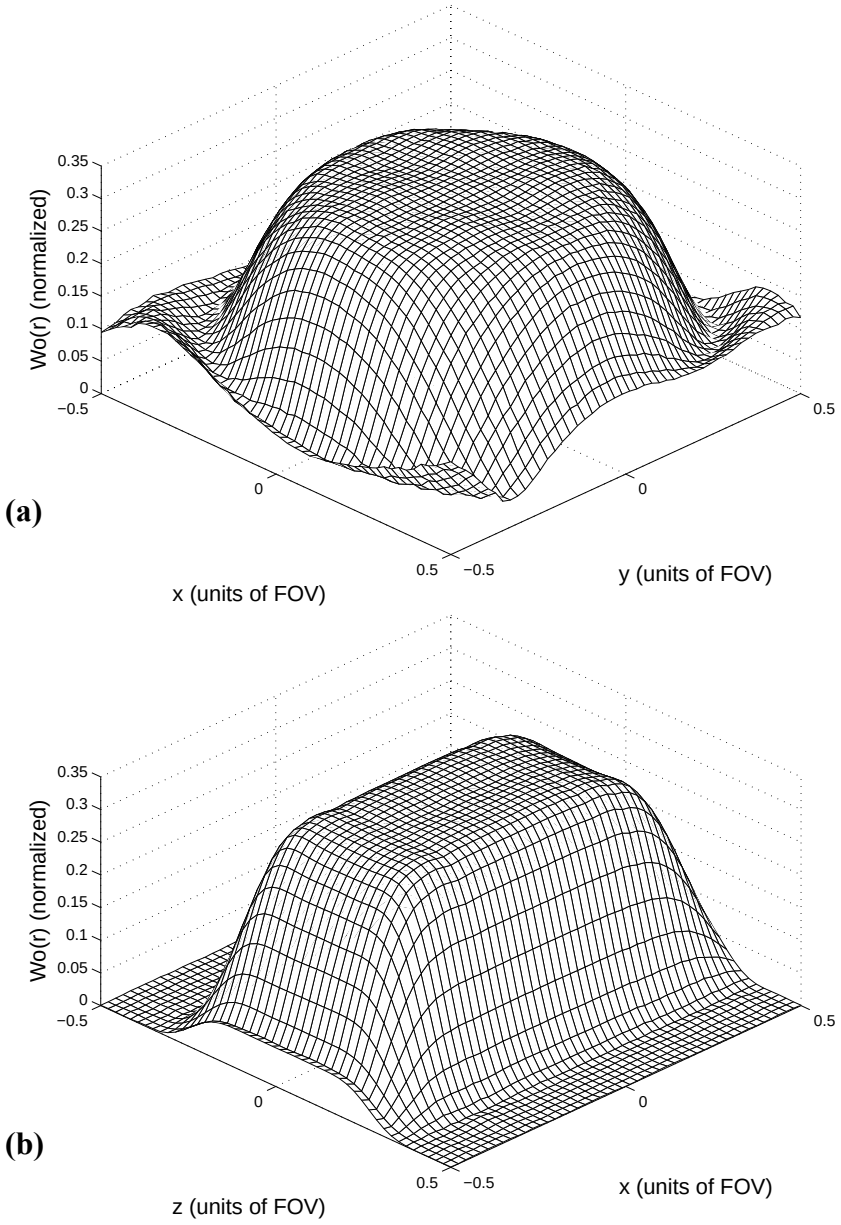

Figure 4.2 Mesh plots of the excited magnetization $W_0(\mathbf{r})$ in the (a) x-y and (b) x-z directions generated from Bloch equation simulations using 3D TRF pulse as input.

4.2.2 Generating 3D maps

Maps of the B_1 inhomogeneity were acquired as part of the pre-scan procedure using the uniform pulse profile for 3D TRF pulse excitation. The maps were generated from 3D images acquired

over the same FOV as the pulse and smoothed down to match the pulse resolution of 12x12x16 matrix size over a 24x24x20 cm^3 FOV. The optimal resolution of the maps was determined based on two parameters, pulse width and image details. The optimal resolution was the resolution such that the minor details of structure on the images were eliminated at the shortest pulse width. This implies that the spin density becomes uniform and leaves only the B_1 inhomogeneity as expressed in Equation(4.7). The effect of the smoothing process can be understood from Equation(4.2). When the resolution of $I(\mathbf{r})$ is reduced, the spin density becomes approximately uniform and the resultant image $\Delta M(\mathbf{r})$ is a map of the coil sensitivity multiplied by the flip angle:

$$\Delta M(\mathbf{r}) \alpha C(\mathbf{r}) \alpha(\mathbf{r}) \tag{4.7}$$

4.2.3 3D compensated TRF pulse construction

The excited slice profile was assumed to be uniform ($W(\mathbf{r}) = W_0(\mathbf{r})$). The 3D image was smoothed using a Gaussian filter with the full width at half maximum matched to the excitation resolution of the pulse. Equations(4.3), (4.5), and (4.6) were then used to determine the compensated 3D TRF pulse profile. However, the division required by Equation (4.5) produced singularities and errors which were amplified by noise in the measurement of $W(\mathbf{r})$. Therefore, it was determined that a simple proof of concept would be more convenient if the mean of $M(\mathbf{r})$ was either windowed or subtracted out such that

$$M(\mathbf{r}) = \bar{M} + \Delta M(\mathbf{r}) \tag{4.8}$$

In this case, the desired profile was determined by

$$W(\mathbf{r}) = \frac{W_0(\mathbf{r})}{\bar{M} + \Delta M(\mathbf{r})} \cong W_0(\mathbf{r})\left(\bar{M} - \Delta M(\mathbf{r})\right) \tag{4.9}$$

The approximation in Equation (4.9) holds true if $\Delta M(\mathbf{r})$ is small compared to $\overline{M}$. Figure 4.3 (a) shows an example of a 3D image of a 20 cm $NiCl_2$ phantom displayed as slices. The images were excited by the 3D TRF pulse with the uniform profile, and B_1 maps were subsequently generated. Figure 4.3 (b) shows $\Delta M(\mathbf{r})$ generated from (a) when the resolution was reduced to the optimal resolution such that the spin density became uniform. Figure 4.3 (c) shows the uniform profile $W_0(\mathbf{r})$ that was built from the analytical function in Equation(4.6), and (d) shows the compensated profile $W(\mathbf{r})$ that was obtained from Equation(4.9). Figure 4.3 (e) illustrates plots along the L-R direction through the center slices in (a) through (d). Figure 4.4 shows an example of one shot from a two-shot 3D TRF pulse with the B_1 inhomogeneity compensated profile ($W(\mathbf{r})$) as input. Rows (a) and (b) are real and imaginary parts of the pulse envelope function of the compensated 3D TRF pulse, respectively. Rows (c) and (d) are spiral gradient wave forms with two interleaves along x and y directions. Row (e) is the blip along z at the origin of each of the (c) and (d) spirals.

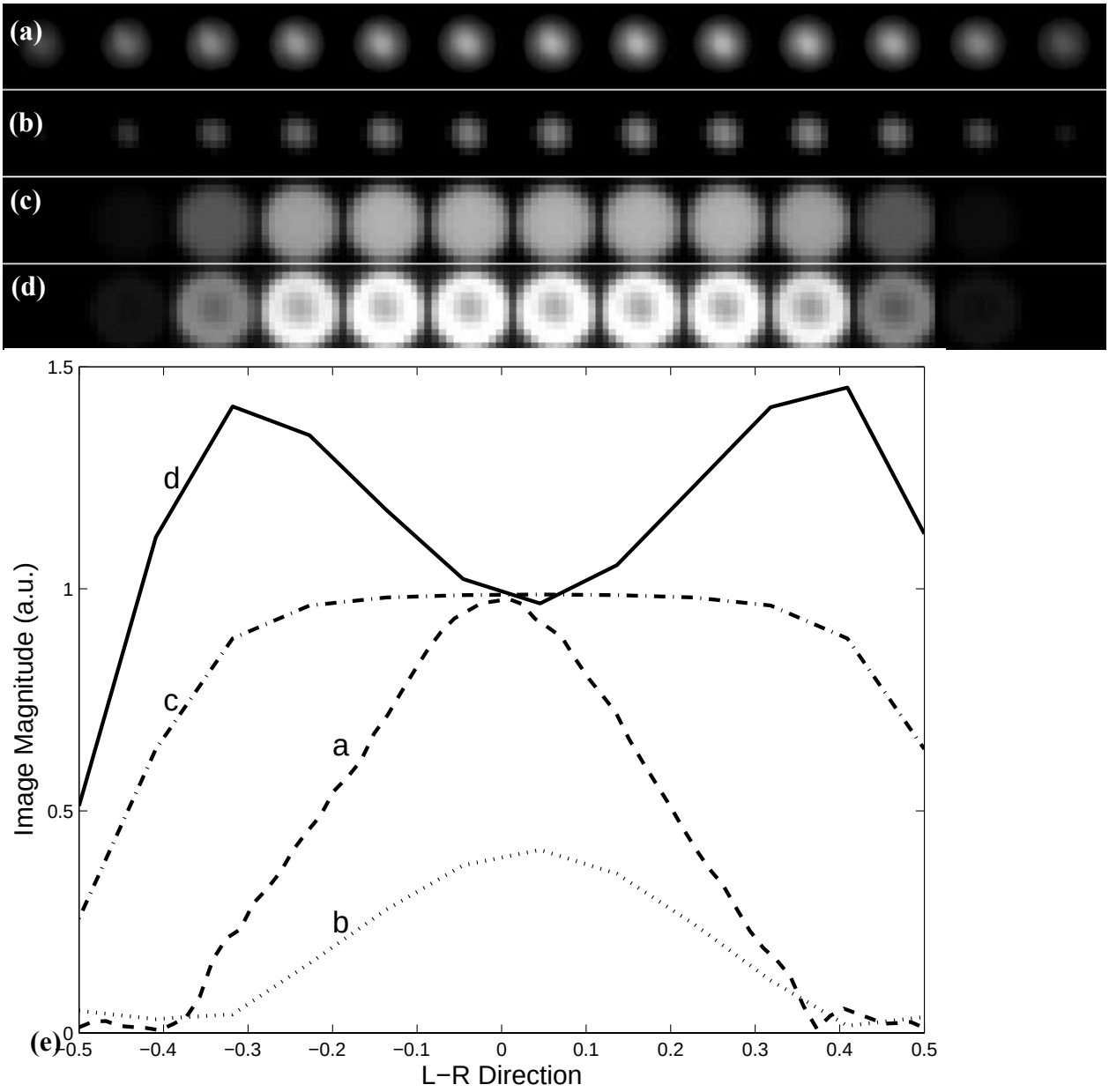

Figure 4.3 Three-dimensional images of a $NiCl_2$ phantom and example 3D TRF slice profiles. (a) initial images acquired for input into the pulse algorithm. (b) Same images smoothed with a 3D Gaussian filter and windowed between the mean and the maximum magnitude. These were used as the inhomogeneity maps $\Delta M(\mathbf{r})$. (c) Desired uniform slice profie $W_0(\mathbf{r})$. (d) Modified slice profile $W(\mathbf{r})$ that was generated from $\Delta M(\mathbf{r})$ and used to excited a uniform slice. The images (c) and (d) were windowed to the peak magnitude of (a) and (b), to half of this value. (e) Plots along L-R direction through the center slices of (a) through (d)

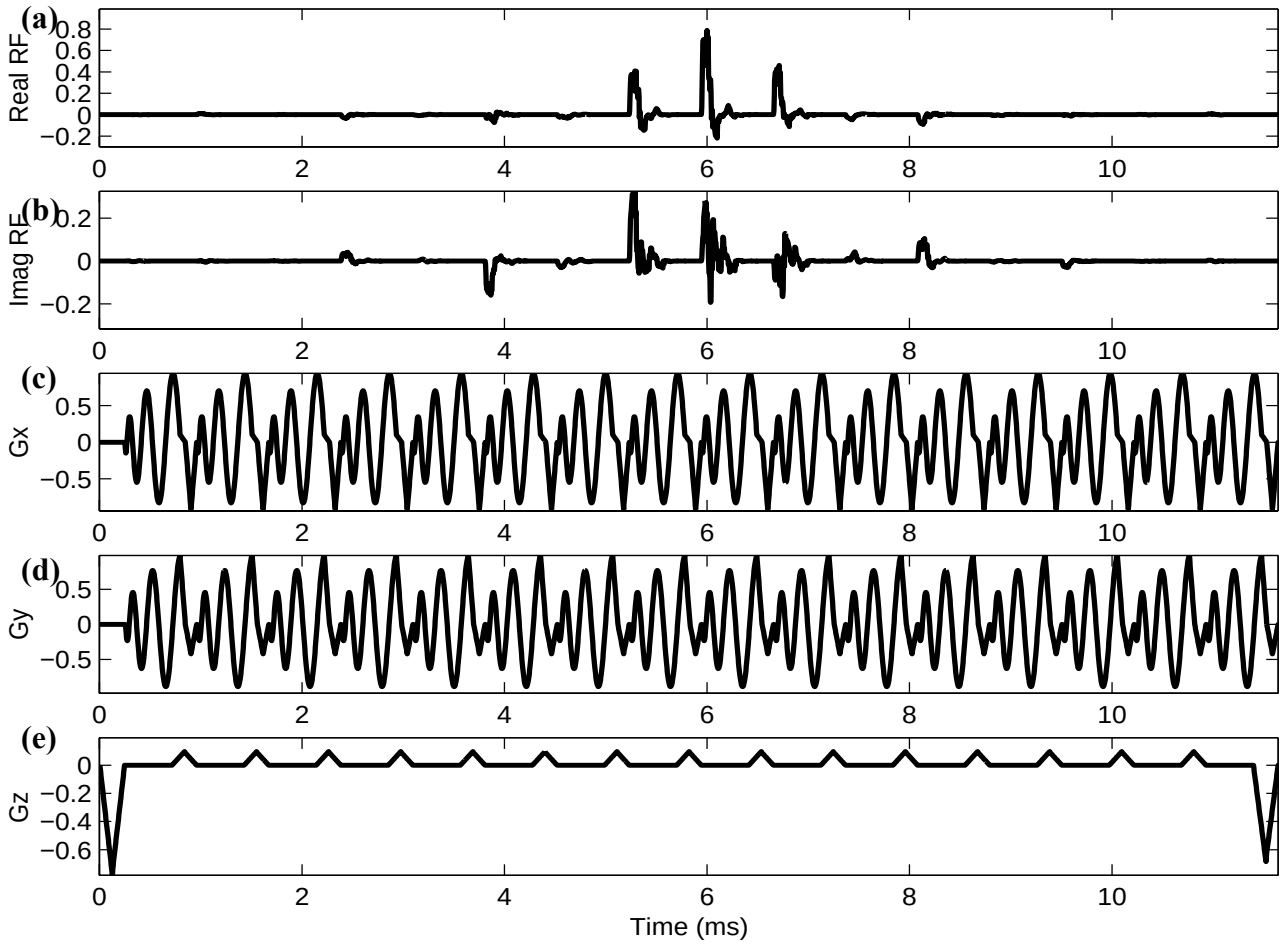

Figure 4.4 Diagram of one shot from a two-shot B1 inhomogeneity-compensating 3D TRF pulse. Rows (a) to (e) show, in order, the real and imaginary parts of the RF, followed by the x-,y-,and z-gradients.

Figure 4.5 shows Bloch equation simulations of the compensated profile $W(\mathbf{r})$ plotted versus *x*-*y* and *x*-*z* using the 3D TRF pulse at a 20^0 flip angle. Compared to Figure 4.2, these profiles excite the inverse of the spatial variation due to B_1 inhomogeneity. All of the image processing and pulse construction programs were written using Matlab, a software program produced by The Mathworks, Inc. and were run on the scanner console.

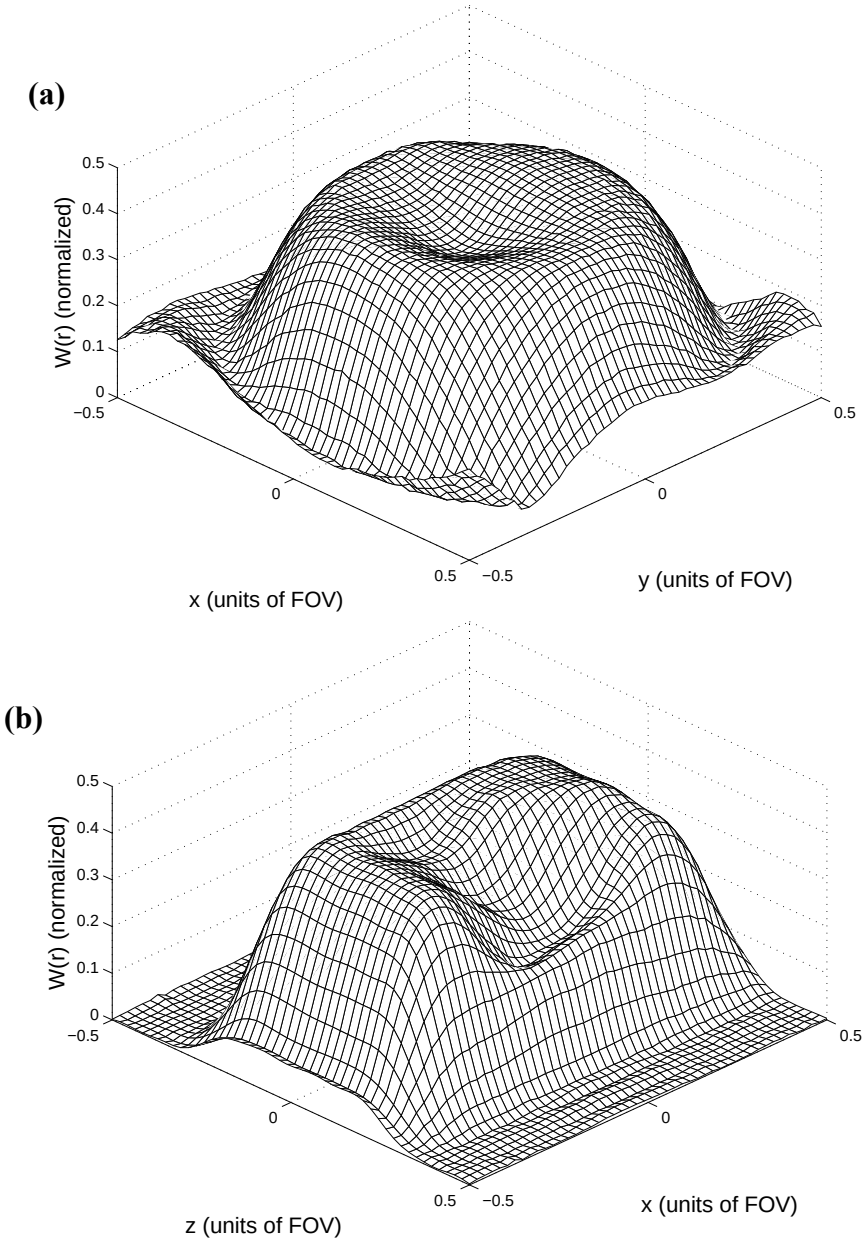

Figure 4.5 Mesh plots of the excited magnetization of $W(\mathrm{r})$ in the (a) x-y and (b) x-z directions generated from Bloch equation simulation using a 3D TRF pulse as input.

4.2.4 Imaging experiments

Phantom and human imaging experiments were performed to test the method *in vivo*. The 3D TRF pulse parameters and construction methods used were as described above, except for

variation in the flip angle. The phantom experiments used a 20 cm $NiCl_2$ doped TLT phantom in which a substantial amount of B_1 inhomogeneity was observed at 3T. The 3D stacked spiral acquisition had a 64x64x16 (*xyz*) matrix size, TR = 50 ms, TE = 8 ms, and FOV = 24 cm. Phantom images were acquired using a standard 10 cm (minimum phase SLR) slab-select pulse and a 3D TRF slab-select pulse with B_1 inhomogeneity compensation. A flip angle of 25^0 was used. The amplitude $P(t)$ of the 3D TRF pulses was adjusted manually during pre-scan to obtain the correct flip angle. Experiments were also performed on three normal human volunteers in different scan sessions. As in the phantom experiments, a standard slab-select pulse and a 3D TRF pulse with B_1 inhomogeneity compensation, both with a 25^0 flip angle, were used. The 3D stacked spiral acquisition had a 128x128x64 resolution using four spiral interleaves, TR = 50 ms, TE = 8 ms, and FOV = 24 cm.

4.3 RESULTS

Figure 4.6 (a) shows a 3D image of the $NiCl_2$ phantom displayed as a series of 2D slices acquired using the standard slab-select pulse. Note that the images show decreased magnitude near the outer edges due to inhomogeneity in the B_1 field. Figure 4.6 (b) shows images of the same phantom that were acquired after being excited by a 3D TRF pulse with B_1 inhomogeneity compensation. The resultant images have a more uniform magnitude. A 1 cm^3 ROI was taken near the edge of the phantom where a large degree of B_1 inhomogeneity was present. From the images excited by the 3D TRF and standard slab-select pulses, the SNR in the ROI was measured to be 88.4 and 55.6, respectively. Figure 4.6 (c) shows the difference between (a) and

(b). The images were first normalized to the maximum magnitude of (a), then they were windowed between 0.0 and 0.5.

Plots of the image magnitude profile through the center of the phantom along the L-R direction are shown in Figure. 4.7 (a). The solid and dashed lines are the profiles through the center of the phantom when the compensated 3D TRF pulse is and is not used, respectively. The profile when the compensated 3D TRF pulse was used is flatter, with recovered image magnitude near the edges. A plot of the difference between the solid and dashed lines in (a), normalized to the maximum of the image acquired without the compensated 3D TRF pulse, is shown in (b).

Figure 4.8 (a) shows a representative 3D image from one of the human subjects displayed as a series of 2D slices that were acquired using the standard slab-select pulse. The images are brighter in the center than they are at the edges due to the effect of B_1 inhomogeneity. Figure 4.8 (b) shows the same 3D image from the same subject acquired using the compensated 3D TRF slab-select pulse. The images show a more uniform image magnitude than those acquired with the standard slab-select pulse.

Figure 4.9 shows a 3D image from a human brain displayed as axial, sagittal, and coronal slices through the volume center. Rows (a) and (b) were windowed to the same minimum and maximum magnitudes. They were acquired with a standard 3D slice selective pulse (a) and the compensated 3D TRF pulse (b). Row (c) shows the difference between (a) and (b), normalized to the maximum magnitude of the image shown in (a), windowed between 0.0 and 0.30.

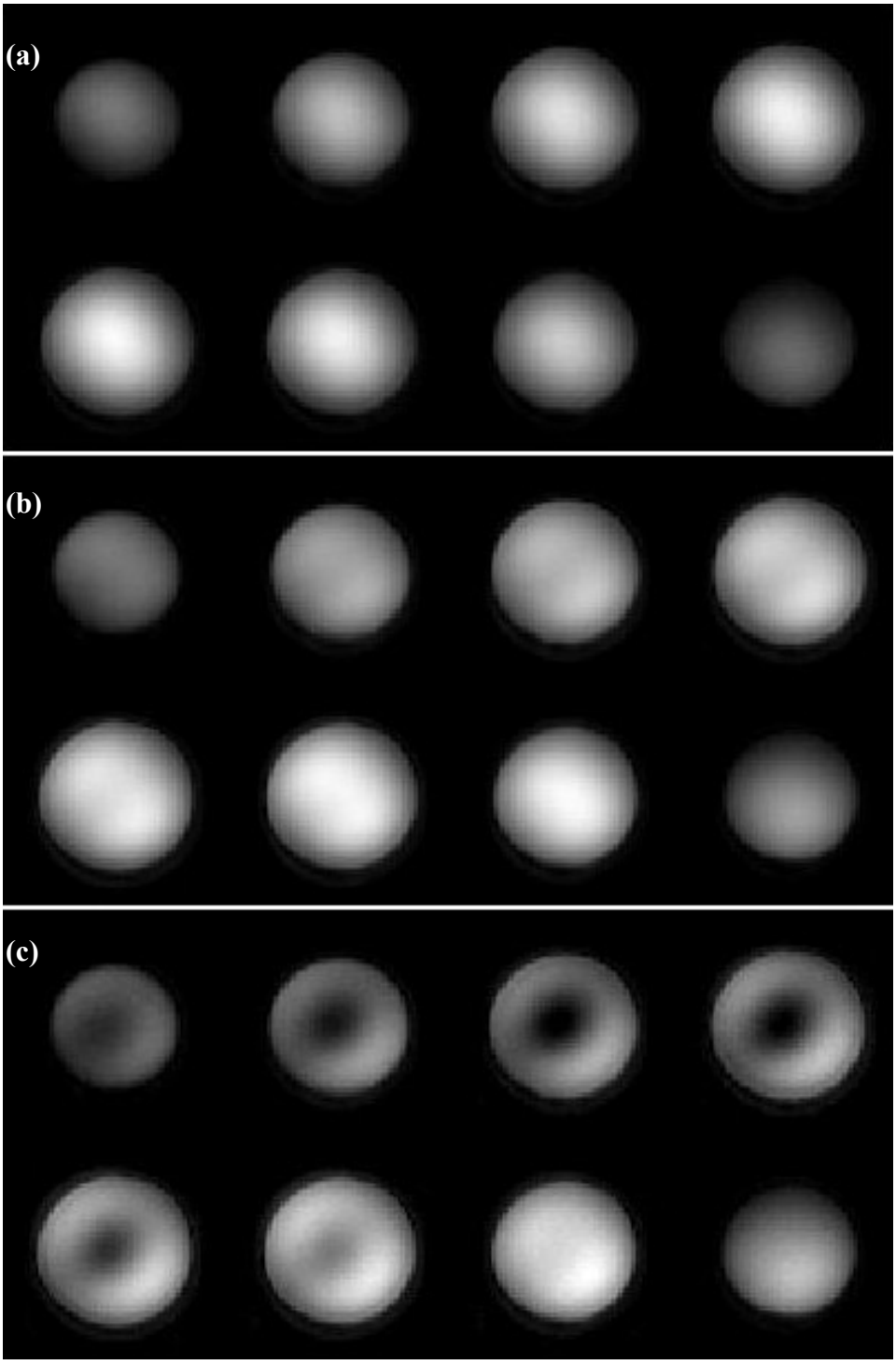

Figure 4.6 Three-dimensional images at 3T of a uniform $NiCl_2$ phantom displayed as slices (a) image excited with a standard slab-select pulse. (b) Images excited with the 3D TRF pulse. The images in (a) and (b) were windowed identically. (c) Images of the normalized difference between (a) and (b) (windowed between 0.0 and 0.5)

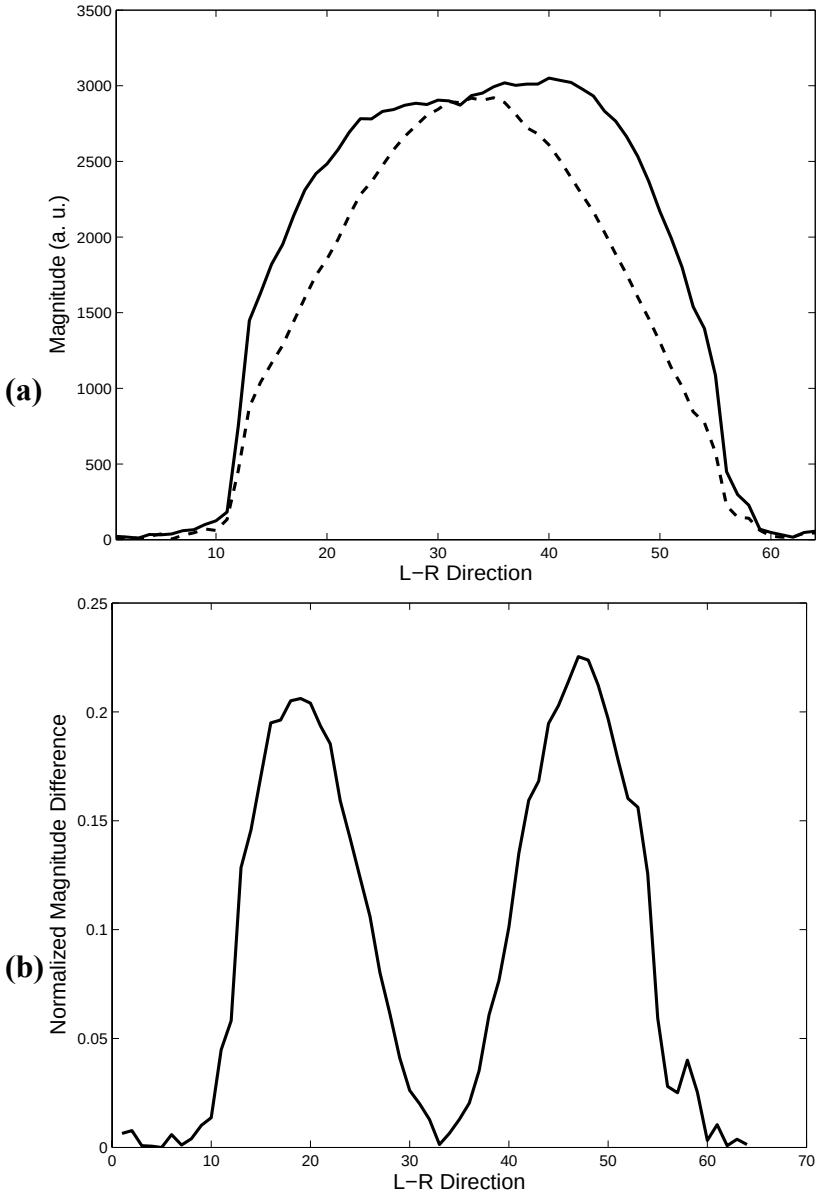

Figure 4.7 (a) Plot of the profile along the L-R direction through the middle of the volume. The dashed line is of with a uniform profile pulse and the solid line is of the pulse for B_1 inhomogeneity compensation. (b) Plot of the normalized difference between the profiles shown in (a).

(a)

(b)

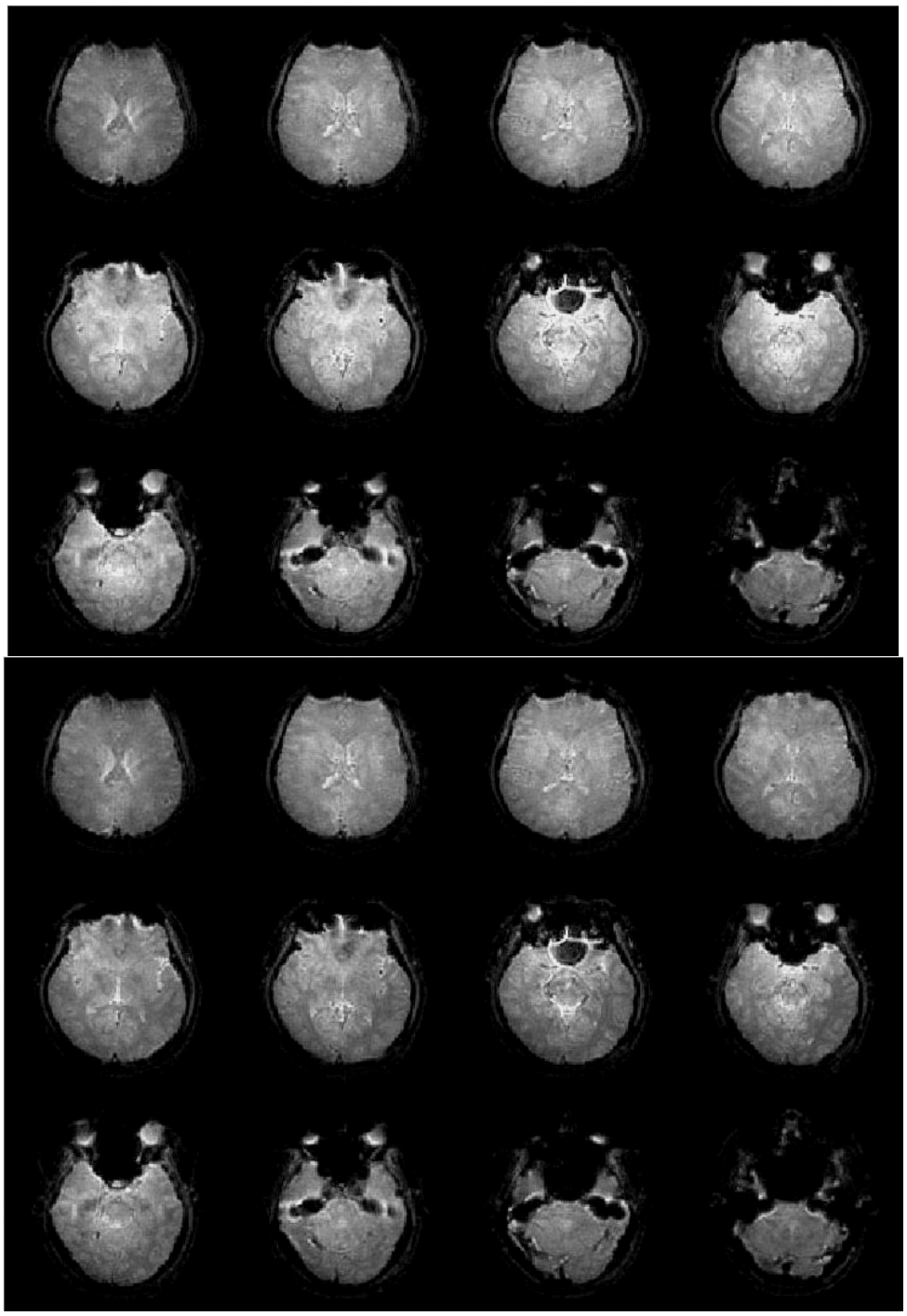

Figure 4.8 Three-dimensional images at 3T of a human brain in vivo displayed as slices. (a) Image excited with a standard slab-select pulse. (b) Image excited with a 3D TRF B_1 inhomogeneity compensated slab-select pulse. The image excited with the 3D TRF pulse shows a more uniform image magnitude between the edges and the center.

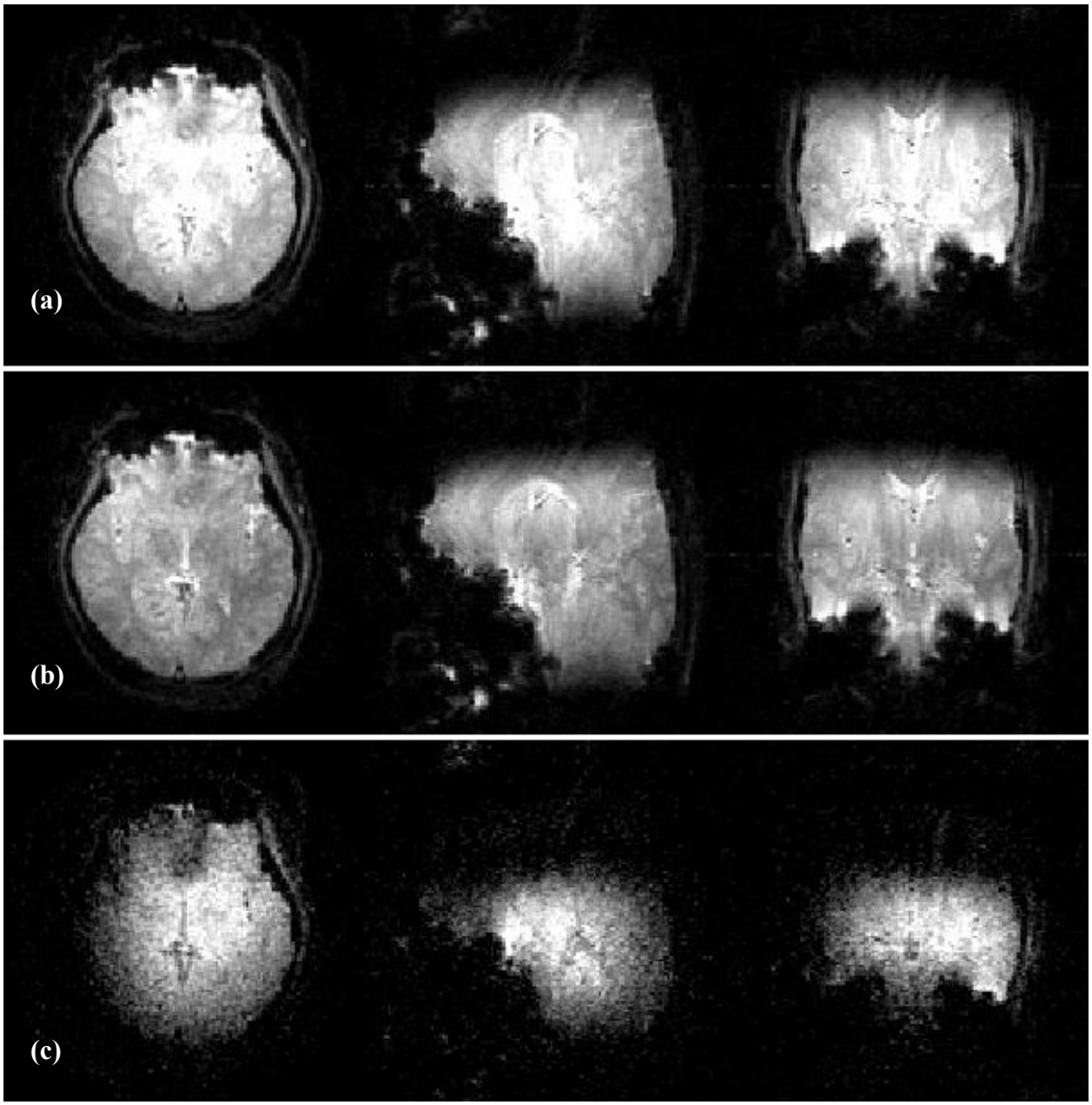

Figure 4.9 Center slices through a 3D image of a brain at 3T. The slice are displayed as axial(left), sagittal (middle)and coronal (right) 2D images. The images in row (a) and (b) were acquired with a standard slab-select pulse and a compensated 3D TRF pulse, respectively. They were windowed identically. (c) Images of the normalized difference between (a) and (b), windowed between 0.0 and 0.3.

4.4 DISCUSSION

This work shows that anatomically accurate maps of the flip angle and coil receive sensitivity can be used to construct small tip angle, slab-select 3D TRF pulses that compensate for B_1 inhomogeneity in all three spatial directions. The compensated 3D TRF pulses used in this research promisingly reduce B_1 inhomogeneity by approximately 30% of the peak image magnitude of the human brain over a 24x24x20 cm^3 FOV at 3T. This method was implemented on a standard scanner and required no special hardware. The flip angle and receive sensitivity maps were approximated using a smoothed low-resolution anatomical image. The smoothing removed differences in image intensity caused by anatomical features, leaving only the variation due to B_1 inhomogeneity. Although more precise measurements are desirable [74], the results seem to indicate that this process was adequate for 3T. In addition, this method has the added advantage of accounting for both the flip angle and received sensitivity variations. Compensating for the receive inhomogeneity with the RF is feasible for small tip angles. However, this leads to angles larger than optimal at different locations. This can cause the technique to break down, and it can create a spatial variation in tissue contrast. The results reported in this chapter indicate that the study methodology is adequate at 3T and has the added advantage that both the flip angle and receive sensitivity variations are present in the image and do not need to be acquired separately. A higher field implementation, however, may require the explicit measurement of the two maps, due to their potentially unique spatial distributions [75, 76] and larger flip angles. Equation (4.9) was employed where the fraction of inhomogeneity present in the image was subtracted to obtain the desired excitation profile instead of dividing. This approach was adequate for a proof of concept, but it required that the amplitude of the pulse be increased to match the peak image magnitude of the uncorrected image in order to maintain

SNR. This can be seen in the plot of Figure4.7 (a) where the center magnitudes of the phantom images were matched by increasing the amplitude of the 3D TRF pulse. Due to scanner time constraints, this was not done in the human experiments where the images acquired with the 3D TRF pulses were more uniform but had decreased SNR. This loss of SNR can be easily remedied by increasing the pulse amplitude, as was done with the phantoms. There are no known safety concerns using this method. The SAR is not to an issue with these pulses, despite their length, because the majority of the peak B_1 occurs only for short intervals at the spiral *k*-space centers along the length of the pulse. These sharp peaks in B_1 can be seen in Figure 4.4, rows (a) and (b). However, a potential problem is that the scanner may be unable to achieve the peak B_1 necessary for obtaining the desired flip angle in a region with very large inhomogeneity.

The major limitation of the 3D TRF method remains that pulse lengths are often impractically long due to sampling requirements. One possible approach to alleviating this problem is to decompose the pulses into multi-shot excitations. However, this approach causes increased image acquisition time. Still, when correcting the B_1 inhomogeneity in a 10 cm slab at 3T, the pulse sampling requirements are not as severe, due to B_1's slower spatial variations. It was found that a single shot pulse on the order of 22 ms which excited the slab with 2.0x2.0x1.25 cm^3 resolution over 24x24x20 cm^3 FOV was more than sufficient. Implementation in the stacked spiral acquisition required that the pulse be decomposed into two 11 ms long excitations in order to reduce off-resonance effects. In spite of the two-shot implementation, the acquisition obtained nearly whole brain coverage with a 2 mm^3 isotropic resolution in 51 seconds. Increasing the resolution to 1 mm^3 would bring the acquisition time to just less than 7 minutes, an approximate increase of eight times. A factor of two in acquisition speed could be obtained by developing a

single-shot implementation of the 3D TRF pulse. It is likely that an excitation with a lower map resolution would have worked adequately, requiring a 3D TRF pulse shorter than 22 ms. However, the chosen resolution was based on the sampling needs of the uniform slice profile function $M_0(\mathbf{r})$. Although using smoother functions for $M_0(\mathbf{r})$ would reduce the pulse length, the edges of the slice profile would be less steep. The slice profile along the slab-select direction of the 3D TRF pulse used in this work was already not as sharp as the minimum phase SLR slab-select pulse, and 25% over-sampling was required to remove aliasing. Poor slice profiles are a limitation of this technique.

4.5 CONCLUSIONS

This work presents a novel 3D tailored RF pulse method that uses anatomical maps of the flip angle and coil receive sensitivity to compensate for B_1 inhomogeneity in all three spatial directions. Compensated 3D TRF slab-select pulses were able to be designed that performed at 10 cm thickness and reduced B_1 inhomogeneity by as much as 30% of the peak image magnitude over a 24x24x20 cm^3 FOV at 3T. This method was implemented on a standard scanner and required no special hardware. A 10 cm thick slab with 2 mm^3 isotropic resolution could be acquired in under a minute using the pulse with a four-shot stacked spiral sequence.

5.0 EXPLORATION OF THE USE OF 3D TRF PULSE FOR B_1 INHOMOGENEITY COMPENSATION IN ULTRA-HIGH FIELD MRI

5.1 INTRODUCTION

The previous chapter discusses the promising potential of compensating for B_1 inhomogeneity by using 3D TRF slab-select pulses. This chapter addresses the feasibility of using this technique for ultra-high magnetic field strength. However, the problem of B_1 inhomogeneity at ultra-high field is complicated since the wavelength of the RF excitation further decreases as the field strength increases. Accordingly, the image intensity distribution acquired during ultra-high field imaging exhibits a significant amount of B_1 inhomogeneity [42, 43, 51, 76]. This effect is caused by the phenomenon known as field polarization [21, 76]. Under this condition, the phase of the RF field is a function of its position inside the sample. At ultra-high field, both components of the B_1 field, clockwise and counterclockwise rotating fields discussed in section 2.4.1.1, need to be considered during the RF field calculation [76]. The transmission field and the reception field need to be calculated separately [76]. To explore the possibility of using compensated 3D TRF pulses to reduce B_1 inhomogeneity, the pulses were first tested in a Bloch equation simulation and then with a doped phantom of large diameter which was constructed to simulate the wavelike effects at ultra-high field.

5.2 METHODS

5.2.1 Bloch equation simulation testing

Maps[3] of B_1 inhomogeneity at 8T in Figure 4.1 (a) were generated from a spherical phantom of 18.5 cm diameter filled with 0.125 M NaCl. The phantom was loaded into a 16-strut TEM resonator operating under linear excitation, and the maps were numerically simulated using the Finite Difference Time Domain method tuned to the frequency of 340 MHz (8T). Pulse profiles for B_1 inhomogeneity compensation were designed for sixteen-shot 3D TRF pulses to excite a 10 cm thick slice after the complex summation of all images acquired with each shot. Multiple shots were used to minimize pulse lengths. The flip angle was 30^0, and the gradients were assumed to be those of a commercial scanner: a peak gradient of 40 mT/m and a slew rate of 150T/m/sec. The sampling requirements of the pulses were such that a 24x24x20cm (xyz) FOV was excited with a 16x16x8 (xyz) resolution. The numerically simulated B_1 inhomogeneity was re-sampled to that of the pulse and used in Equation (4.9) for $W(\mathbf{r})$. The length of each shot was approximately 3.8 ms.

Figure 5.1 (b) shows the compensated maps for 3D TRF slab-select pulses. The Bloch equations were numerically integrated to determine the effectiveness of the pulse at replicating the desired slice profile shown Figure 5.1 (c). The compensated 3D TRF slab-select pulse of one shot of 16-shot pulses is shown in Figure 5.2.

[3] Provided by Dr. Petra Schmalbrock and Dr. Tamer Ibrahim of Ohio State University

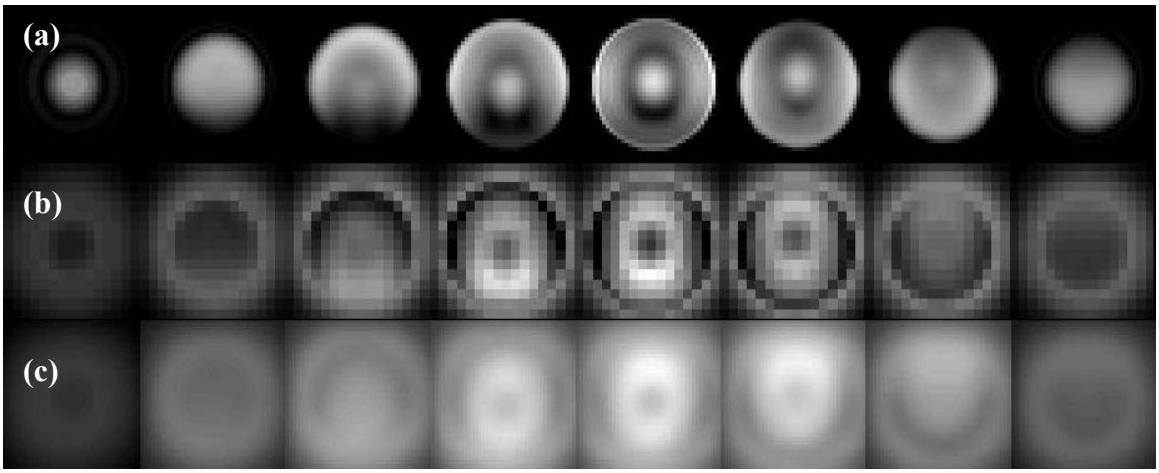

Figure 5.1 (a) Maps of the B1 inhomogeneity at 8T, (b) Maps for compensated 3D TRF pulses, (c) Maps of the compensated 3D TRF pulse profiles from Bloch equation simulation.

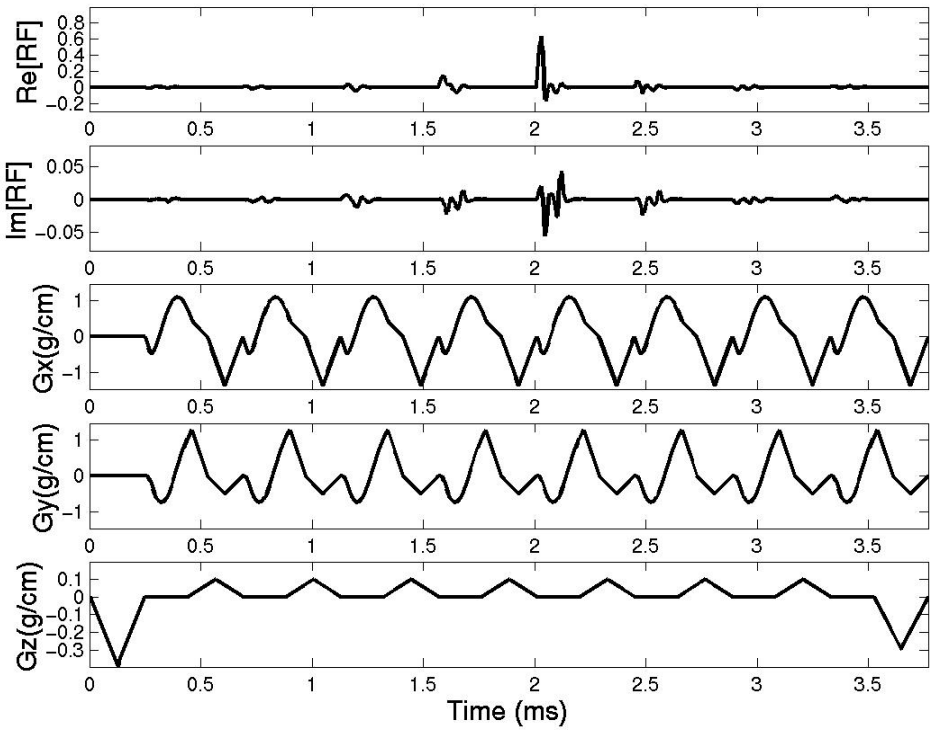

Figure 5.2 One shot of a sixteen shot 3D tailored RF pulse with a B_1 non-uniform compensation slice profile built into the 3D TRF slab-select pulses.

5.2.2 Imaging experiments

The pulse profiles shown in Figure 5.1 (c) from Bloch equation simulation demonstrate the possibility of using the 3D TRF pulses for B_1 inhomogeneity compensation. In this image, the region of decreased intensity near the center was compensated by the pulses. Then, the pulses were tested on the 3T MR scanner using a phantom that simulated the B_1 artifact at ultra-high field strength.

The imaging experiments were performed using a body coil as a source of B_1 excitation. The phantom that simulated a B_1 artifact at ultra-high field strength was a plastic sphere 36 cm in diameter filled with Manganese Chloride. It was found that the pulses generated using the same approach as discussed in chapter 3 failed in this experiment because the spatial content is high which violates the assumption made by Equation (4.9) that assumes the fraction of B_1 inhomogeneity is small. Thus, for the compensated B_1 maps, $W(\mathbf{r})$ needed to be based on Equation (4.5) instead. The background noise amplification and singularity problems were resolved by having a noise threshold set for each pixel of the maps. Specifically, any pixel in which the intensity was equal to or less than the threshold would remain unchanged; otherwise, the pixel would follow Equation(4.5). The compensated B_1 maps were designed for the following pulse parameters: the FOV was 40x40x40 cm, the slice thickness was 20 cm, the resolution was 4x4x2 cm (xyz), and the pulse 2-shot. The compensated 3D TRF pulse for a simulated B_1 artifact phantom at ultra-high field strength is shown in Figure 5.3 below.

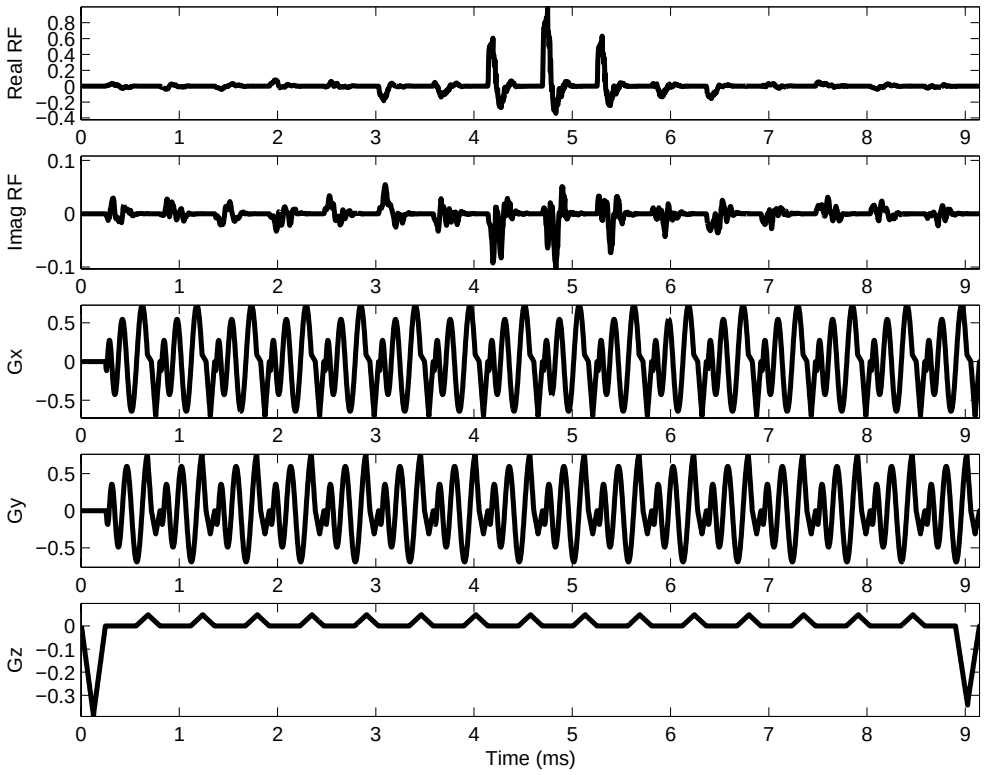

Figure 5.3 The compensated 3D TRF pulse for simulated B_1 inhomogeneity of ultra-high field at 3T MRI.

5.3 RESULTS

Figure 5.4 (a) shows the phantom images excited by a standard sinc pulse with gradient echo sequence that were acquired from the 3D spirals acquisition with resolution of 64x64x16 (xyz). For these images, the phase encoding was in z direction, the FOV was 40 cm, the slice thickness was 20 cm, TE=8 ms, TR=100ms, the flip angle was 20 degrees, and the slice thickness was 20 cm. All of the phantom images show an extremely bright spot located near the center. Figure 5.4 (b) shows the B_1 inhomogeneity maps acquired from a uniform slice profile, $W(\mathbf{r})=W_0(\mathbf{r})$ of

the 3D TRF pulses. Figure 5.4 (c) shows the resultant images from the same phantom excited by the compensated 3D TRF pulses. All images from Figure 5.4 were acquired with identical imaging parameters and pulse sequences. The images in Figure 5.4 (c) were taken after an application of the compensated 3D TRF pulse, and they show improvement in the B_1 uniformity. The edges of the images have greater intensity than images without compensation. However, the compensation near the center of the images is still insufficient. This experiment showed that there exist limitations in the current implementation of the method, and the causes of these limitations were explored. The relationships of intensities at different pixel locations and flip angles were compared between different scales of inhomogeneity. The scales of inhomogeneity inside phantoms represented by 3 different sizes of phantoms of diameter 10 cm, 20 cm, and 36 cm. The smallest phantom had a relatively uniform intensity throughout the volume. The inhomogeneity in the medium phantom was at 3T, and the largest phantom represented the effect of inhomogeneity at ultra-high field. All three phantoms were excited with identical standard sinc pulse, and their images were acquired at identical imaging acquisition parameters. The phantoms were excited with different flip angles, which varied from 0.05π to π in steps of 0.05π. The imaging acquisition parameters were slice thickness 5 mm, TE=6 ms, and TR=5 s. The magnitudes of the pixels located from the edge to the center of the phantoms for varying flip angles were plotted. Figures 5.5 (a), (b), and (c) show plot diagrams for the phantoms with diameters of 10, 20, and 36 cm, respectively. The dashed lines represent the pixels near the edge, and the solid lines represent the pixels near the center.

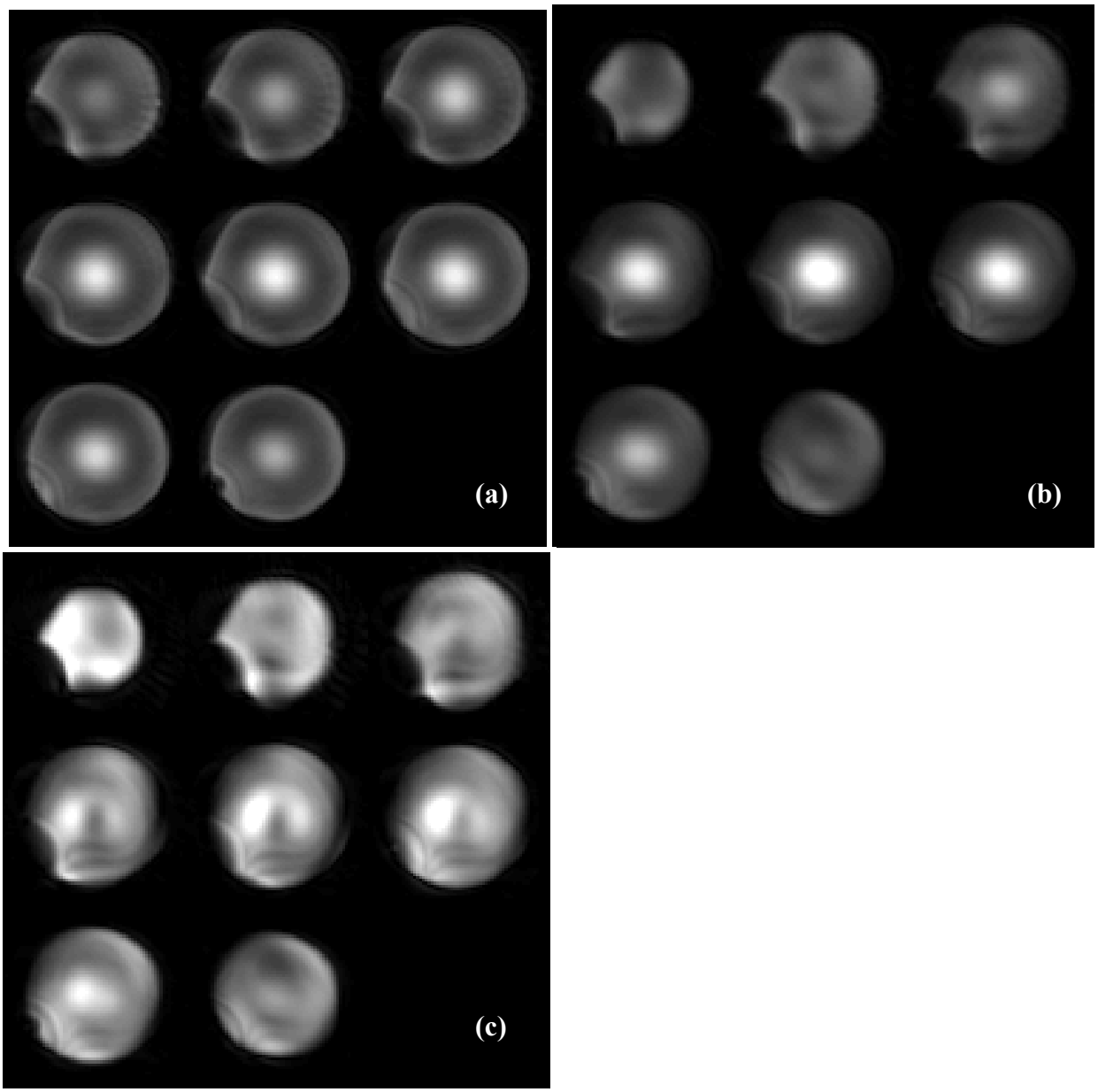

Figure 5.4 (a) Iages acquired from Manganese Chloride phantom using standard sinc pulse and 3D spiral sequence acquisition. (b) B_1 maps from two-shot 3D TRF pulses with a uniform slice profile. (c) Images from 3D TRF pulse with B1 inhomogeneity compensation.

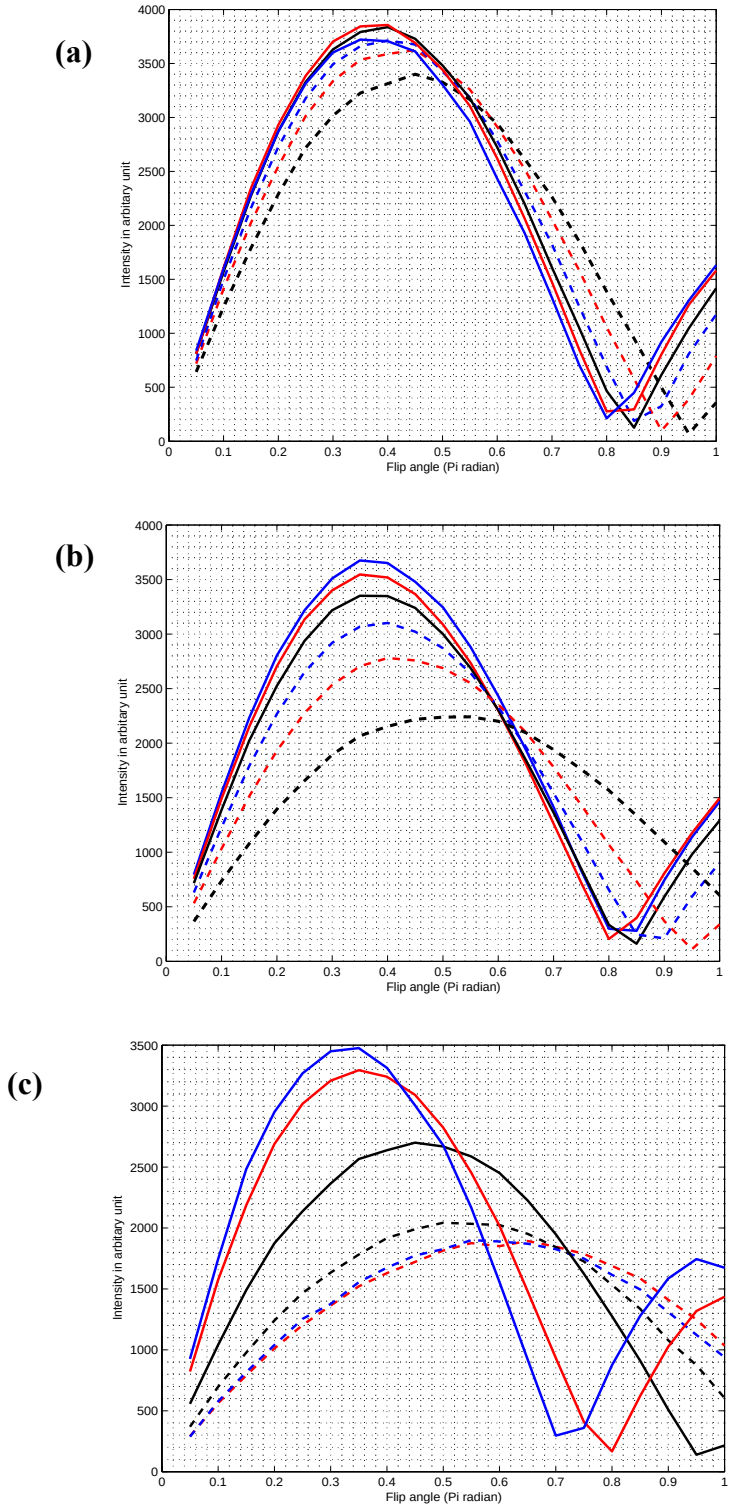

Figure 5.5 Plots of magnitudes of pixels located near the edges (dashed lines) and near the center (solid lines) versus flip angles for phantoms with diameters of (a) 10 cm, (b) 20 cm and (c) 30 cm

5.4 DISCUSSION

Figure 5.4 (c) shows phantom images after an application of the compensated 3D slab-select pulses. The images demonstrate insufficient power deposits in the loss signal area. An explanation of this problem was evident after experiments involving three different-sized phantoms. In the low flip angle regions (before reaching the peaks), the imaging intensity of phantoms with diameters of 10 and 20 cm show only minor differences in the magnitude of pixels located near the centers and those located near the edges. This implies that an increase in the flip angles of low flip-angle regions can compensate for the loss of signal near the edge due to a low level of B_1 inhomogeneity. However, the diagram of the imaging intensity from the phantom with a diameter of 36 cm, which represented inhomogeneity at ultra-high field, shows a significant difference in the magnitude of the pixels located near the edges and those located near the centers. In this situation, to compensate for the loss of signal near the edges, the flip angles must be greater than those allowed by the low flip angle approximation; the pixels which are close to the edge can never be compensated in this way. In addition, the loss of SNR after compensation is more severe in the larger phantom. To reduce inhomogeneity at ultra-high field strength by applying the low flip angle approximation, the limited peak B_1 may need to be addressed first. One possible cause for the limited peak B_1 is that the transmitter reaches the maximum allowance for the peak B_1. A new design of k-space trajectories to lower the peak B_1 which would result in allowing a larger flip angle for the 3D slice-select excitation may be necessary. Due to the polarization effect at ultra-high field, $C(\mathbf{r})$ and $\alpha(\mathbf{r})$from Equation [3.5] may need to be calculated separately, as done by Mihara, *et al*. [58] and Wang, *et al*. [77]. The

3D TRF pulses may need to be compensated only for transmission, and the reception field may compensate offline in the reconstruction routine. See Appendix C for more details.

5.5 CONCLUSIONS

The 3D TRF slab-select pulses may be employed for B_1 inhomogeneity compensation at 3T, and the compensated B_1 maps are simply calculated by subtracting the uniform slice profile from the inhomogeneity slice profile, as demonstrated in Equation(4.9). However, at ultra-high field strength, polarization exerts a dominant effect on the B_1 inhomogeneity and causes a substantial amount of non-uniformity in the B_1 field. The 3D TRF slab-select pulses provide some degree of compensation. The 3D TRF slab-select pulses have a very high peak in the middle lobe, which limits the pulse to only small flip angles. This problem may be resolved in any of the ways mentioned throughout this chapter, or it may require a combination of several approaches.

6.0 3D SLICE-SELECT TAILORED RF WITH FAST K_Z PULES FOR REDUCED B_1 INHOMOGENEITY AT 3T

6.1 INTRODUCTION

As discussed in earlier chapters, the limitations, the limitations of using 3D TRF slab-select pulses to compensate for B_1 inhomogeneity include limited peak B_1 and long pulse length. To overcome these limitations, this chapter will present a new pulse design associated with a new k-space. The 3D TRF slab-select pulses employ stacked spiral k-space as their trajectories to cover the slab volume in a one-shot pulse. Although the stacked spiral k-space is one of the fastest known trajectories through 3D k-space, it requires a significant number of sampling points, which results in a long pulse length. The new pulse design exploits results of the previous study which demonstrated that the B_1 inhomogeneity profile at 3T is likely a quadratic function. This is confirmed by many other studies, such as those conducted by Deichmann, et al. [53, 54] and Alecci [44]. The new pulse design does not require a B_1 map. Instead, appropriate analytical functions are employed as B_1 compensation profiles. These profiles are incorporated into the pulses. In addition, the k-space in the x-y direction is designed such that it is a quadratically compensated weighting function for the varying RF inhomogeneity. In the z direction, the k-space has a fast switching G_z with continuous gradients in a manner similar to EPI. Phase encoding is along the k_x-k_y direction. To ease the difficulties of pulse implementation, 2D separable pulse design was employed and each 2D pulse is weighted along the z direction by a

Gaussian function. The varying rate selective excitation (VERSE) was adopted to modify the middle lobe of the z gradients. VERSE has the greatest contribution to the pulse, allowing higher flip angles associated with higher energy deposits. Applying VERSE to the pulse also reduces SAR [78]. This pulse could be useful for cases in which thinner slices are desired (e.g., higher resolution images)

6.2 BASIC PRINCIPLES OF BUILDING THE 3D COMPENSATED FAST K_z PULSES

The general formulation of the 3D slice profile is:

$$sl(x, y, z) = w(x, y)w(z) \tag{6.1}$$

where

$w(x,y)$ is the desired in-plane excitation profile (x-y direction)

$w(z)$ is the desired slice profile (z direction)

$W(k_z)$ is the Fourier transform of $w(z)$

$W(k_x,k_y)$ is the Fourier transform of $w(x,y)$

The 3D TRF pulse will be derived from the 3D Fourier transformation of this function. The first step is to take the Fourier transformation in the z direction. This yields:

$$sl(x, y, k_z) = w(x, y)W\left(k_z\right) \tag{6.2}$$

To produce the final RF pulse, this function will be created based on the desired $W(k_z)$, the desired $w(x,y)$. Then the 2D Fourier transformation in the x-y domain is used and this function is sampled for each k_z plane along the excitation trajectory in k_x-k_y.

6.2.1 Fast Gz Switching

In this case, inhomogeneity is less important along k_z, but is more important along k_x-k_y. Therefore, the pulse design needs to be incorporated with inhomogeneity compensation in a manner similar to that described by Bornert, et al. [27, 28, 30]:

$$B_1(t) = \left|G_z(t)\right| \sum_{x,y} w(x,y) W\left(k_z\right) \exp\left(i2\pi\left(xk_x(t) + yk_y(t)\right)\right) \tag{6.3}$$

In order to assume of no phase change along the through plane, dwell time along k_z must be short. This can be achieved by traversing G_z first with a thin slice and phase encoding along the x-y direction. Thus, Equation (6.3) in the Fourier domain becomes

$$B_1(t) = \left|G_z(t)\right| \sum_{k_x,k_y} W(k_x,k_y) W\left(k_z\right) \tag{6.4}$$

Based on the work discussed in chapter 4 and earlier studies by Deichmann [53, 54], the B_1 inhomogeneity profile at 3T exhibits traits similar to a quadratic function in spatial domain. Therefore, it is possible to model the corresponding k space of a compensated slice selective pulse weighting function in the following manner.

6.2.2 Correction of quadratically varying RF inhomogeneity patterns

Consider that the five lines were traversed in the k_z direction and were positioned in (k_x,k_y) at:

1: position ($-k_0$,0), RF: $A_1\exp(-i\phi_0)$

2: position (0,$-k_0$), RF: $A_2\exp(-i\phi_0)$

3: position (k_0,0), RF: $A_1\exp(i\phi_0)$

4: position (0,k_0), RF: $A_2\exp(i\phi_0)$

5: position (0,0), RF: A_0

The k_z direction was weighted by a Gaussian function to yield the desired slice profile, and the k_x-k_y spatial frequency weighting was modeled by

$$\begin{aligned} W(k_x,k_y) = A_0\delta(k_x,k_y) + A_1 e^{i\phi_0}\delta(k_x-k_0,k_y) + A_1 e^{-i\phi_0}\delta(k_x+k_0,k_y) \\ + A_1 e^{i\phi_0}\delta(k_x,k_y-k_0) + A_1 e^{-i\phi_0}\delta(k_x,k_y-k_0) \end{aligned} \tag{6.5}$$

This produced a spatial weighting function

$$w(x,y) = A_0 + 2A_1\cos(2\pi k_0(x+x_0)) + 2A_1\cos(2\pi k_0(y+y_0)) \tag{6.6}$$

Here, $x_0 = y_0 = \phi_0/2\pi k_0$. If k_0 is sufficiently small (i.e., < 1/(2FOV)), then the cosine functions can be approximated using the first two terms in their power series expansion to yield

$$w(x,y) = (A_0 + 4A_1) - A_1(2\pi k_0)^2((x+x_0)^2 + (y+y_0)^2) \tag{6.7}$$

Here, $A_1(2\pi k_0)^2$ is the curvature of the profile, and (x_0, y_0) is the center of the RF bulge. At the edge of the FOV, the RF intensity varies by a fraction of $\varepsilon = \dfrac{-A_1(\pi k_0 FOV)^2}{(A_0 + 4A_1)}$. In order to reduce excitation in the center, A_1 can be made a negative value. With only five traverses of k-space, this pulse can be played in 3-5 ms, depending on the desired sharpness of the *z* profile and the slice thickness. Figure 6.1 shows the *k*-space trajectory of the pulse along k_x, k_y and k_z.

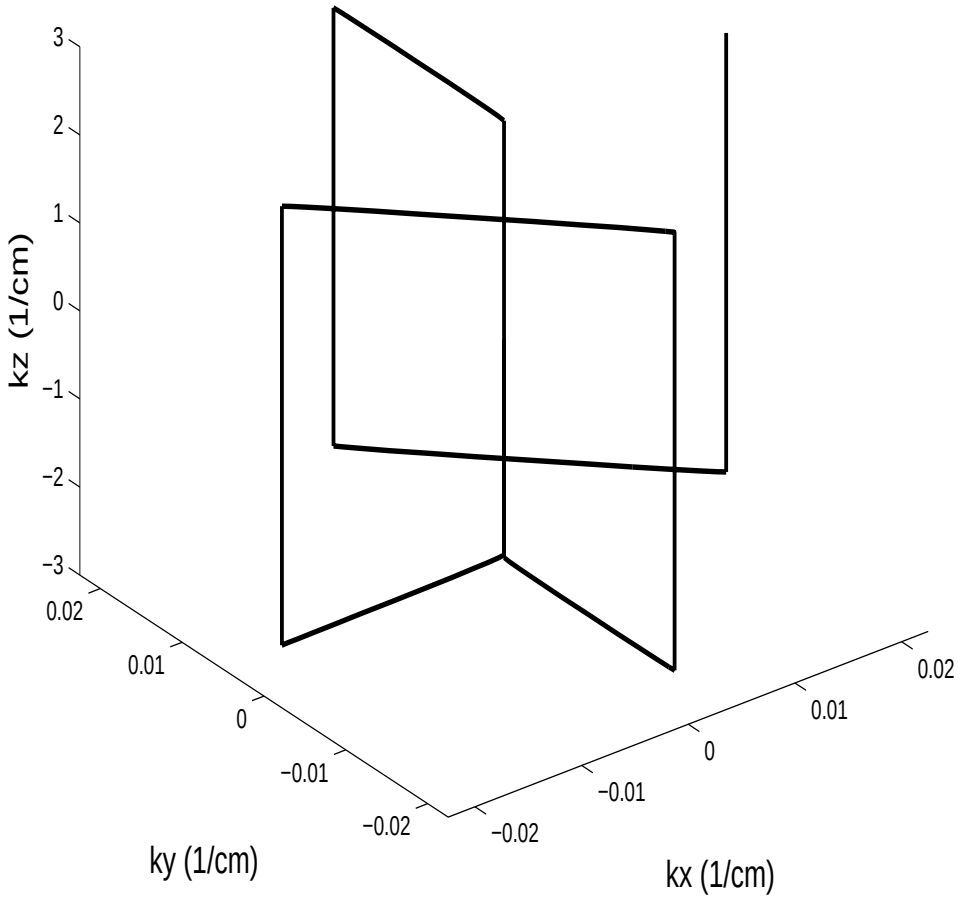

Figure 6.1 Diagram of the k-space trajectory for the fast-kz pulse design.

6.3 METHODS

6.3.1 Pulse Construction

The compensated fast-kz pulses were designed for a General Electric 3T system that was developed by GE Medical Systems. The system had a standard head coil, a 150 T/m/sec slew rate and a 40 mT/m peak body gradient. Essentially, the pulses were built from Equation(6.4). Gaussian function was chosen as a slice-select profile, $W(k_z)$ and its full width at half maximum (FWHM) characterizes the thickness of the slice. The in-plane excitation profiles, $W(k_x,k_y)$, were built from Equation(6.5). Equation(6.4) demonstrates that the pulses can be implemented separately, and the final pulse is the composite of the five sub-pulses. The z gradient waveform was determined by resolution along z axis, gradient slew rate, and peak gradient. It can either be triangular or trapezoid in shape, depending on the three parameters, and it was blipped along the x-y plane. The k_z traversed along five lines at five corresponding positions in (k_x, k_y), including (-0.5, 0), (0, -0.5), (0.5, 0), (0, 0.5), and (0, 0) in units of cm. Each of the five lines of k_z trajectories was then weighted using the $W(k_x,k_y)$ and $W(k_z)$. Although the resultant RF pulse function provides a relatively short duration pulse (e.g., 3.4 ms. for 2 mm of pulse resolution along z, 150 T/m/sec slew rate, and a 40 mT/m peak gradient), it is still impractical due to the peak B1 limitation on the RF amplifier. Thus, the pulses were re-fabricated using the variable rate selective excitation technique (VERSE) [78, 79] to allow more flexible magnitudes for the flip angles. This was achieved by slowing down the gradient slew rate and lowering the peak B1 at the central portion of the gradient. This modification has the expense of a longer pulse width. Figure 6.2 shows an example of the pulse. The pulse encompasses the real and imaginary parts

of the RF pulse along with the gradients, Gx, Gy, and Gz. The VERSE technique has been proven to cause no change to the selective excitation profile [78].

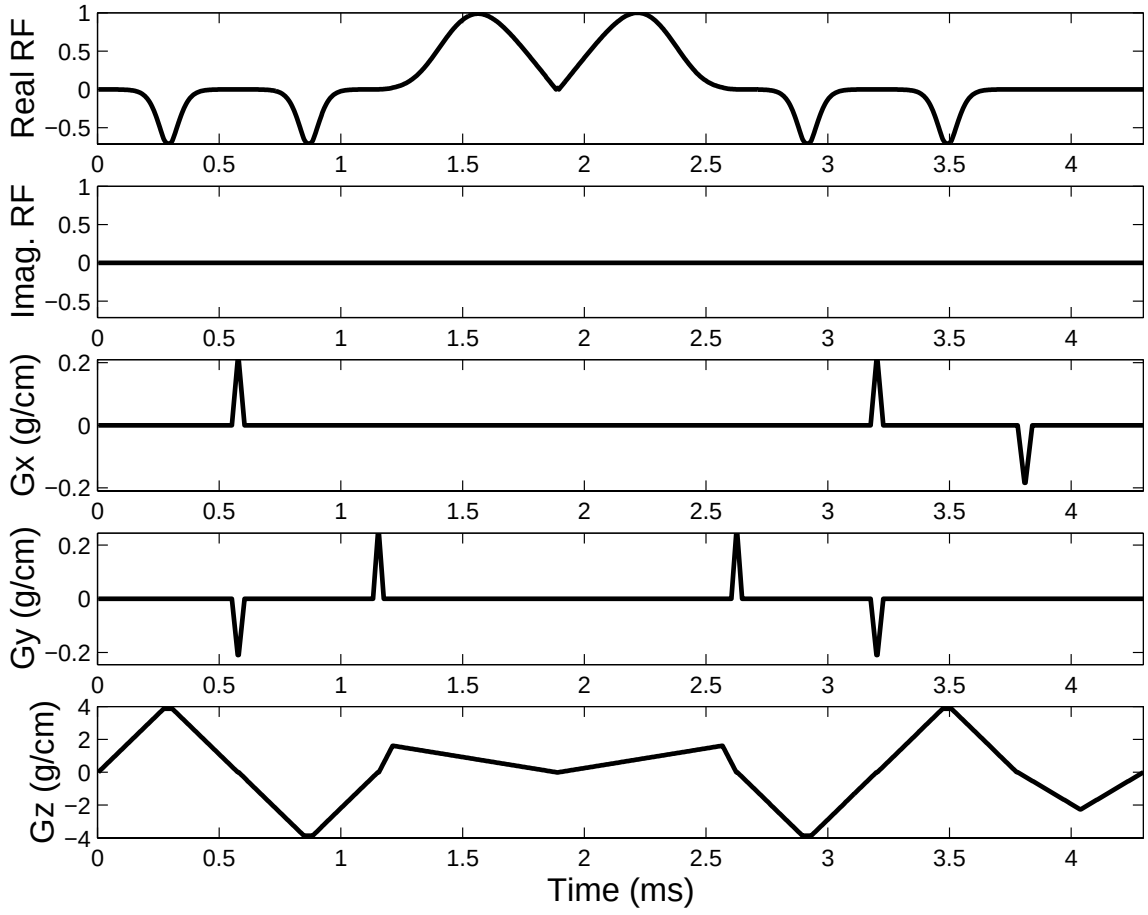

Figure 6.2 Fast k_z pulse. The rows (top to bottom) are the real and imaginary parts of the RF and the x-,y-, and z-gradients respectively.

The modified compensated fast-k_z pulse and the modified gradient waveform are compared to those of the original designs in Figures 6.3(a) and (b), respectively. As shown in Figure 6.3(a), the original design of the pulse in (dashed lines) has a peak amplitude that is approximately eightfold greater than that of the modified pulse with VERSE (solid line); however, the pulse width of the modified pulse is approximately 26 % longer than that the original design.

Therefore, it is clear that the specific absorption rate (SAR) is reduced, as shown in the equation stated by Connolly, et al. [78].

$$SAR \propto \int_{o}^{T} \left| B_1(t) \right|^2 dt \tag{6.8}$$

Equation (6.8) demonstrates that the magnitude of B_1(t) is quadratically proportional to the SAR, while the pulse width is linearly proportional. Therefore, reducing the magnitude by eightfold as the pulse width increases by approximately 26 % results in pulses still offer relatively lower SAR than those in the original design. As shown in Figure 6.3(b), the gradient waveform of the modified pulse was slowed down and dipped in the middle to provide the variable rate excitation. Equation (6.7) illustrates that A_1 determines the curvature of the profile (i.e., its spatial weighting function) and that the ratio of the signal intensity at the edge to the center of the profile is denoted by a fraction, ε. Since ε is a function of A_0 and A_1, the different curvature of the pulse profiles can be simply built by varying the amount of ε. Figure 6.4 shows examples of three different spatial weighting functions for the RF pulses from the Bloch equation simulation. These functions have ε =0.1, 0.5 and 1.0, respectively. Figure 6.5 shows an example of two interleaves spiral pulse sequences with the 3D compensated fast k_z pulse.

(a)

(b)

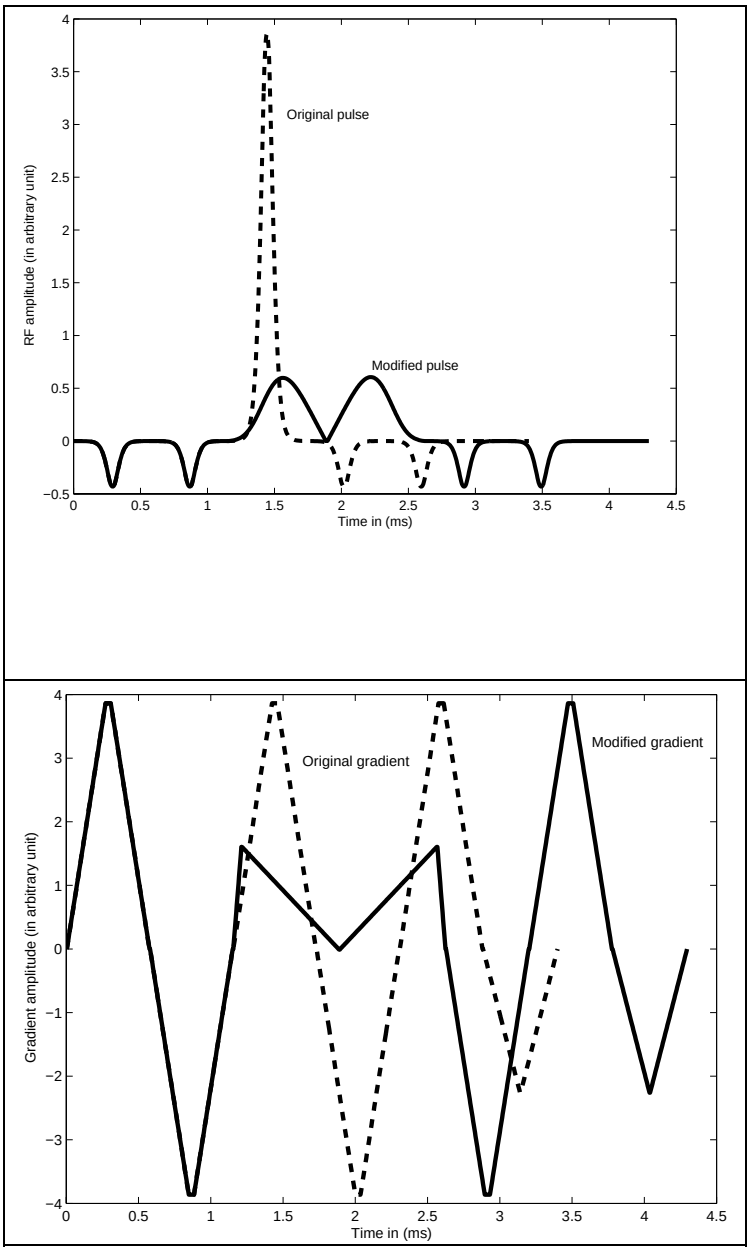

Figure 6.3 (a) Comparison of two RF pulse designs. The dashed line is the pulse from the original design. The solid line is the modified pulse using VERSE technique to decrease the peak amplitude. (b) Gradient waveforms of the original design (dashed line) and the modified gradient waveform (solid line) by VERSE.

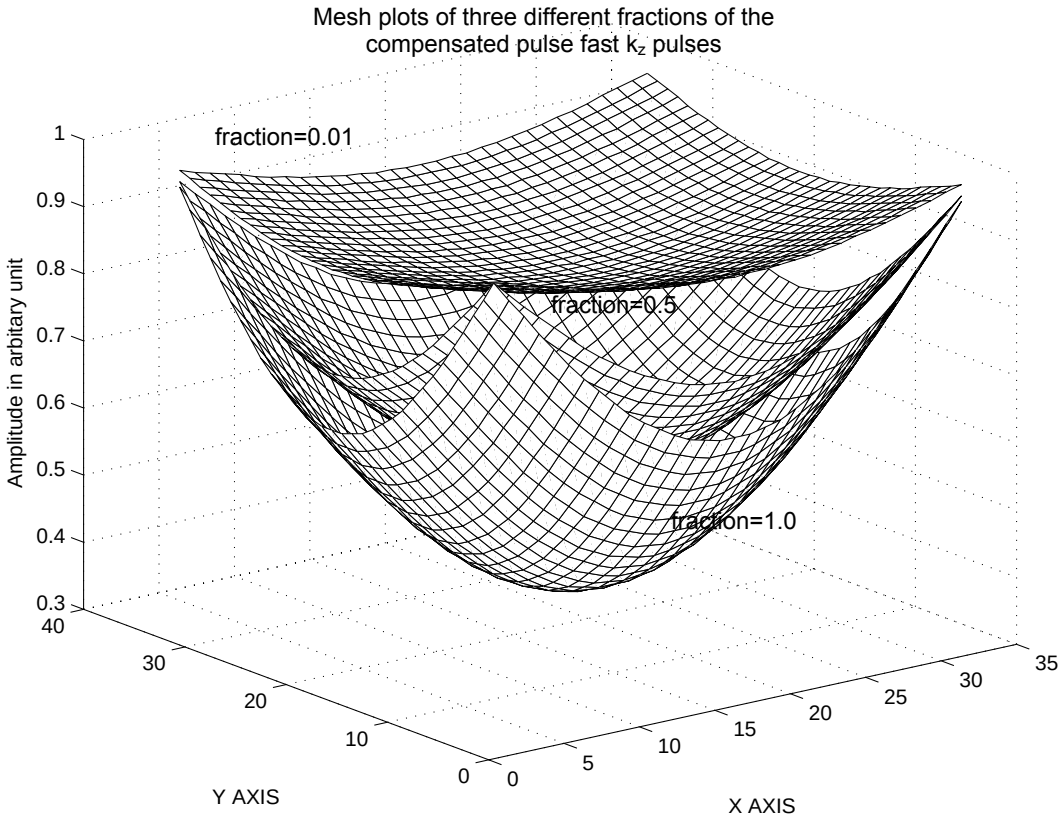

Figure 6.4 Slice profiles, $w(x,y)$ from Bloch equation simulation of three different spatial weighting functions (ε=0.1,0.5, and 1.0) pulses.

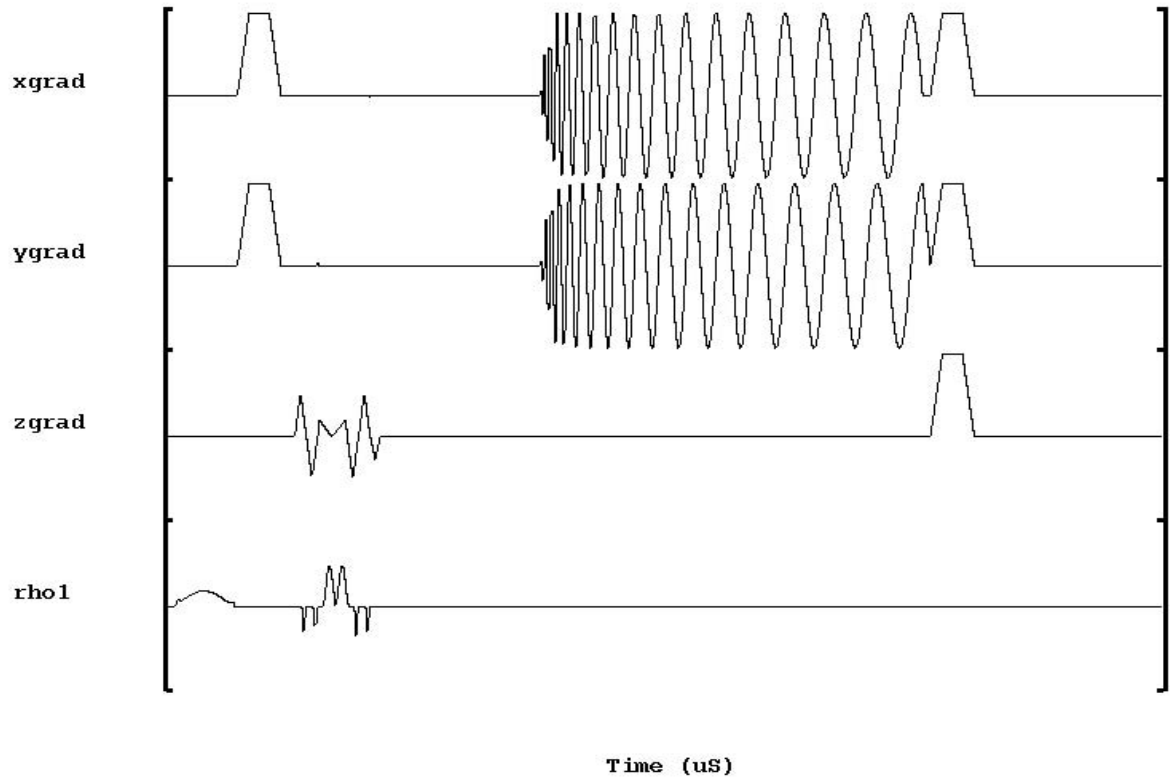

Figure 6.5 Time diagram of two interleaves spiral pulse sequence.

6.3.2 Flip angles calibration

The different slice profiles (e.g., sinc function and Gaussian function) may each provide a different amount of energy deposits to the pulses at the same flip angle. In order to more accurately compare images acquired from sinc pulse with those obtained from compensated fast k_z pulse, the same amount of energy deposit must be used. Thus, the flip angles acquired from the two pulses need to be calibrated. The calibration was performed with a $NiCl_2$ doped spherical phantom 20 cm in diameter. The phantom was excited with a sinc pulse at progressively increasing angles in steps of 5^o, from 5^o until the signal amplitude passed the peak amplitude. These procedures were repeated with the compensated fast k_z pulses. The flip angles

were plotted versus the image intensity, as shown in Appendix D. To calculate the flip angle of the compensated fast k_z pulse which would provide the same amount of energy deposit as the sinc pulse at 45^0, a search was made for the flip angle on the x axis of the plot of the compensated fast k_z pulse at the same image intensity of the sinc pulse at 45 ^{o}.

6.3.3 Imaging experiments

The imaging experiments began with Bloch equation simulation tests of the designed pulses at fractions (ε) which started at 0.5 and increased to 3.0 in steps of 0.5. The pulses which provided overcompensated profiles were eliminated for the phantom and human experiments. The protocol for the phantom experiments was used as a guideline for the human studies. The pulses with ε greater than 2.0 were found to result from overcompensation from the Bloch equation simulation, and they were not selected in phantom and human studies. For the phantom experiments, a $NiCl_2$ doped spherical phantom was excited by the four compensated fast k_z (ε =0.5, 1, 1.5, 2) pulses and one standard sinc pulse. The images obtained from the five pulses are shown in Appendix E. Pulse resolutions were 2 mm and 2 cm along z and x-y plane, respectively. Each pulse had one shot. The image acquisitions were 2D and had a 64x64 (*xy*) matrix size for 15 slices, a TR = 1 s, a TE = 3 ms, a thickness = 5 mm, a FOV= 20 cm, and a flip angle of 45^0. The experiments *in vivo* were done in three human subjects. Brain images were excited with a standard sinc pulse, as well as with the compensated fast k_z pulses with different fractions. The experiment on the first subject provided an opportunity to explore the optimal fraction of the compensated fast k_z pulses. The experiments with the other two subjects were used to verify the method. The first volunteer subject was scanned with the 3D compensated fast k_z pulses of fractions (ε) 0.5 to 2.0 in steps of 0.2, and with a standard sinc pulse. The optimal ε

was determined by both the quantitative approach and inspection. The quantitative evaluation relies on the measurements of SNR and the uniformity of the image profiles. The uniformity of the image profiles was determined by the differences between the image intensity at the edges, represented by areas 2 to 5 in Figure 6.6, and at the centers, represented by area 1, in percentage. The optimal fraction of the compensated fast k_z pulse was chosen from the pulses which offered the best compromise of high SNR and low percentage in difference between edge and center intensity. The ideal fraction is the fraction with the highest SNR and lowest percentage of the difference. All plots of the SNRs and the percentage of the differences used for the evaluation are in Appendix F. Since the quantitative measurements were calculated only for small, representative areas, a demand for greater accuracy required an inspection to be made as a conclusive step. Due to the fact that the B_1 inhomogeneity at 3T occurs at the center of the volume, only those slices 2 cm above and 2 cm below the center were compared. The calculated voxel size was 1.4x1.4x0.5 cm^3. Figure 6.6 demonstrates the five different locations used for SNR and uniformity measurements. Following the optimal fraction evaluation, two subjects were imaged both with the standard sinc pulse and with the compensated fast k_z pulse at the optimal fraction. The percentage of the signal differences between the edges and the center of the images was calculated, as were the SNRs. The SNRs and the percentage of the difference were compared between the standard sinc pulse and the optimal compensated fast kz pulse at five locations. The acquisition had a 256x256 resolution (24 interleaves spirals), a 45^0 flip angle, a TR = 1500 ms, a TE = 8 ms, and a FOV = 25 cm. The pulse construction programs were written in Matlab, a program developed by The Mathworks, Inc., and inserted into the spiral pulse sequence in order to be run on the scanner.

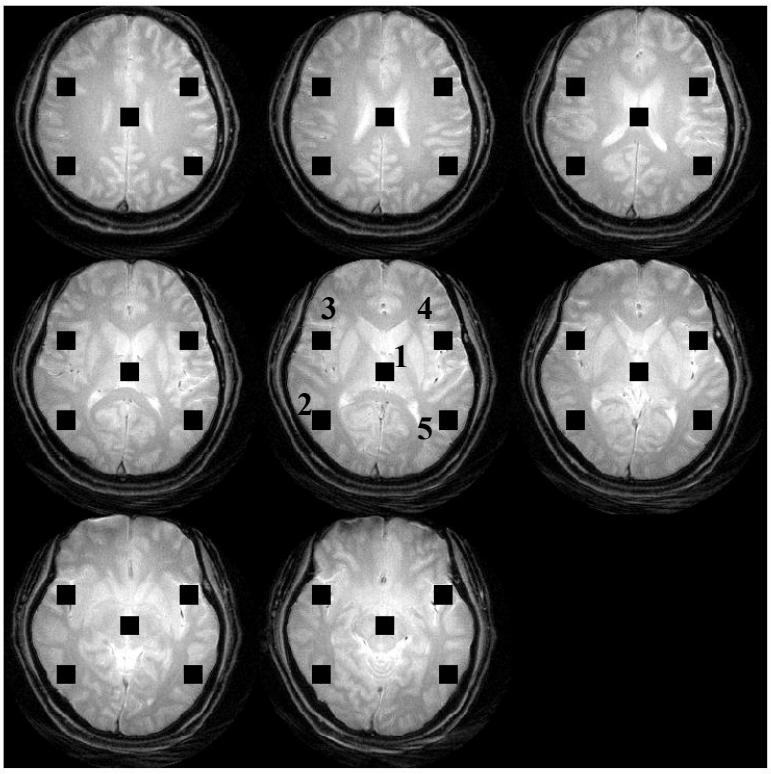

Figure 6.6 Five measured locations with sizes of 1.4x1.4x0.5 cm_3.

6.4 RESULTS

Figure 6.7(a) shows the phantom images excited using a standard sinc pulse and displays only selected slices near the center from top to bottom. The images excited by the standard sinc pulse have a higher magnitude at the center, due to the B_1 inhomogeneity. The compensated fast k_z pulse with ε of 1.5 promisingly compensates for the B_1 inhomogeneity at the slices near the center of the phantom by about 60 percent. Both Figures 6.7(a) and 6.7(b) were displayed at the

same window. Figure 6.7(c) shows the results of the images in row (b) subtracted from the results of the row (a) images, normalized by the maximum of row (b) then windowed from zero to approximately 80 percent of the maximum value. The images of slices near the center show improved signal intensity at their edges while the images of the slices located farther away from the center show improved B_1 imhomogeneity compensation of within 10 percent. These are not able to be observed in the same window.

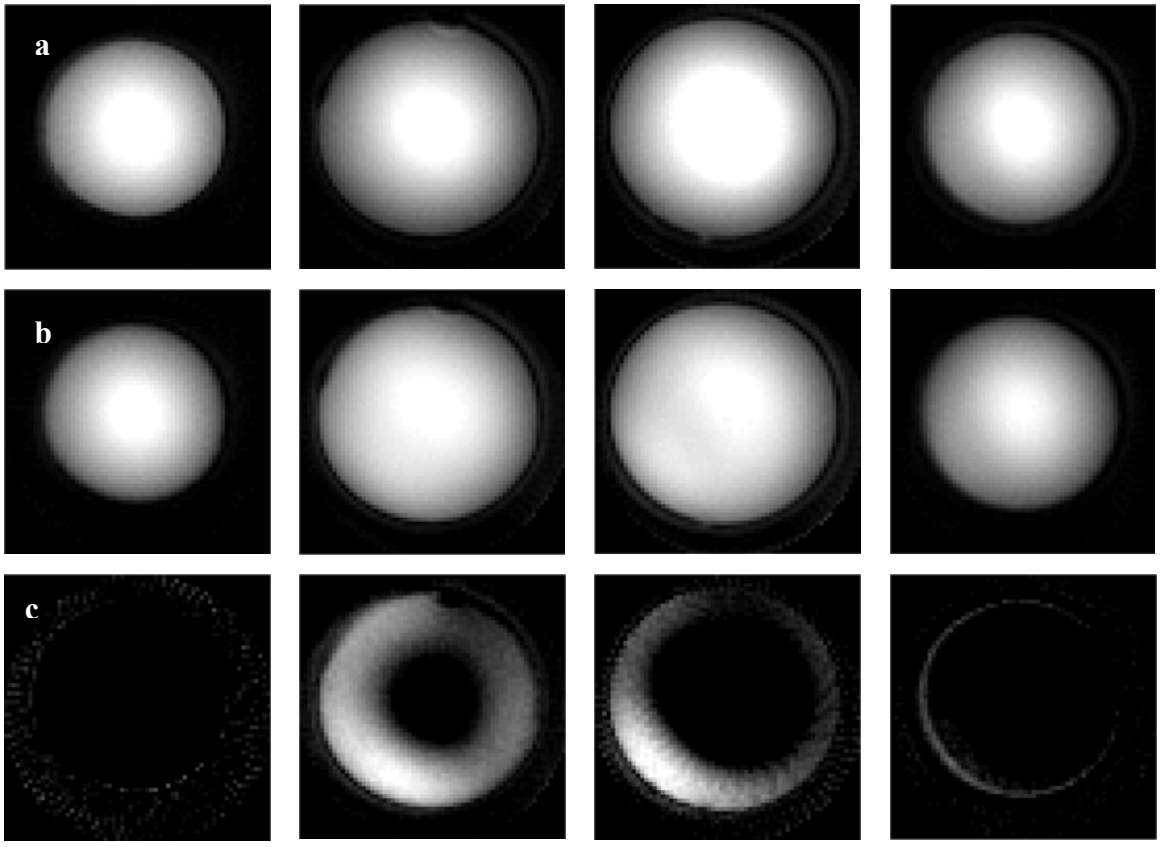

Figure 6.7 (a) Phantom images excited by a standard sinc pulse, (b) Phantom images excited by compensated fast-k_z pulse with a fraction of 1.5, (c) The difference between 6.7(b) and 6.7(a) windowed from zero to 80 % of the maximum value.

According to both the plots shown in Appendix F and to visual inspection of the images, the optimal fraction for brain images of the first volunteer was 1.0. Figure 6.8(a) shows images from a human brain excited with the standard sinc pulse. Images of slices near the center have decreased intensity at their outer edges. Figure 6.8(b) shows more uniform images excited with a compensated fast-k_z pulse at the fraction of 1.0. It was found that there was no significant variation of B_1 inhomogeneity for the three human volunteers. Figure 6.8(c) shows the difference between row (b) and row (a) calculated in of the same manner as was described for Figure 6.7(c). The images were windowed from zero to 80 % of the maximum value. The images show compensation at the outer edges of approximately 30 percent, depending on the slice's level of inhomogeneity. Figure 6.9 shows the plots of SNRs calculated from five locations of the images from Figure 6.8. One of these locations was in the center of the images, while the other four were at the edges. The solid lines were calculated based on images shown in Figure 6.8(a) that were excited by the standard sinc pulses. The dashed lines were calculated based on images shown in Figure 6.8(b) that were excited by the compensated fast k_z with a fraction of 1.0. Figure 6.9(a) illustrates that the compensated fast k_z pulses result in better SNRs of slice number 8 in all five locations than do those of the standard sinc pulses. However, for slices 9 through 12, the use of compensated fast k_z pulses improved the SNRs only in the peripheral areas, as shown in Figures 6.9 (b) through (e).

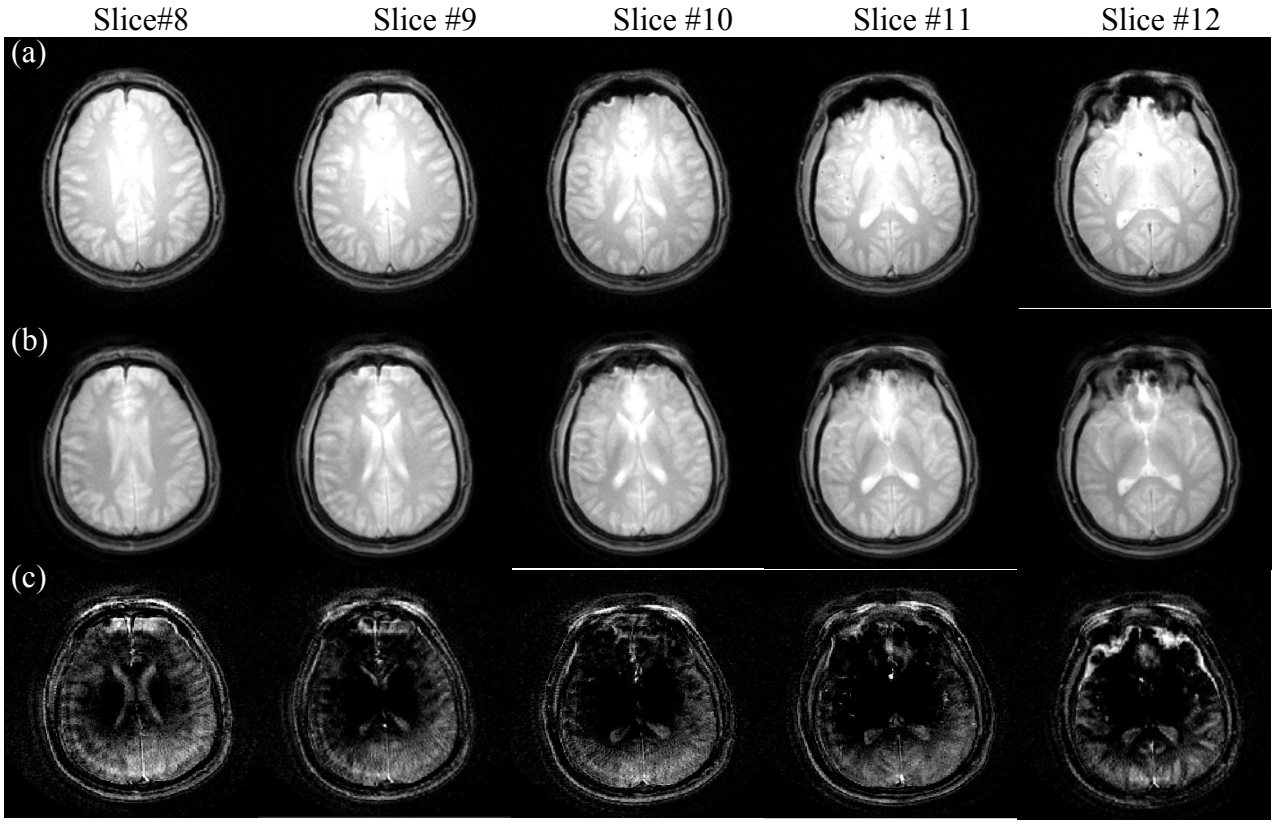

Figure 6.8 T2 weighted human brain imaged. (a) Images acquired from the standard sinc pulse, (b) Images acquired from the 3D compensated fast k_z pulse with a fraction of 1.0., (c) The difference between row (b) and row (a) normalized by the maximum intensity and windowed to approximately 80 % of the maximum value.

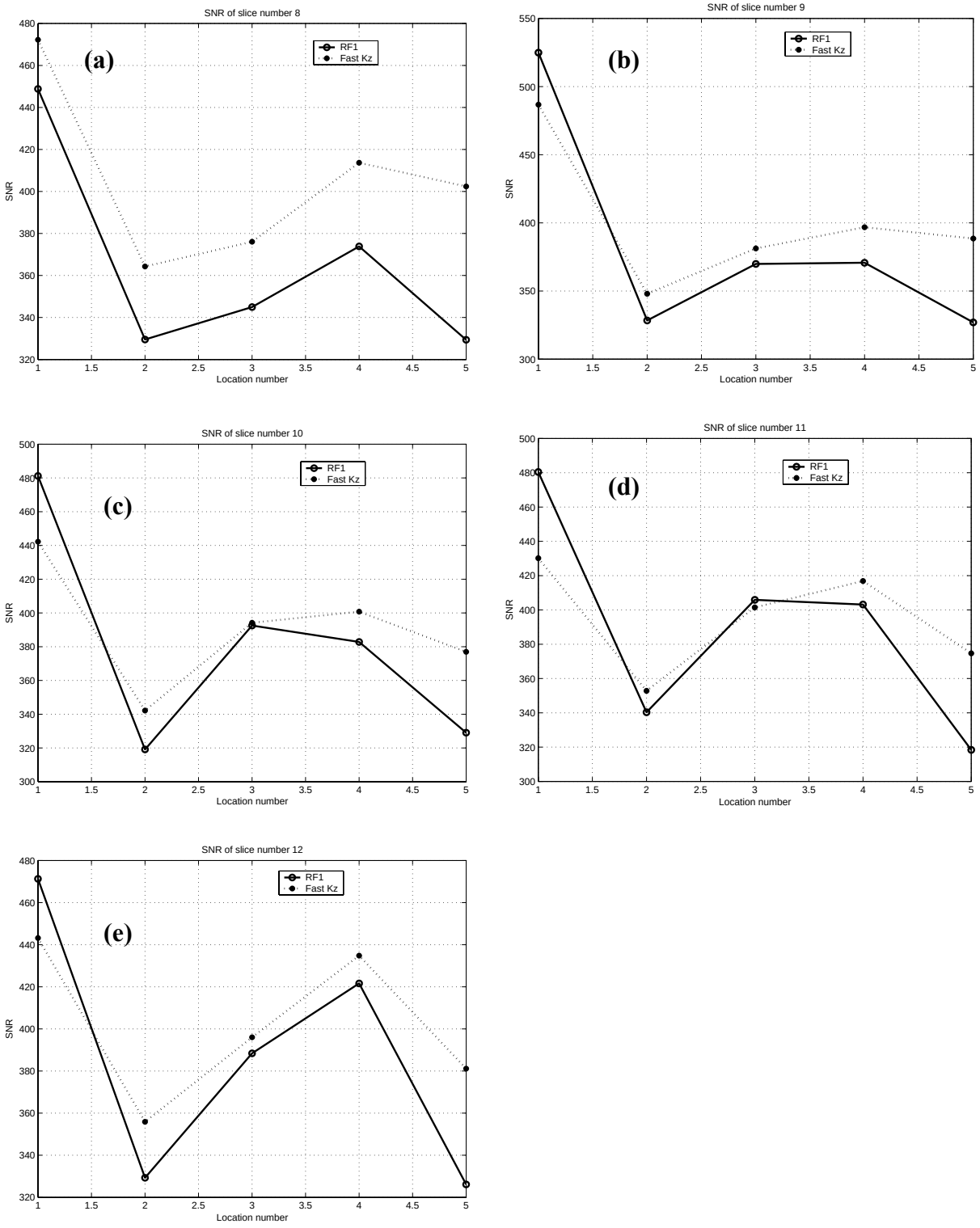

Figure 6.9 SNR of five different locations on human brain images excited by the standard sinc pulses (solid lines) and excited by the compensated fast k_z pulses (dashed lines). All five plots are of locations near the center.

Figure 6.10 plots the different intensities of the center and four peripheral areas in percentages. Difference number 1 is the difference between the center and point number 2. Difference number 2 is the difference between the center and point number 3. This pattern continues for each difference number and point number until the last peripheral point, number 5. The plots were calculated from the five slices of the images with the standard sinc pulses and compensated fast k_z pulses displayed in Figures 6.8(a) and (b), respectively. Figures 6.10 (a) through (e) represent the calculations from slices numbered8 through 12. The solid lines were calculated from the images excited with the standard sinc pulses. The dashed lines were calculated from the images excited by the compensated fast k_z at a fraction of 1.0. Figures 6.10(a) through (e) have lower differences in image intensity between the area at the center and all four peripheral areas of all sles than do the images excited by the compensated fast k_z pulse. This implies that the compensated fast k_z pulse provides more uniform image profiles than the standard sinc pulse.

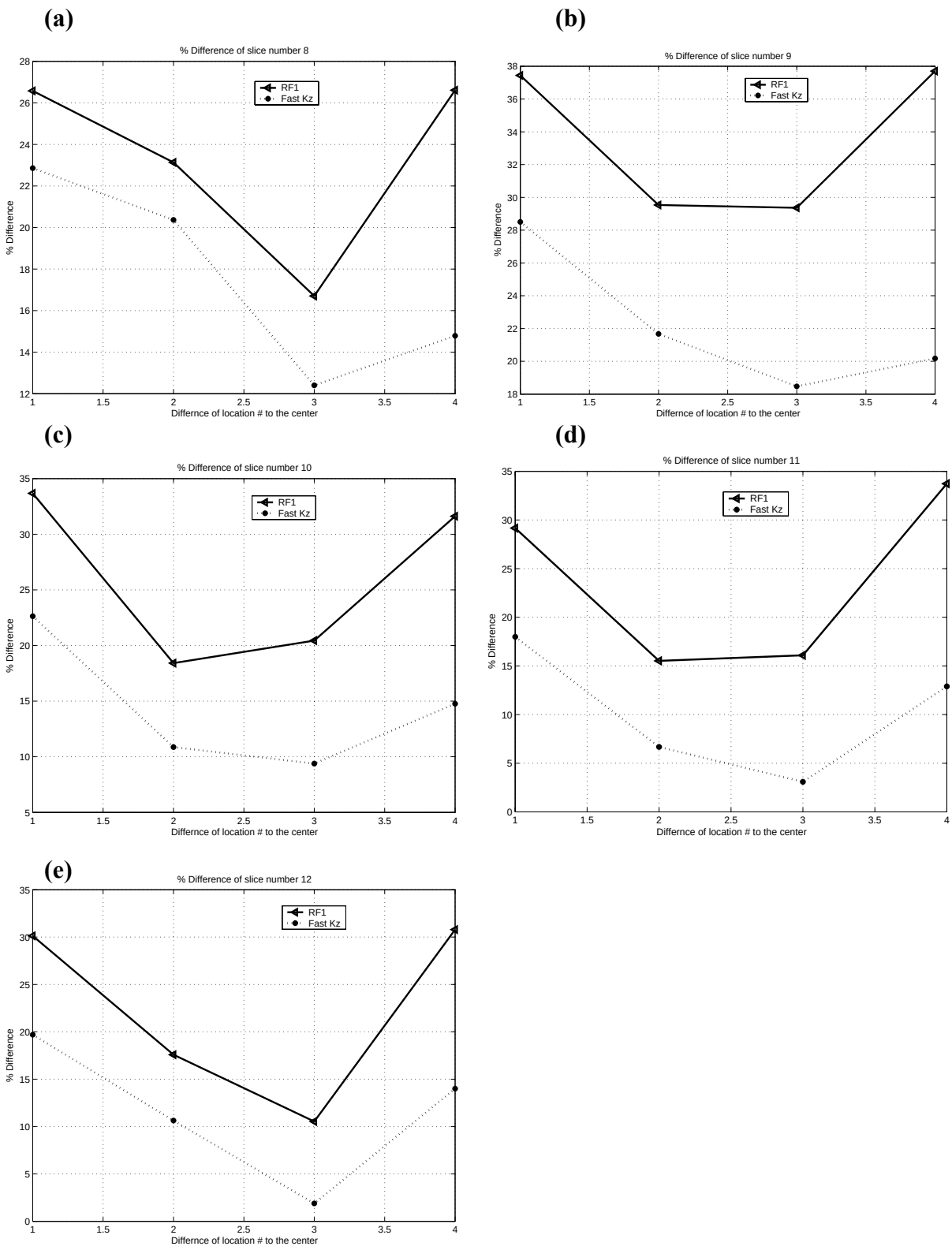

Figure 6.10 Differences in percentage of five different locations on human brain images excited by the standard sinc pulses (solid lines) and excited by the compensated fast k_z pulses (dashed lines). Plots of (a) through (e) are for five different slice locations of Figure 6.6 near the center

6.5 DISCUSSION

According to this study, the SNR plots (in Appendix F) illustrate an inverse relationship to the fractions of compensated fast k_z pulses. The higher the fraction applied to the compensated fast k_z pulse, the lower the SNR that will be obtained from the image. The uniformity of the profiles is determined by the percentage differences of image intensities between average intensity at the center and average intensity at the edges. The uniformity is directly proportional to the fraction of the compensated fast k_z pulses when the fraction is in the range of 0.5-1.5. A fraction of greater than 1.5 shows overcompensation on the images. Application of the compensated fast k_z pulses improves uniformity, but this occurs at the expense of the SNRs. The compensated fast k_z pulse with a fraction of 1.5 was found to be most appropriate for the compensation of slices near the center on phantom experiments in this study. For human brains, however, inhomogeneity is less than it is for the phantom; B_1 compensation is approximately 30 percent, and the pulse with a fraction of 1.0 was found to be the most appropriate pulse. In both the phantom and human experiments, the optimal compensated fast k_z pulses were found to potentially compensate for the loss of the signal at the edges in the region of the center of the volume. However, the slices of those locations away the center have less inhomogeneity; therefore, the use of a constant fraction for the compensated fast k_z pulses throughout the volume of excitation may not be appropriate since it may cause unnecessarily higher energy deposits or an excessive amount of compensation in some slices. This problem may be resolved by incorporating varying flip angles and/or varying pulse fractions for particular slice locations into the pulse sequence on the scanner. This modification may utilize the power deposition of the pulses at each slice location in a more efficient way. SAR was not an issue for this pulse because the design was based on low flip angles and limited the B_1 to, at most, a 90 degree sinc pulse at 3.2 ms pulse width. This pulse

is considered to be safe in general use. The pulse could possibly be optimized to obtain a shorter pulse width and sharper pulse profile with the compromise of peak B_1 and SAR. The limitation of this pulse design is the slice thickness. The larger slice thickness causes the higher peak B_1, thus limiting the flip angle to a very small angle. Another possible limitation is resonance shifts. The pulse is probably more sensitive to resonance shifts due to the dipping of the central lobe gradient that is the major contribution to the pulse [78, 79] .

6.6 CONCLUSIONS

This work presents a new 3D TRF pulse design using fast switching gradients along the z direction and blipping along the x-y direction. It requires only five traverses of k-space. The VERSE technique was adopted to reduce the peak B_1 of the central portion of the pulses, thus allowing more flexible magnitudes of the flip angles. The pulse width is 4.29 ms for a 1-shot pulse, which compares favorably to earlier work which used 3D TRF slab-select pulses of 11 ms for 2-shot pulses. Images excited by the compensated fast k_z pulses are better than those excited by the standard sinc pulse in terms of the signal loss. The loss was found to be 60 percent better in experiments with phantoms and 30 percent better in experiments with human brains. The pulse fraction of 1.5 was found to be the most suitable for the phantom experiment in this study and 1.0 was determined the optimal weighting for the compensated pulse in human brains. Gains in SNR were not compromised by the improvement of uniformity in the image profiles.

7.0 CONCLUSIONS

B_1 inhomogeneity is one of the major technical concerns in MRI higher magnetic field strengths are used. This thesis presents two novel RF pulse designs and examines their limitations for B_1 inhomogeneity reduction in 3T MRI. The feasibility of using these methods for ultra-high field strength imaging was also discussed.

7.1 KEY CONTRIBUTIONS

This thesis makes three major contributions. The first is the development of the 3D TRF slab-select pulses for B_1 inhomogeneity reduction. These RF pulses compensate for signal loss and result in an approximate 30% improvement in the uniformity on the brain images. The images from the 3D TRF slab-select pulses demonstrated significantly more uniform profiles than the standard 3D RF pulses. The design of the compensated 3D TRF slab-select pulse was able to perform on an object that was 10 cm thick for a single-shot pulse of approximately 22 ms, which excited a slab with 2.0x2.0x1.25 cm^3 resolution and a 24x24x20 cm^3 field of view (FOV). In the experiment, the pulses were decomposed into two 11 ms excitations. The acquisition could obtain whole brain coverage with a 2 mm isotropic resolution in 51.2 seconds with two shot pulses, four interleaves spirals, 128 *z* phase encodes, and 50 ms TR. Increasing the resolution to

1 mm would produce an acquisition time slightly less than seven minutes with two shot pulses, 16 interleaves spirals, 256 *z* phase encodes, and 50 ms TR. This amount of time is approximately half that of the general 2D pulse method.

The second major contribution of this work is the exploration of the feasibility of using the compensated 3D TRF slab-select pulses for B_1 inhomogeneity reduction in ultra-high field MRI. The study shows some degree of improvement in image uniformity. The inhomogeneity may be caused by the depositing of insufficient energy into the pulse which, in turn, may be caused by the use of low flip angles or transmitted coils. If this latter attribute is the cause, this pulse may possibly be used for B_1 inhomogeneity reduction at ultra-high field strength. The study serves as a stepping stone for the actual experiment using of these pulses at ultra-high field strength.

The third major contribution is the development of the 3D TRF slice-select pulse design using fast switching of z gradients for B_1 inhomogeneity reduction. This design employs a new k-space design requiring only five traversal lines along the z direction and blips along the x-y direction. The inhomogeneity compensation profiles were built from appropriate analytical functions and incorporated into the pulses. These pulses provide a practical pulse-width of 3-5 ms for 5 mm slice thickness with a single-shot pulse. Inhomogeneity is reduced by 10-60 %, depending on the slice location and spatial location of the images. With the advantage of short pulse length, the 3D fast k_z slice-select pulse is able to acquire high resolution images in a reasonable amount of time.

7.2 FUTURE DIRECTIONS

Although the two new 3D TRF pulse designs demonstrate significant improvement with regard to the uniformity of the images, they still have room for development. Three areas of potential development will be discussed. First, due to the polarization effect, [76] the transmission field and reception field need to be calculated separately. In order to improve accuracy, compensation for B_1 inhomogeneity of 3D TRF slab-select pulses may need to be done only for the transmission field. Compensation for the reception field may need to be performed as part of the post processing scheme.

Second, with the design of the fast k_z pulses, sparse k_z sampling by trajectories is no longer a concern; therefore, Gaussian functions were employed as a slice profile without the problem of aliasing slices. Though the Gaussian function is a smooth function which causes no ripple at the edges, it does not provide a sharp profile. Exploiting the advantage of the pulse design in sampling rate allowance, the sharper slice profile such as the Shinnar–Le Roux (SLR) algorithm[4] [80] may be applied instead. The designed pulse ultimately should be optimized for the constraints of sampling rate, slice profiles and SAR.

Finally, the 3D TRF fast k_z pulses designed for this experiment can be used only for inhomogeneity at 3T in which the inhomogeneity profile can be assumed to be quadratic. In order to extend this concept to the building of a compensated B_1 inhomogeneity pulse at a higher field, the k-space needs to be redesigned to correspond to the spatial compensated profile for B_1

[4] The Shinnar–Le Roux algorithm is based on a numerical solution of the Bloch equations. It was invented by Pauly et al in 1991

inhomogeneity. This may be accomplished by optimizing the location and numbers of the blipping in the k_x-k_y direction.

APPENDIX A

DERIVATION OF THE BLOCH EQUATION IN THE ROTATING FRAME

If pulse duration is short compared to T1 and T2, the last two terms of the Bloch equation can be dropped, and the Bloch equation becomes:

$$\frac{d\mathbf{M}}{dt} = \gamma \mathbf{M} \times \mathbf{B} \tag{A.1}$$

Since the magnetization observed in the lab or in the rotating frame is the same, it can be expressed as

$$\mathbf{M} = \mathbf{M}_{rot} = M_{x'}\mathbf{i}' + M_{y'}\mathbf{j}' + M_{y'}\mathbf{k}' \tag{A.2}$$

Taking the first order derivative on both sides of the Equation (A.2) yields

$$\frac{d\mathbf{M}_{rot}}{dt} = (\frac{dM_{x'}}{dt}\mathbf{i} + \frac{dM_{y'}}{dt}\mathbf{j} + \frac{dM_{z'}}{dt}\mathbf{k}) + (M_{x'}\frac{d\mathbf{i}'}{dt} + M_{y'}\frac{d\mathbf{j}'}{dt} + M_{z}\frac{d\mathbf{k}'}{dt}) \tag{A.3}$$

Let

$$\frac{\partial \mathbf{M}_{rot}}{dt} = \frac{dM_{x'}}{dt}\mathbf{i} + \frac{dM_{y'}}{dt}\mathbf{j} + \frac{dM_{z'}}{dt}\mathbf{k} \tag{A.4}$$

The unit vectors in the rotating frame which rotates in a clockwise direction relates to the lab frame as follows:

$$\begin{aligned} \mathbf{i}' &= \cos(\omega t)\mathbf{i} - \sin(\omega t)\mathbf{j} \\ \mathbf{j}' &= \sin(\omega t)\mathbf{i} + \cos(\omega t)\mathbf{j} \\ \mathbf{k}' &= \mathbf{k} \end{aligned} \tag{A.5}$$

Note that the time derivative of Equation(A.5) followed by coordinate transform is:

$$\frac{d\mathbf{i}'}{dt} = \boldsymbol{\omega} \times \mathbf{i}', \ \frac{d\mathbf{j}'}{dt} = \boldsymbol{\omega} \times \mathbf{j}', \quad \frac{d\mathbf{k}'}{dt} = \boldsymbol{\omega} \times \mathbf{k}' \tag{A.6}$$

Substituting Equations(A.4) and (A.6) into Equation yields

$$\frac{d\mathbf{M}_{rot}}{dt} = \frac{\partial \mathbf{M}_{rot}}{dt} + \boldsymbol{\omega} \times \mathbf{M}_{rot} \tag{A.7}$$

Thus, the Bloch equation from Equation(A.1) in the rotating frame can be written as

$$\frac{d\mathbf{M}_{rot}}{dt} = \gamma \mathbf{M}_{rot} \times \mathbf{B}_{rot} \tag{A.8}$$

Substituting Equation (A.8) into Equation (A.7) yields

$$\frac{\partial \mathbf{M}_{rot}}{dt} = \gamma \mathbf{M}_{rot} \times \mathbf{B}_{rot} - \boldsymbol{\omega} \times \mathbf{M}_{rot} = \gamma \mathbf{M}_{rot} \times (\mathbf{B}_{rot} + \frac{\boldsymbol{\omega}}{\gamma}) \tag{A.9}$$

Equation (A.9) can be rewritten as:

$$\frac{\partial \mathbf{M}_{rot}}{dt} = \gamma \mathbf{M}_{rot} \times \mathbf{B}_{eff} \tag{A.10}$$

where

$$\mathbf{B}_{eff} = \mathbf{B}_{rot} + \frac{\boldsymbol{\omega}}{\gamma} \tag{A.11}$$

APPENDIX B

DERIVATION OF SOLUTION FROM THE BLOCH EQUATION WITH SMALL TIP ANGEL APPROXIMATION

From Equation(2.40),

$$\frac{dM_r}{dt} = -i\omega(z)M_r + i\omega_1(t)M_0 \tag{B.1}$$

The integration factor is $e^{\int i\omega(z)dt} = e^{i\omega(z)t}$

Multiplying Equation(B.1) by the integration factor yields

$$e^{i\omega(z)t} \cdot \frac{dM_r}{dt} + e^{i\omega(z)t} \cdot i\omega(z)M_r = e^{i\omega(z)t} \cdot i\omega_1(t)M_0 \tag{B.2}$$

Equation (B.2)can be rewritten as

$$\left(e^{i\omega(z)t} \cdot M_r(t)\right)' = e^{i\omega(z)t} \cdot i\omega_1(t)M_0 \tag{B.3}$$

Integration can occur on both sides of Equation(B.3), given

$$e^{i\omega(z)t} \cdot M_r(t) = \int_0^t i\omega_1(t)M_0 e^{i\omega(z)\tau} d\tau + C \tag{B.4}$$

Initial condition: Mr(0)=0 implies that C=0, and (B.4) becomes

$$M_r(t) = iM_0 e^{-i\omega(z)t} \int_0^t \omega_1(\tau) e^{i\omega(z)\tau} d\tau \tag{B.5}$$

APPENDIX C

CALCULATION OF TRANSMISSION FIELD AND RECEPTION FIELD

The techniques for using two flip-angles to solve for a transmission field, $\alpha(\mathbf{r})$, and reception field, $C(\mathbf{r})$, were proposed by Mihara, *et al.* [58] and Wang, *et al.* [77]. The Fourier Transform of signal equation (GE) from Equation (2.46) gives the MR imaging equation, $I(\mathbf{r})$, as:

$$I(\mathbf{r}) = i\omega_0 \gamma C(\mathbf{r}) M(\mathbf{r}) \sin(\alpha(\mathbf{r})) \tag{C.1}$$

If two flip angles, one of them with a value double the other, were employed to acquire two images, $I_1(\mathbf{r})$ and $I_2(\mathbf{r})$, $\alpha(\mathbf{r})$ could be solved in the following manner:

$$I_1(\mathbf{r}) = i\omega_0 \gamma C(\mathbf{r}) M(\mathbf{r}) \sin(\alpha_1(\mathbf{r})) \tag{C.2}$$

$$I_2(\mathbf{r}) = i\omega_0 \gamma C(\mathbf{r}) M(\mathbf{r}) \sin(\alpha_2(\mathbf{r})) \tag{C.3}$$

$$\frac{I_1(\mathbf{r})}{I_2(\mathbf{r})} = \frac{\sin(\alpha_1(\mathbf{r}))}{\sin(2\alpha_1(\mathbf{r}))} = \frac{\sin(\alpha_1(\mathbf{r}))}{2\sin(\alpha_1(\mathbf{r}))\cos(\alpha_1(\mathbf{r}))} \tag{C.4}$$

Thus, the transmission field:

$$\alpha_1(\mathbf{r}) = \cos^{-1}\left(\frac{I_2(\mathbf{r})}{2I_1(\mathbf{r})}\right) \tag{C.5}$$

To solve for the reception field, Wang et al [77] introduced an elegant approach to eliminate the third unknown, $M(\mathbf{r})$, by optimizing TE and TR to minimize the contrast among tissues. The reception field becomes

$$C(\mathbf{r}) = \frac{I_1(\mathbf{r})}{i\omega_0 \gamma \sin(\alpha_1(\mathbf{r}))} \tag{C.6}$$

APPENDIX D

CALIBRATION OF FLIP ANGLES BETWEEN SINC PULSE AND FAST K_Z PULSE AT DIFFERENT FRACTIONS.

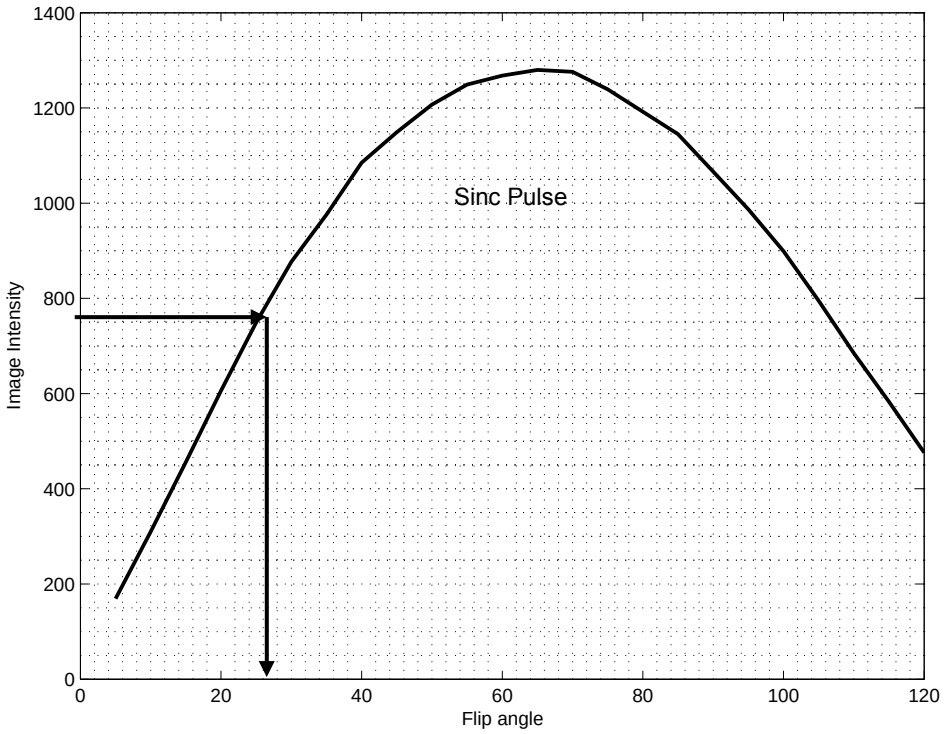

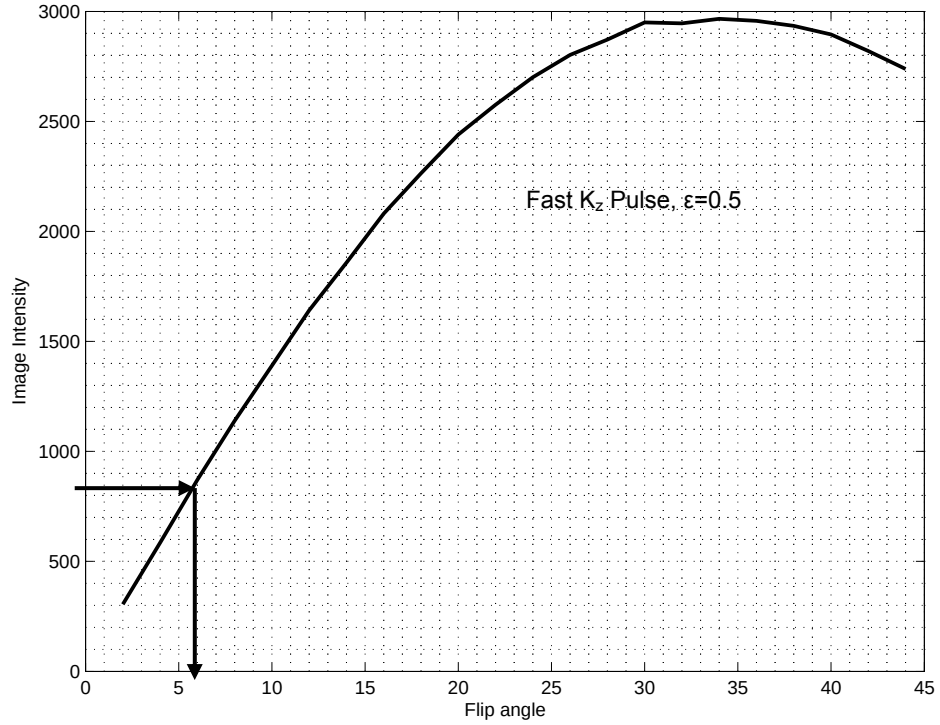
Fast K_z Pulse, ε=0.5
Image Intensity
Flip angle
0
500
1000
1500
2000
2500
3000
0
5
10
15
20
25
30
35
40
45

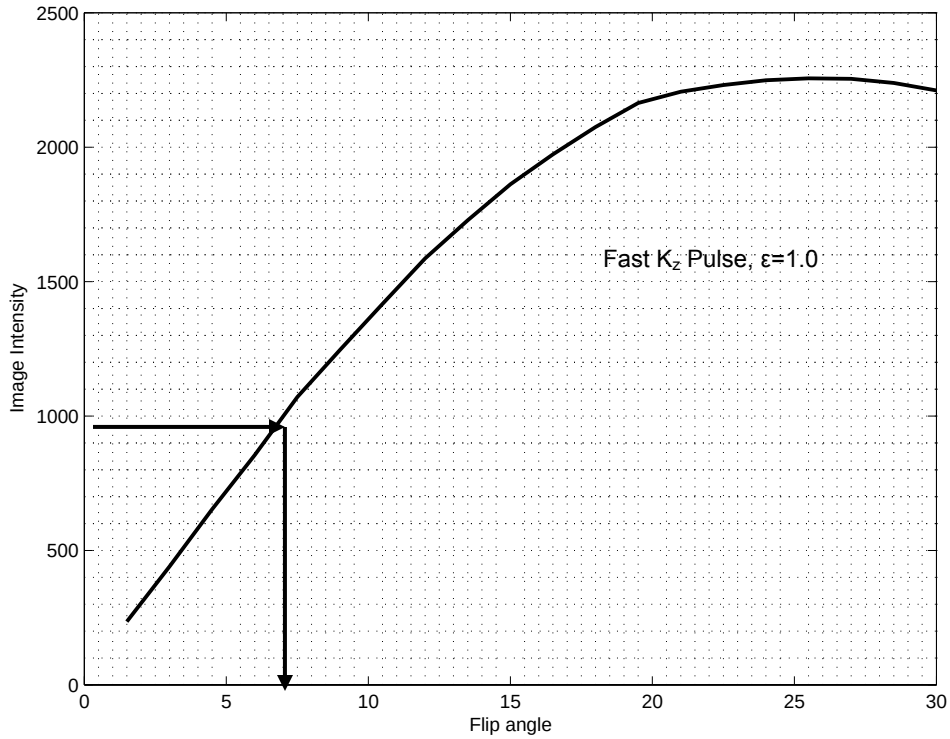
Fast K_z Pulse, ε=1.0
Image Intensity
Flip angle
0
500
1000
1500
2000
2500
0
5
10
15
20
25
30

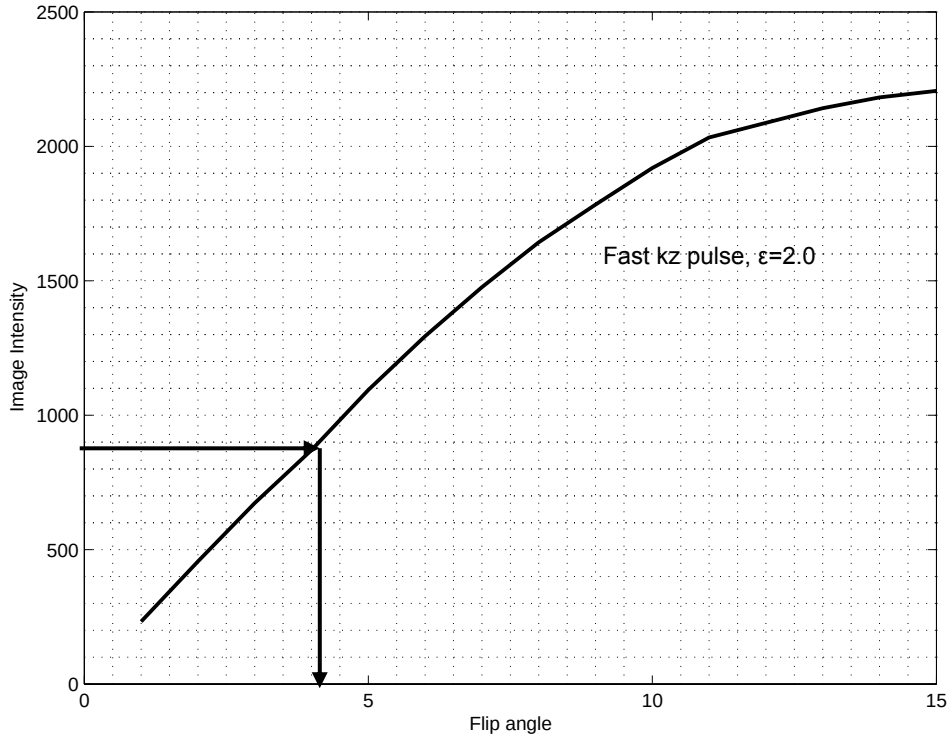
Fast kz pulse, ε=2.0
Image Intensity
Flip angle
0
500
1000
1500
2000
2500
0
5
10
15

APPENDIX E

PHANTOM DATA FROM ONE SINC PULSE AND FOUR 3D COMPENSATED FAST K_Z PULSES

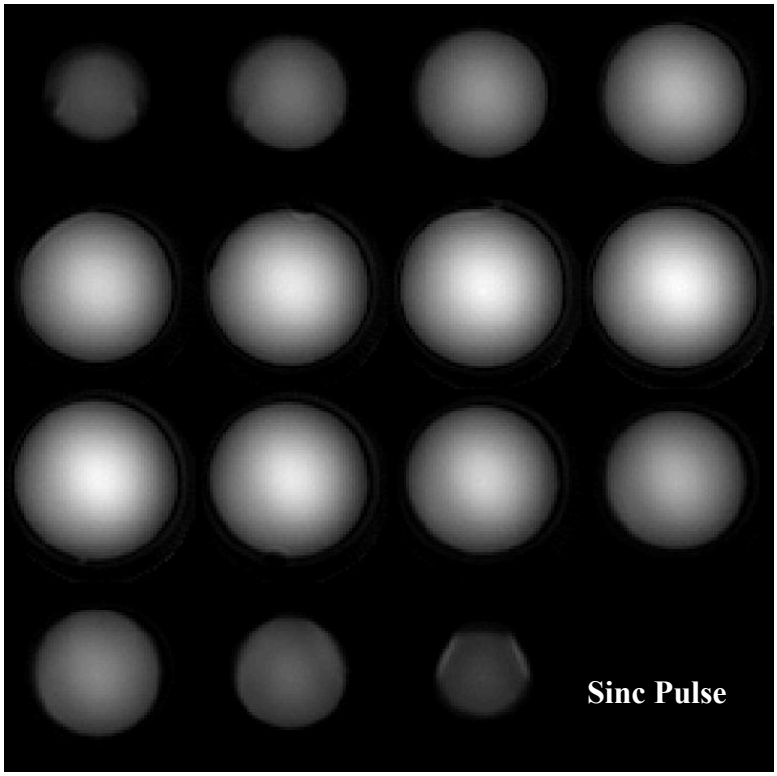

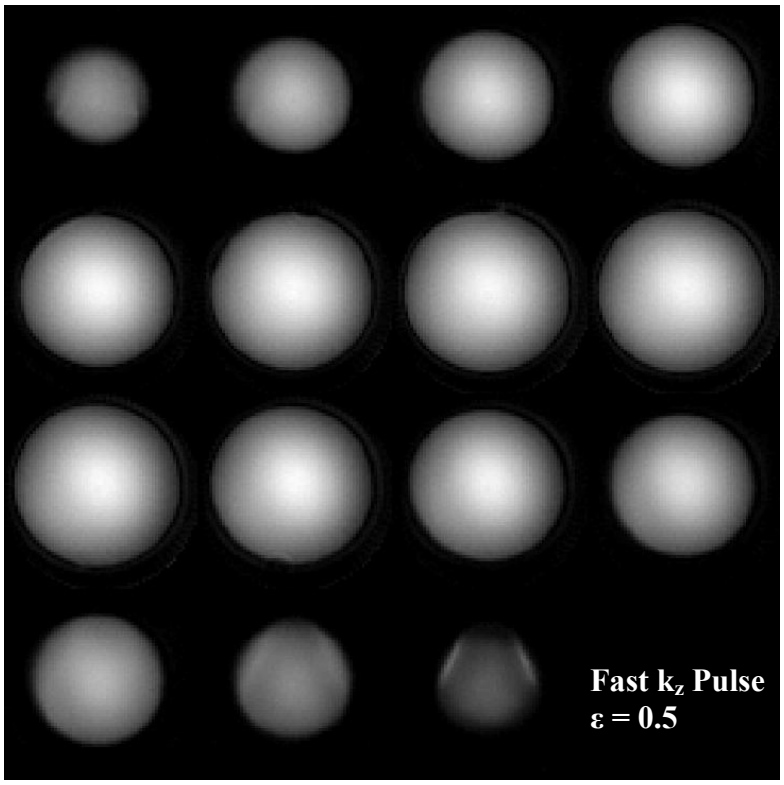
Fast k_z Pulse
$\varepsilon = 0.5$

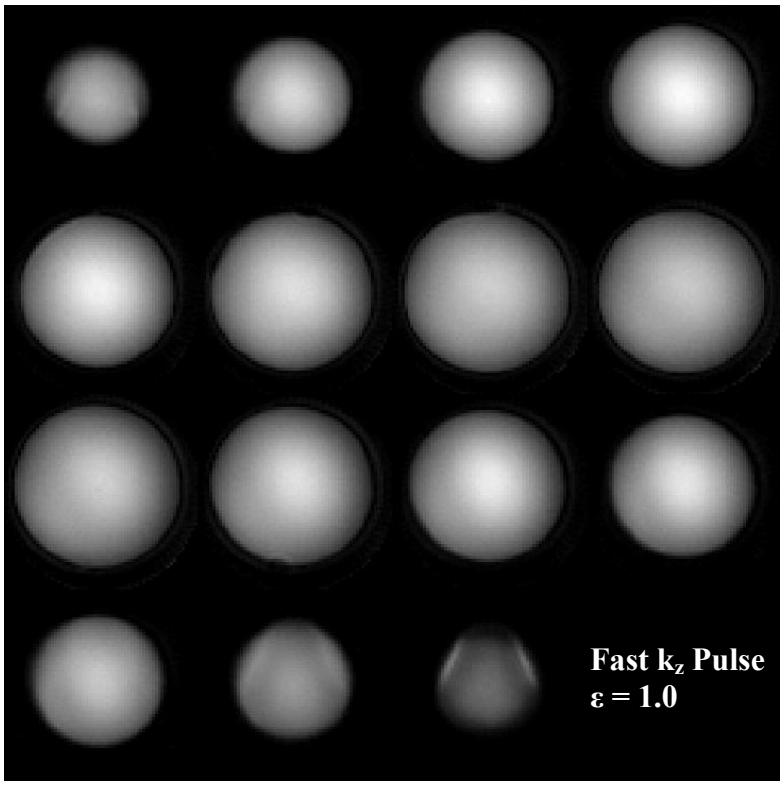
Fast k_z Pulse
$\varepsilon = 1.0$

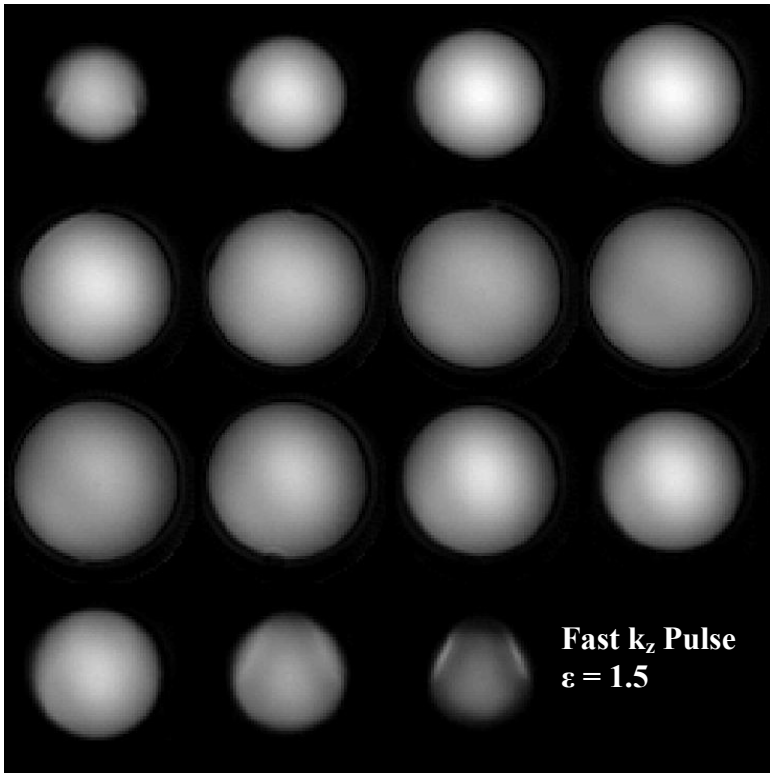
Fast k_z Pulse
$\varepsilon = 1.5$

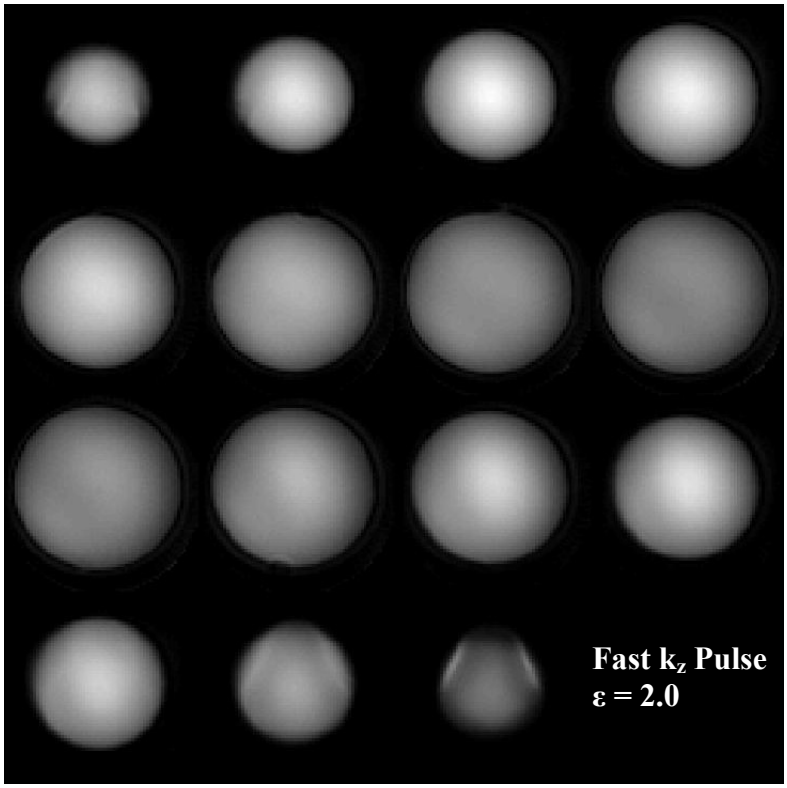
Fast k_z Pulse
$\varepsilon = 2.0$

APPENDIX F

PULSE OPTIMIZATION

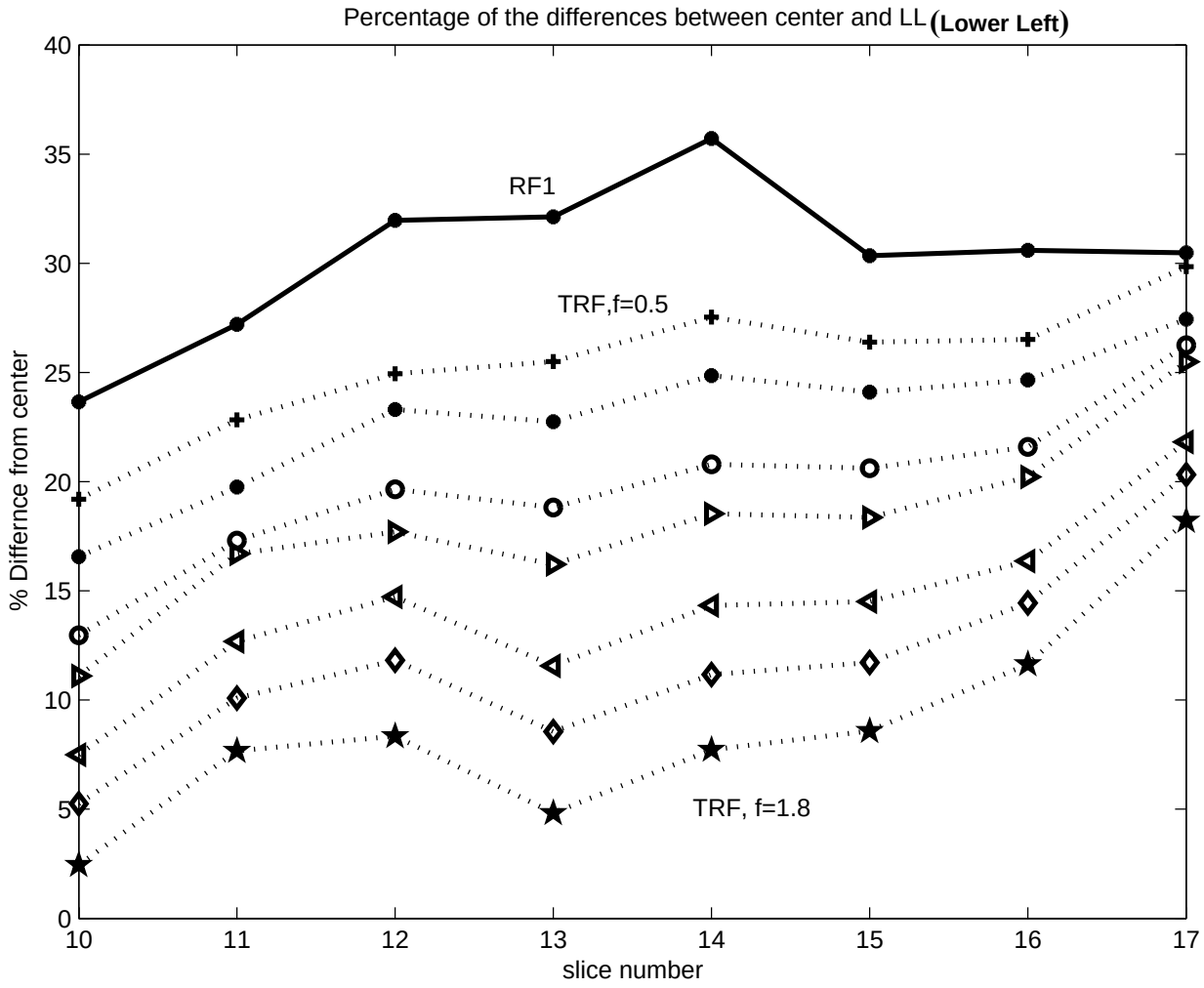

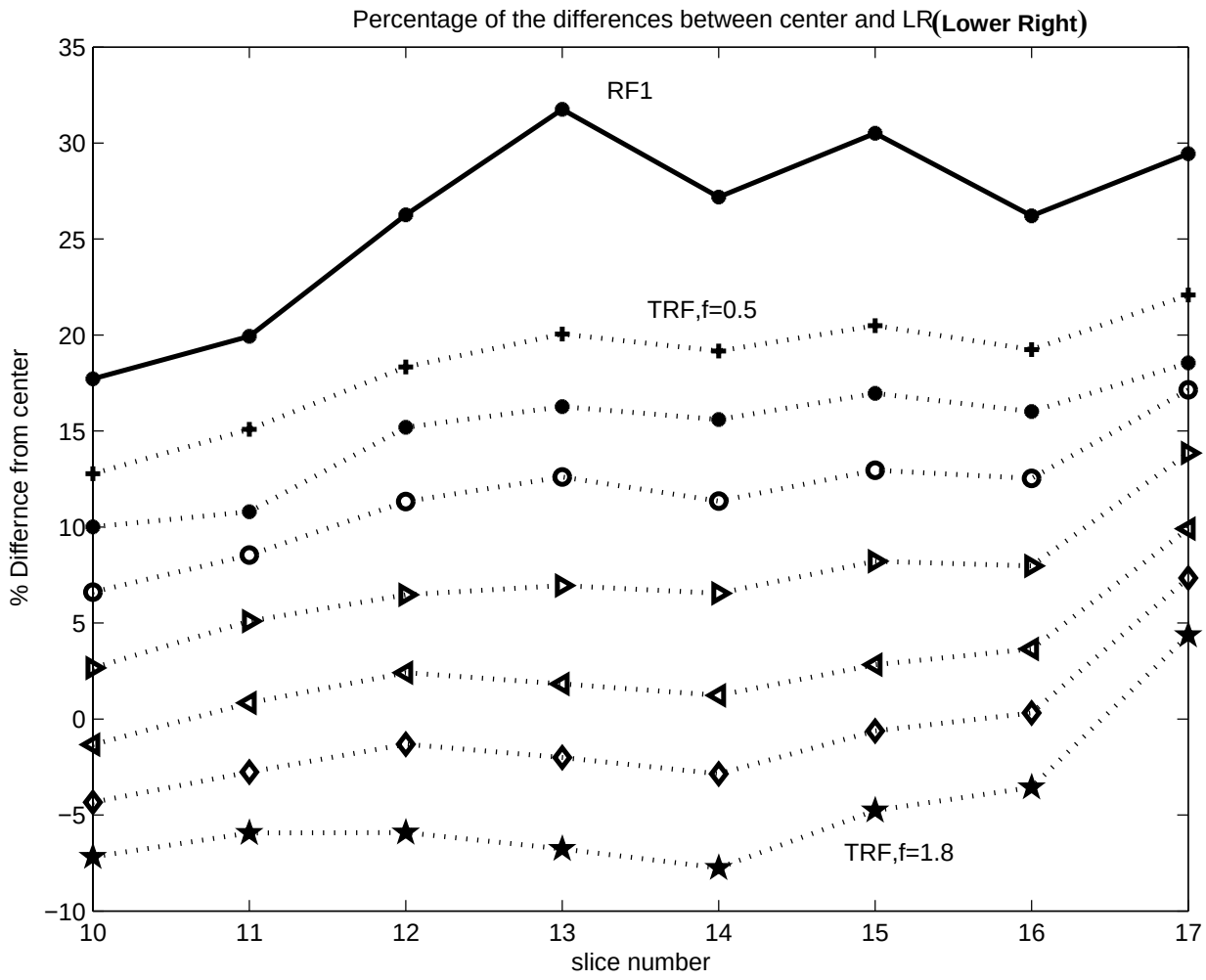
Percentage of the differences between center and LR(Lower Right)
RF1
TRF,f=0.5
TRF,f=1.8
% Differnce from center
slice number
35
30
25
20
15
10
5
0
−5
−10
10
11
12
13
14
15
16
17

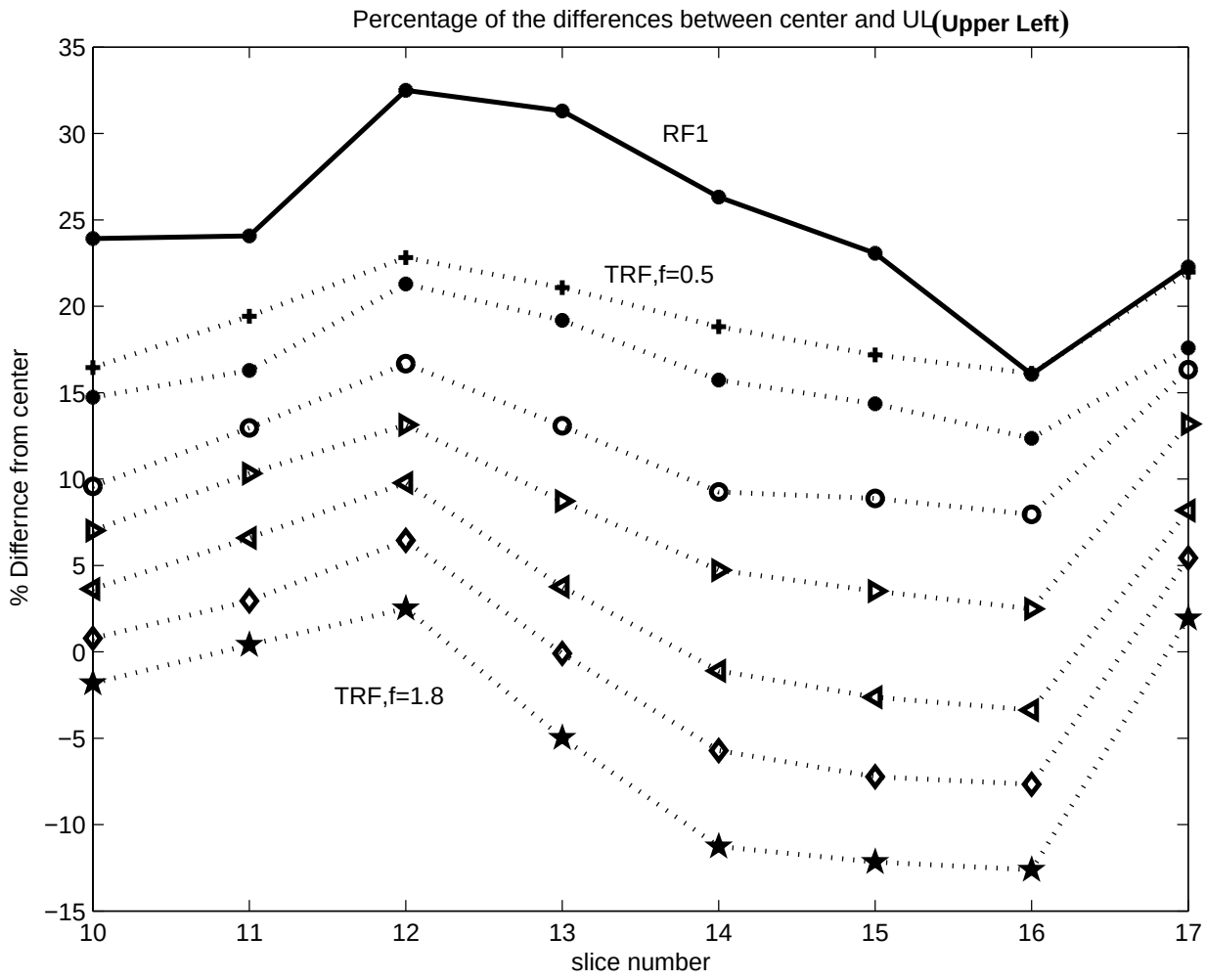
Percentage of the differences between center and UL (Upper Left)
RF1
TRF,f=0.5
TRF,f=1.8
% Differnce from center
slice number
35
30
25
20
15
10
5
0
−5
−10
−15
10
11
12
13
14
15
16
17

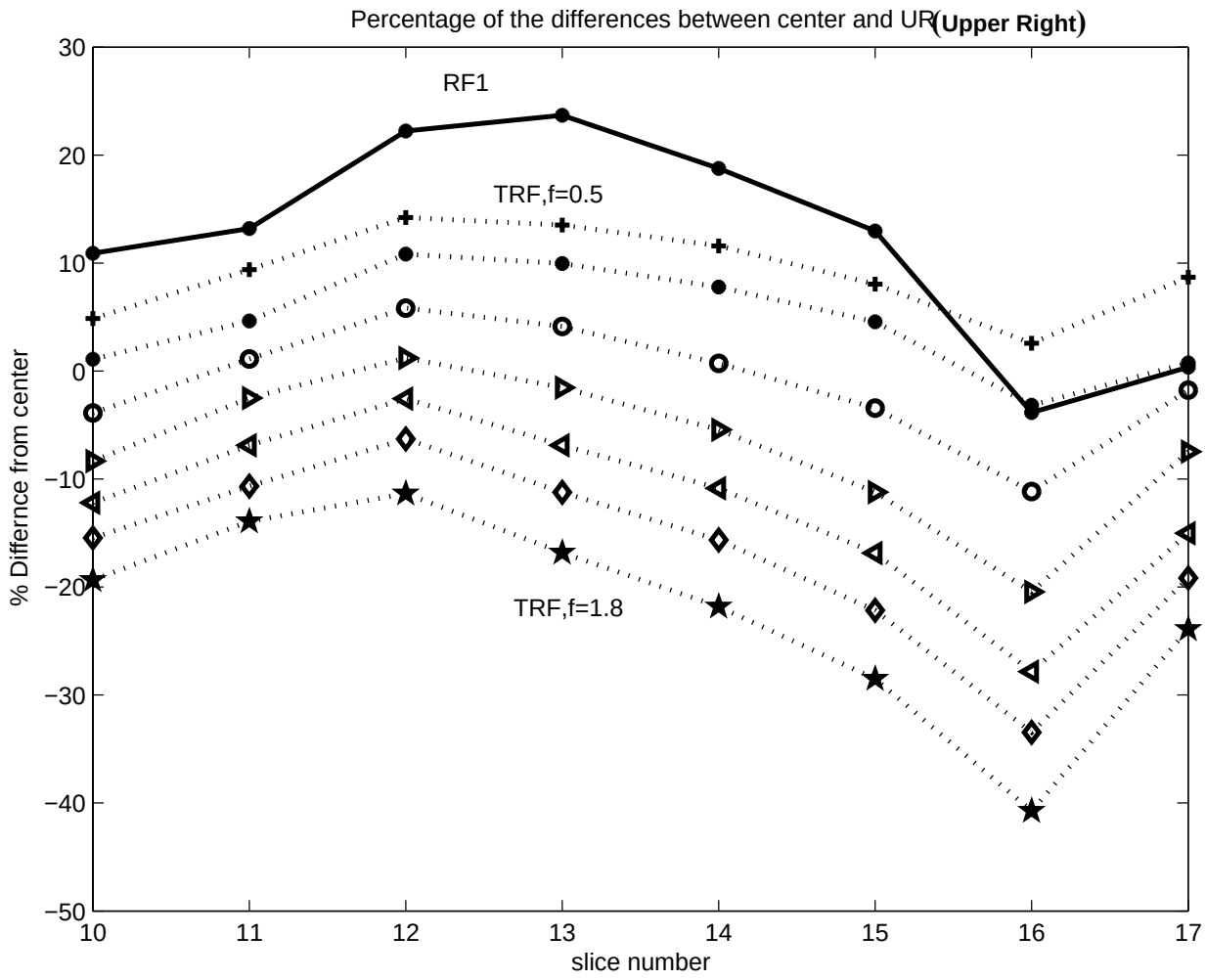
Percentage of the differences between center and UR (Upper Right)
RF1
TRF,f=0.5
TRF,f=1.8
% Differnce from center
slice number
30
20
10
0
−10
−20
−30
−40
−50
10
11
12
13
14
15
16
17

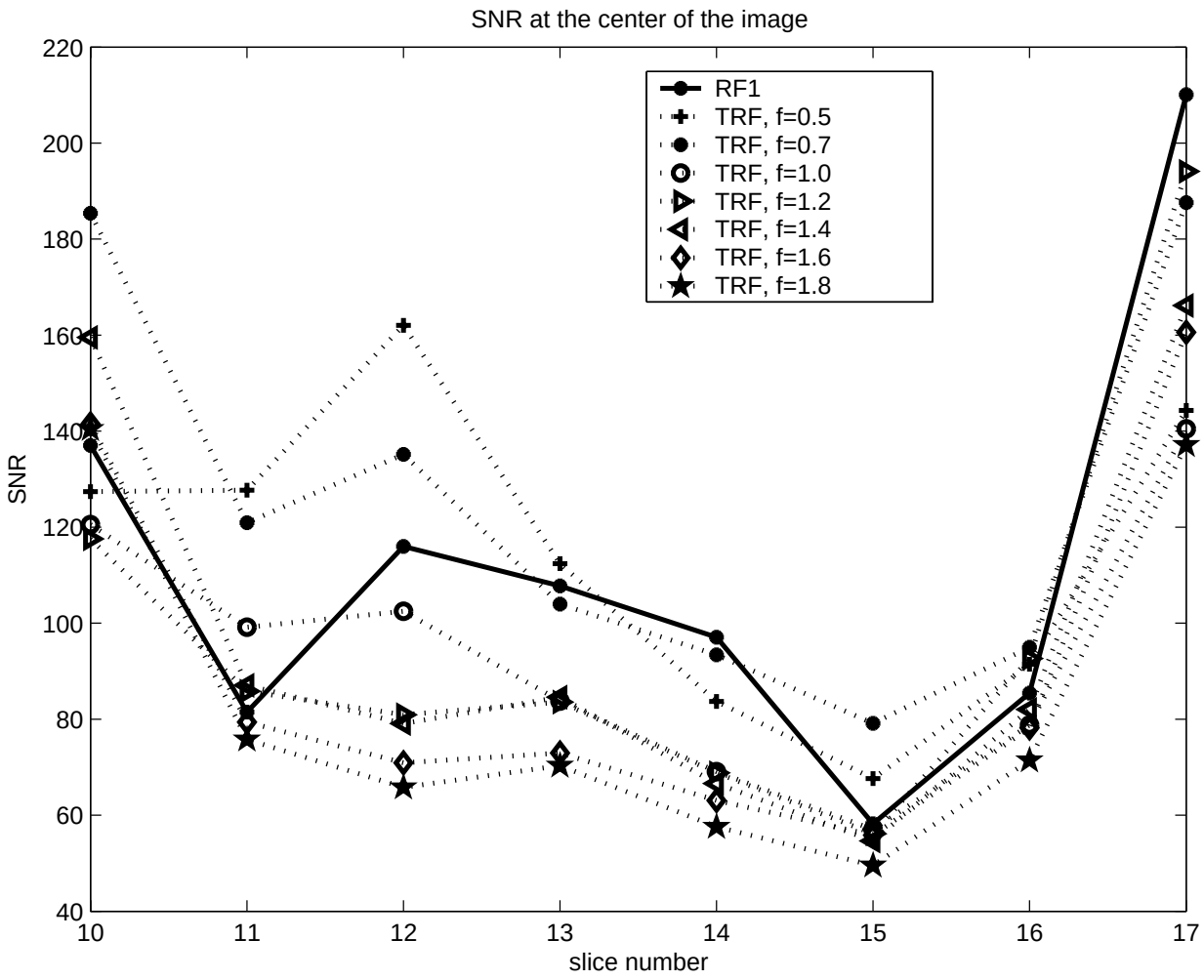
SNR at the center of the image
RF1
TRF, f=0.5
TRF, f=0.7
TRF, f=1.0
TRF, f=1.2
TRF, f=1.4
TRF, f=1.6
TRF, f=1.8
SNR
slice number
220
200
180
160
140
120
100
80
60
40
10
11
12
13
14
15
16
17

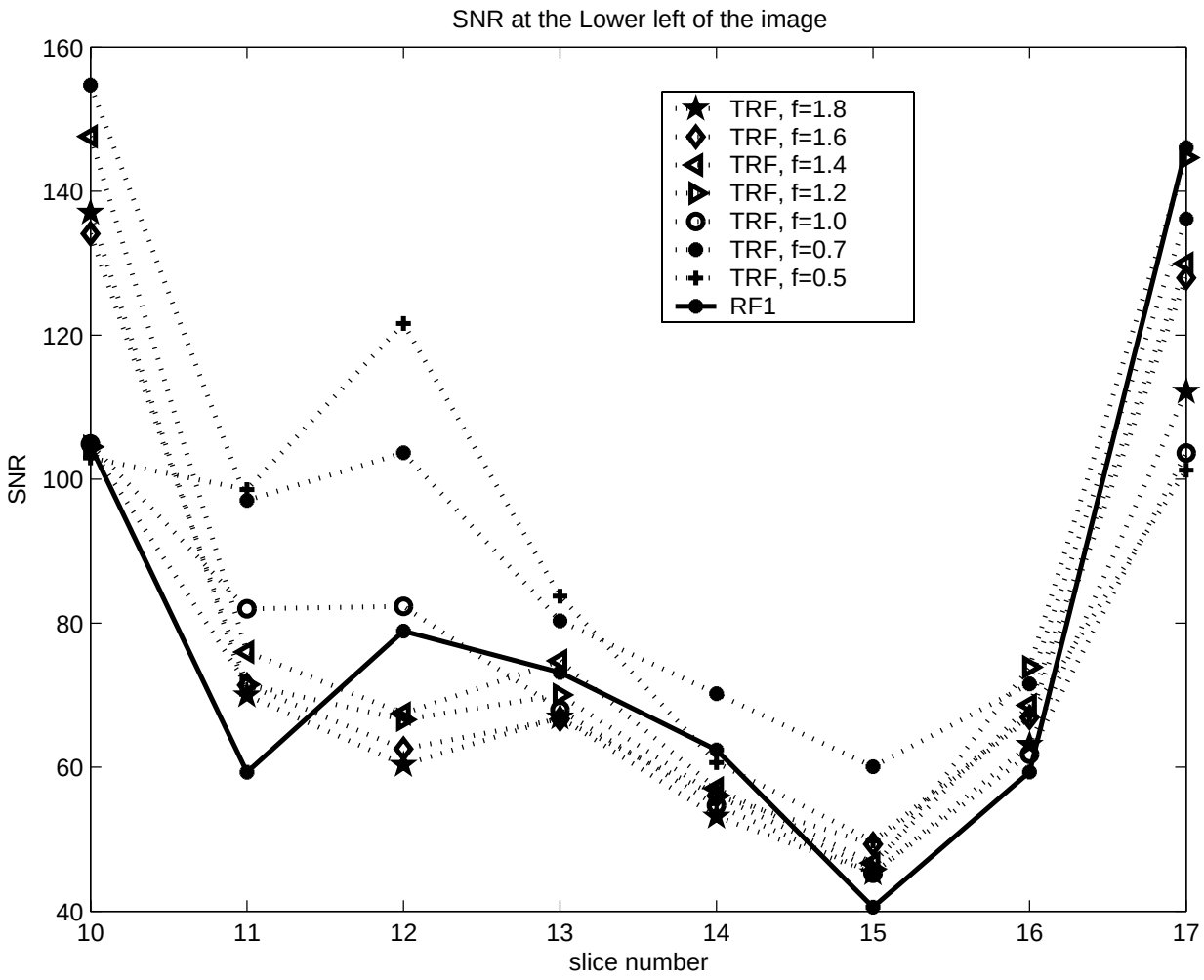
SNR at the Lower left of the image
TRF, f=1.8
TRF, f=1.6
TRF, f=1.4
TRF, f=1.2
TRF, f=1.0
TRF, f=0.7
TRF, f=0.5
RF1
SNR
slice number
160
140
120
100
80
60
40
10
11
12
13
14
15
16
17

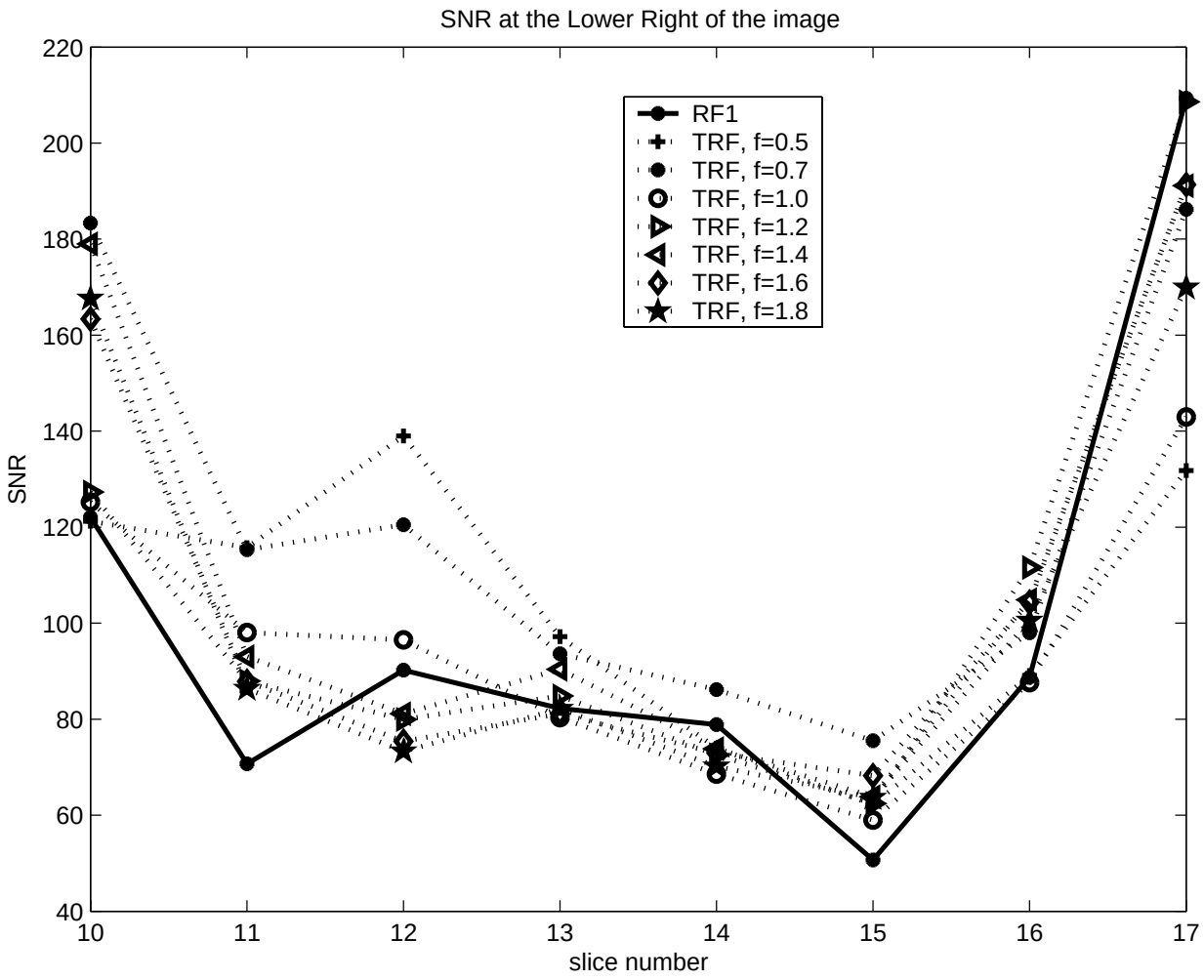
SNR at the Lower Right of the image
SNR
slice number
RF1
TRF, f=0.5
TRF, f=0.7
TRF, f=1.0
TRF, f=1.2
TRF, f=1.4
TRF, f=1.6
TRF, f=1.8
220
200
180
160
140
120
100
80
60
40
10
11
12
13
14
15
16
17

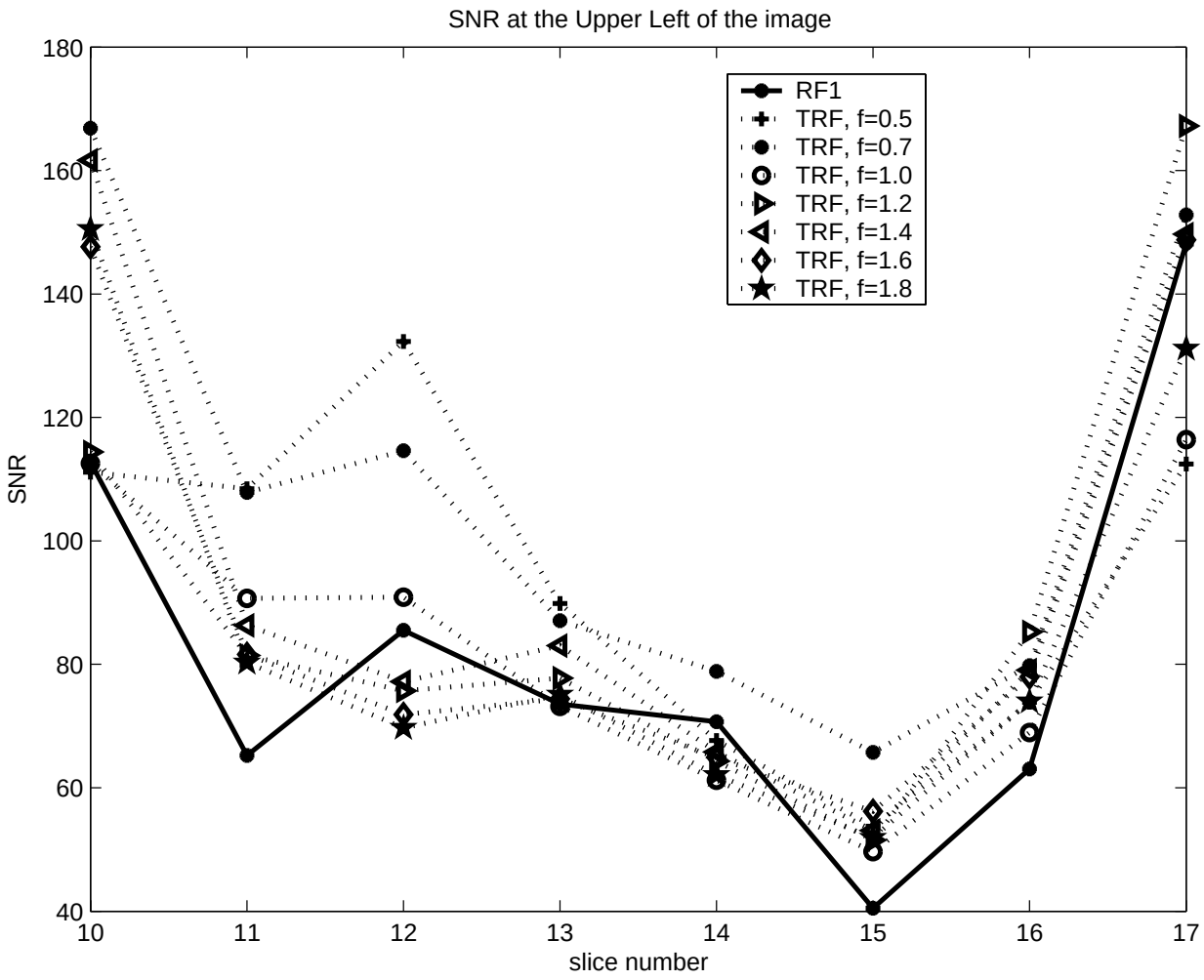
SNR at the Upper Left of the image
RF1
TRF, f=0.5
TRF, f=0.7
TRF, f=1.0
TRF, f=1.2
TRF, f=1.4
TRF, f=1.6
TRF, f=1.8
SNR
slice number
180
160
140
120
100
80
60
40
10
11
12
13
14
15
16
17

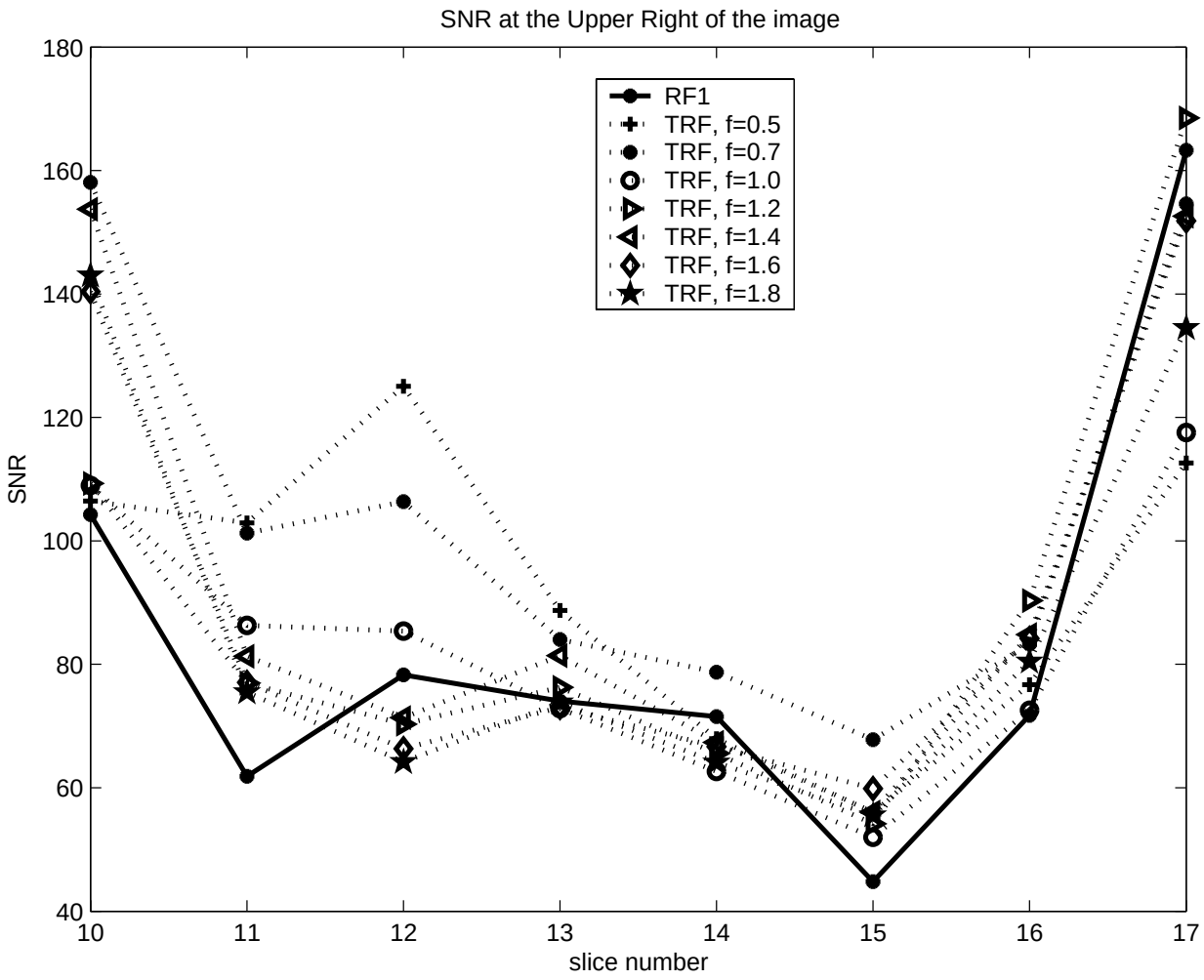
SNR at the Upper Right of the image
RF1
TRF, f=0.5
TRF, f=0.7
TRF, f=1.0
TRF, f=1.2
TRF, f=1.4
TRF, f=1.6
TRF, f=1.8
SNR
slice number
180
160
140
120
100
80
60
40
10
11
12
13
14
15
16
17

BIBLIOGRAPHY

1. Hoult, D. and R. Richards, *The signal to noise ratio of the nuclear magnetic resonance experiment.* J Magn Reson, 1976. **24**: p. 71-85.

2. Edelstein, W.A., et al., *The intrinsic signal-to-noise ratio in NMR imaging.* Magn Reson Med, 1986. **3**(4): p. 604-18.

3. Hu, X. and D.G. Norris, *Advances in high-field magnetic resonance imaging.* Annu Rev Biomed Eng, 2004. **6**: p. 157-84.

4. Ogawa, S., et al., *Oxygenation-sensitive contrast in magnetic resonance image of rodent brain at high magnetic fields.* Magn Reson Med, 1990. **14**: p. 68-78.

5. Frayne, R., et al., *Magnetic resonance imaging at 3.0 Tesla: challenges and advantages in clinical neurological imaging.* Invest Radiol, 2003. **38**(7): p. 385-402.

6. Kim, D.S. and M. Garwood, *High-field magnetic resonance techniques for brain research.* Curr Opin Neurobiol, 2003. **13**(5): p. 612-9.

7. Lin, W., et al., *Practical consideration for 3T imaging.* Magn Reson Imaging Clin N Am, 2003. **11**(4): p. 615-39, vi.

8. Scarabino, T., et al., *3.0 T magnetic resonance in neuroradiology.* Eur J Radiol, 2003. **48**(2): p. 154-64.

9. Barth, M., et al., *Functional MRI of the human motor cortex using single-shot, multiple gradient-echo spiral imaging.* Magn Reson Imaging, 1999. **17**(9): p. 1239-43.

10. Chen, Y.C., et al., *Improved mapping of pharmacologically induced neuronal activation using the IRON technique with superparamagnetic blood pool agents.* J Magn Reson Imaging, 2001. **14**(5): p. 517-24.

11. Yacoub, E., et al., *Spin-echo fMRI in humans using high spatial resolutions and high magnetic fields.* Magn Reson Med, 2003. **49**(4): p. 655-64.

12. Bernstein, M.A., et al., *High-resolution intracranial and cervical MRA at 3.0T: technical considerations and initial experience.* Magn Reson Med, 2001. **46**(5): p. 955-62.

13. Christoforidis, G.A., et al., *High resolution MRI of the deep brain vascular anatomy at 8 Tesla: susceptibility-based enhancement of the venous structures.* J Comput Assist Tomogr, 1999. **23**(6): p. 857-66.

14. Christoforidis, G.A., et al., *Visualization of microvascularity in glioblastoma multiforme with 8-T high-spatial-resolution MR imaging.* AJNR Am J Neuroradiol, 2002. **23**(9): p. 1553-6.

15. Nishimura, D., *Principles of Magnetic Resonance Imaging*. 1995.

16. Liang, Z. and P. Lauterbur, *Principles of Magnetic Resonance Imaging: A Signal Processing Perspective*, ed. M. Akay. 2000, New York: IEEE Press.

17. Garroway, A., P. Grannell, and P. Mansfield, *Image formation in NMR by a selective irradiative.* J. Phys.C:Solid State Physics, 1974. **7**: p. 457-462.

18. Hoult, D.I., *The solution to the Bloch equations in the presence of a varying B1 field.* J. Magn. Reson., 1979. **35**: p. 69-86.

19. Hinshaw, W.S. and A.H. Lent, *An Introduction to NMR Imaging: From the Bloch Equation to the Imaging Equation.* Proc. IEEE, 1983. **71**: p. 338-350.

20. Pauly, J.M., D. Nishimura, and A. Macovski, *A k-space analysis of small-tip-angle excitation.* J. Magn. Reson., 1989. **81**: p. 43-56.

21. Hoult, D., *The principle of Reciprocity in Signal Strength Calculations-A Mathematical Guide.* Concepts in Magnetic Resonanc, 2000. **12**: p. 173-187.

22. Mansfield, P., *Principles of NMR imaging, in Physics of NMR spectroscopy in Biology and medicine*, ed. B. Maraviglia. 1988: North Holland Physics Publishing:Amsterdam.

23. Meyer, C., et al., *Fast Spiral Coronary Artery Imaging.* Magn. Reson. Med., 1992. **28**: p. 202-213.

24. Ahn, C.B., J.H. Kim, and Z.H. Cho, *High-speed spiral-scan echo planar NMR imaging-I.* IEEE Transactions on Medical Imaging, 1986. **MI-5**: p. 2-7.

25. Mansfield, P., *Multi-planar image formation using NMR spin echoes.* J. Phys.C:Solid State Physics, 1977. **10**: p. L55-L58.

26. Pauly, J., D. Nishimura, and A. Macovski, *A Linear Class of Large Tip-Angle Selective Excitation Pulses.* Journal of Magnetic Resonance, 1989. **82**: p. 571-587.

27. Bornert, P. and T. Schaffter, *Curved slice imaging.* Magn Reson Med, 1996. **36**(6): p. 932-9.

28. Bornert, P. and B. Aldefeld, *On spatially selective RF excitation and its analogy with spiral MR image acquisition.* Magma, 1998. **7**(3): p. 166-78.

29. Hardy, C.J. and H.E. Cline, *Spatial Localization in Two Dimensions using NMR designer pulses.* Journal of Magnetic Resonance, 1989. **82**(647-654).

30. Bornert, P., *2D-RF-pulse-encoded curved-slice imaging.* Magma, 2003. **16**(2): p. 86-92.

31. Stenger, V.A., F.E. Boada, and D.C. Noll, *Three-dimensional tailored RF pulses for the reduction of susceptibility artifacts in T2*-weighted functional MRI.* Magn Reson Med, 2000. **44**: p. 525-531.

32. Stenger, V.A., F.E. Boada, and D.C. Noll, *Multishot 3D slice-select tailored RF pulses for MRI.* Magn Reson Med, 2002. **48**: p. 157-165.

33. Irarrazabal, P. and D. Nishimura, *Fast Three Dimensional Magnetic Resonance Imaging.* Magn Reson Med, 1995. **33**(5): p. 656-662.

34. Glover, G.H., *Simple Analytical Spiral K-Space Algorithm.* Magnetic Resonance in Medicine, 1999. **42**: p. 412-415.

35. Duyn, J.H. and Y. Yang, *Fast spiral magnetic resonance imaging with trapezoidal gradients.* J Magn Reson, 1997. **128**(2): p. 130-4.

36. Macovski, A., *Noise in MRI.* Magnetic Resonance in Medicine, 1996. **36**: p. 494-497.

37. Vaughan, J.T., et al., *7T vs. 4T: RF power, homogeneity, and signal-to-noise comparison in head images.* Magn Reson Med, 2001. **46**(1): p. 24-30.

38. Vaughan, J.T., et al., *Detunable transverse electromagnetic (TEM) volume coil for high-field NMR.* Magn Reson Med, 2002. **47**(5): p. 990-1000.

39. Szaflarski, J.P., et al., *High-resolution functional MRI at 3T in healthy and epilepsy subjects: hippocampal activation with picture encoding task.* Epilepsy Behav, 2004. **5**(2): p. 244-52.

40. Haacke, E., et al., *Magnetic resonance Imaging: physical principles and sequence design*. 1999, New York: A John Wiley and Sons.

41. Conolly, S., A. Macovski, and J. Pauly, *Magnetic resonnace imaging:Acquisition and processing in Biomedical Engineering Handbook*. 1994: CRC Press,Inc.

42. Yang, Q.X., et al., *Analysis of wave behavior in lossy dielectric samples at high field.* Magn Reson Med, 2002. **47**(5): p. 982-9.

43. Ibrahim, T.S., et al., *Dielectric resonances and B(1) field inhomogeneity in UHFMRI: computational analysis and experimental findings.* Magn Reson Imaging, 2001. **19**(2): p. 219-26.

44. Alecci, M., et al., *Radio frequency magnetic field mapping of a 3 Tesla birdcage coil: experimental and theoretical dependence on sample properties.* Magn Reson Med, 2001. **46**(2): p. 379-85.

45. Griffiths, D.J., *Introduction to Electrodynamics*, ed. Second. 1989, Englewood Cliffs, New Jersy: Prentice Hall.

46. Lin, C., et al., *Reduction of RF power for magnetization transfer with optimized application of RF pulses in k-space.* Magn Reson Med, 2003. **50**(1): p. 114-21.

47. Uematsu, H., et al., *High field body MR imaging: preliminary experiences.* Clin Imaging, 2004. **28**(3): p. 159-62.

48. Abduljalil, A.M., et al., *Macroscopic susceptibility in ultra high field MRI. II: acquisition of spin echo images from the human head.* J Comput Assist Tomogr, 1999. **23**(6): p. 842-4.

49. Yang, Q.X., et al., *Microimaging at 14 tesla using GESEPI for removal of magnetic susceptibility artifacts in T(2)(*)-weighted image contrast.* J Magn Reson, 1999. **141**(1): p. 1-6.

50. Alsop, D.C., T.J. Connick, and G. Mizsei, *A spiral volume coil for improved RF field homogeneity at high static magnetic field strength.* Magn Reson Med, 1998. **40**(1): p. 49-54.

51. Ibrahim, T.S., et al., *Effect of RF coil excitation on field inhomogeneity at ultra high fields: a field optimized TEM resonator.* Magn Reson Imaging, 2001. **19**(10): p. 1339-47.

52. Staewen, R., et al., *3-D FLASH imaging using a single surface coil and a new adiabatic pulse, BIR-4.* Invest Radiol, 1990. **25**: p. 559-567.

53. Deichmann, R., et al., *Optimization of 3-D MP-RAGE sequences for structural brain imaging.* Neuroimage, 2000. **12**(1): p. 112-27.

54. Deichmann, R., C. Good, and R. Turner, *RF inhomogeneity compensation in structural brain imaging.* Magn Reson Med, 2002. **47**: p. 398-402.

55. Clare, S., M. Alecci, and P. Jezzard, *Compensating for B(1) inhomogeneity using active transmit power modulation.* Magn Reson Imaging, 2001. **19**(10): p. 1349-52.

56. Cohen, M.S., R.M. DuBois, and M.M. Zeineh, *Rapid and effective correction of RF inhomogeneity for high field magnetic resonance imaging.* Hum Brain Mapp, 2000. **10**(4): p. 204-11.

57. Simmons, A., et al., *Sources of intensity nonuniformity in spin echo images at 1.5 T.* Magn Reson Med, 1994. **32**(1): p. 121-8.

58. Mihara, H., N. Iriguchi, and S. Ueno, *A method of RF inhomogeneity correction in MR imaging.* Magma, 1998. **7**(2): p. 115-20.

59. Guillemand R and Brady M, *Estimating the bias field of MR images.* IEEE Transations on Medical Imaging, 1997. **16**(3): p. 238-51.

60. DeCarli, C., et al., *Local histogram correction of MRI spatially dependent image pixel intensity nonuniformity.* J Magn Reson Imaging, 1996. **6**(3): p. 519-28.

61. Lee, S.K. and M.W. Vannier, *Post-acquisition correction of MR inhomogeneities.* Magn Reson Med, 1996. **36**(2): p. 275-86.

62. Koivula, A., J. Alakuijala, and O. Tervonen, *Image feature based automatic correction of low-frequency spatial intensity variations in MR images.* Magn Reson Imaging, 1997. **15**(10): p. 1167-75.

63. Wang, L., et al., *Correction for variations in MRI scanner sensitivity in brain studies with histogram matching.* Magn Reson Med, 1998. **39**(2): p. 322-7.

64. Sled, J.G., A.P. Zijdenbos, and A.C. Evans, *A nonparametric method for automatic correction of intensity nonuniformity in MRI data.* IEEE Trans Med Imaging, 1998. **17**(1): p. 87-97.

65. Zhang, X., K. Ugurbil, and W. Chen, *A microstrip transmission line volume coil for human head MR imaging at 4T.* J Magn Reson, 2003. **161**(2): p. 242-51.

66. Staewen, R.S., et al., *3-D FLASH imaging using a single surface coil and a new adiabatic pulse, BIR-4.* Invest Radiol, 1990. **25**(5): p. 559-67.

67. Conolly, S., et al., *A reduced power selective adiabatic spin-echo pulse sequence.* Magn Reson Med, 1991. **18**(1): p. 28-38.

68. de Graaf, R.A., K. Nicolay, and M. Garwood, *Single-shot, B1-insensitive slice selection with a gradient-modulated adiabatic pulse, BISS-8.* Magn Reson Med, 1996. **35**(5): p. 652-7.

69. Shen, J. and D.L. Rothman, *Adiabatic slice-selective excitation for surface coils.* J Magn Reson, 1997. **124**(1): p. 72-9.

70. Mugler, J.P., 3rd and J.R. Brookeman, *Three-dimensional magnetization-prepared rapid gradient-echo imaging (3D MP RAGE).* Magn Reson Med, 1990. **15**(1): p. 152-7.

71. Bampton, A.E., S.J. Riederer, and H.W. Korin, *Centric phase-encoding order in three-dimensional MP-RAGE sequences: application to abdominal imaging.* J Magn Reson Imaging, 1992. **2**(3): p. 327-34.

72. Zhou, L.Q., et al., *A method of radio-frequency inhomogeneity correction for brain tissue segmentation in MRI.* Comput Med Imaging Graph, 2001. **25**(5): p. 379-89.

73. Hardy, C.C.J., H.E. Cline, and P.A. Bottomley, *Correcting for nonuniform k-space sampling in two-dimensional NMR selective excitation.* J Magn Reson, 1990. **87**: p. 639-645.

74. Stollberger, R. and P. Wach, *Imaging of the active B1 Field in vivo.* Magn Reson Med, 1996. **35**: p. 246-251.

75. Collins, C.M., et al., *Different excitation and reception distributions with a single-loop transmit-receive surface coil near a head-sized spherical phantom at 300 MHz.* Magn Reson Med, 2002. **47**: p. 1026-1028.

76. Wang, J., et al., *Polarization of the RF field in a human head at high field: a study with a quadrature surface coil at 7.0 T.* Magn Reson Med, 2002. **48**(2): p. 362-9.

77. Wang, J.H., et al., *Correction of Transmission and Reception Induced Signal Intensity Inhomogeneity in Vivo*. 2003.

78. Conolly, S., D. Nishimura, and A. Macovski, *Variable-Rate Selective Excitaion.* Journal of Magnetc Resonance, 1988. **78**: p. 440-458.

79. Hargreaves, B.A., et al., *Variable-rate selective excitation for rapid MRI sequences.* Magn Reson Med, 2004. **52**(3): p. 590-7.

80. Pauly, J.M., et al., *Parameter Relations for the Shinnar-LeRoux Selective Excitation Pulse Design Algorithm.* IEEE Trans. Med. Imaging, 1991. **10**: p. 53-65.